Fabrication of MoO_2 and VO_2 Thin Films Using Mist Chemical Vapor Deposition

Yuya Matamura

Fabrication of MoO_2 and VO_2 Thin Films Using Mist Chemical Vapor Deposition

Yuya Matamura

2022

Contents

Chapter 1 General Introduction 1
1.1 Background 1
1.2 Thin Films Fabrication via Chemical Vapor Deposition 3
1.3 Mist CVD Method 4
1.4 MoO_2 and VO_2 5
1.4.1 MoO_2 5
1.4.2 VO_2 6
1.5 Mist CVD Application to MoO_2 and VO_2 7
1.6 Aims and Outline of This Thesis 8
References 10
Chapter 2 Mist Chemical Vapor Deposition of MoO_2 Thin Films 17
2.1 Introduction 17
2.2 Experimental 18
2.2.1 Materials 18
2.2.2 Mist CVD of MoO_2 18
2.2.3 Characterization of films 19
2.3 Results and Discussion 21
2.3.1 Appearance of the films 21
2.3.2 Phase of films 24
2.3.3 Composition and chemical states of films 26
2.3.4 Morphology of films 28
2.3.5 Electrical resistivity 31
2.3.6 Discussion 32
2.4 Conclusion 33
References 34
Chapter 3 Mist CVD of Vanadium Dioxide Thin Films with Excellent Thermochromic Properties Using a Water-Based Precursor Solution 36
3.1 Introduction 36
3.2 Experimental 38

3.2.1 Materials 38
3.2.2 Mist CVD of VO_2 38
3.2.3 Characterization of films 38
3.3 Results and Discussion 41
3.3.1 Appearance and phase of the films 41
3.3.2 Composition and chemical states of films 44
3.3.3 Morphology of films 48
3.3.4 Metal–insulator transition behavior 49
3.3.5 Optical properties 52
3.4 Conclusion 55
References 56
Chapter 4 Formation of Uniquely Oriented VO_2 Thin Film by Topotactic Oxidation of V_2O_3 Epitaxial Film on R-plane Al_2O_3 62
4.1 Introduction 62
4.2 Experimental 64
4.2.1 Materials 64
4.2.2 Mist CVD of V_2O_3 64
4.2.3 Thermal oxidation 64
4.2.4 Characterization of the films 64
4.3 Result and Discussion 66
4.3.1 V_2O_3 epitaxial growth by mist CVD 66
4.3.2 Oxidation to VO_2 71
4.3.3 Topotactic relationship 80
4.3.4 Resistance change across MIT 84
4.4 Conclusion 87
References 88
Chapter 5 General Conclusion 90
List of Publications 93
Acknowledgements 95

Chapter 1
General Introduction

1.1 Background

The advancements in science and technology have led to economic development and improved the quality of human lives. However, uncontrolled development in the past centuries, which ignored impacts on the environment, has caused global environmental issues such as climate change, ozone layer depletion, and desertification, which endanger the survival of human beings. For both a more comfortable life of people and survival of human beings, the concept of sustainable development has been advocated. In 1987, the World Commission on Environment and Development [1] published a report titled "Our Common Future" in which sustainable development is defined as "development that meets the needs of the present without compromising the ability of future generations to meet their own needs." To date, many efforts have been made by the civil society, academia, and industry to realize sustainable development.

However, sustainable development has not been achieved yet. The consumption for fossil fuels such as coal, oil, and natural gas has been increasing over the years (Figure 1-1) [2]; the total global energy consumption has increased by ~1.5 times in the past 25 years. Increasing fossil fuel consumption leads to an increase in CO_2 emissions, causing global warming. The sixth assessment report of the Intergovernmental Panel on Climate Change (IPCC) [3] has estimated the increase in human-caused global surface temperature from 1850–1900 to 2010–2019 to be 1.07 °C. The report also indicates that, as a result of global warming, the frequency of extreme temperature events, heavy 1-day precipitation events, and agricultural and ecological drought events, which occurred once in 10 years on average now likely occur 2.8, 1.3, and 1.7 times, respectively. Moreover, the global surface temperature will continue to increase, and these disasters will likely occur more frequently in future [3]. Hence, greater efforts need to be made to achieve sustainable development.

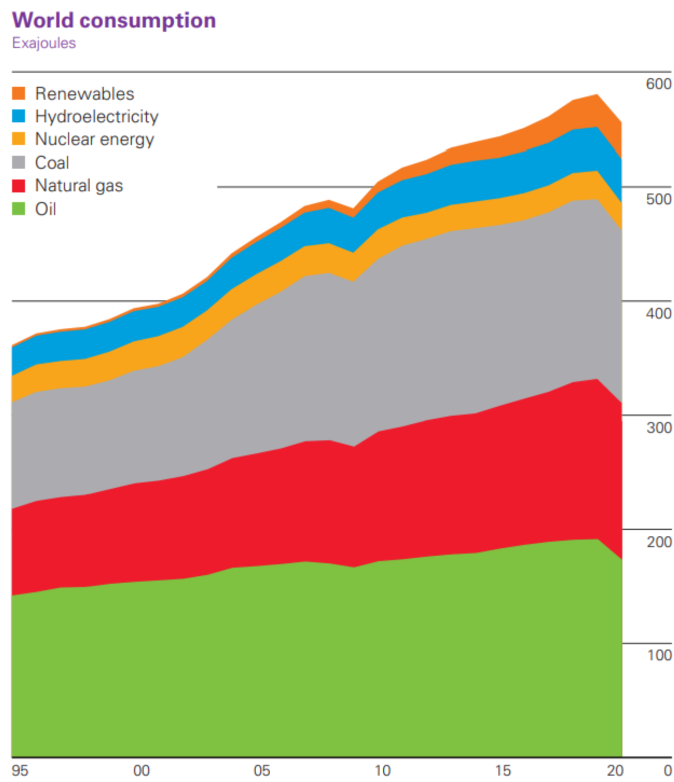

Figure 1-1 World energy consumption from 1995 to 2020 [2].

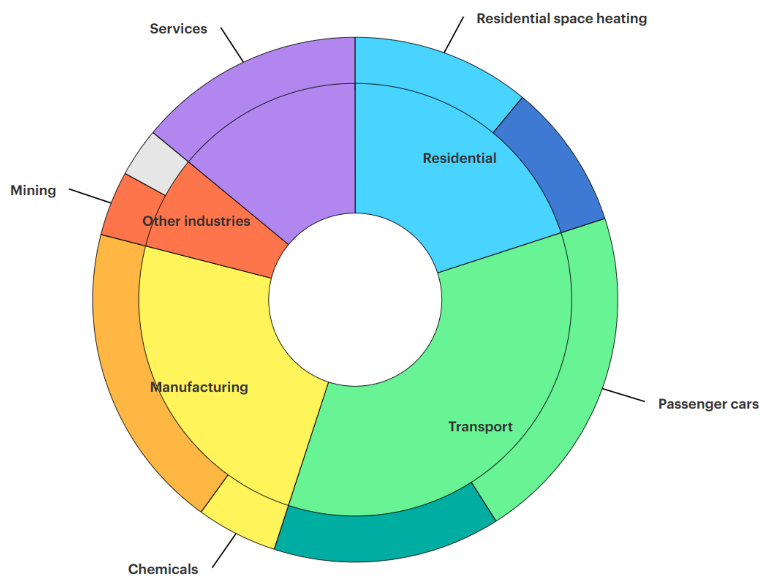

Figure 1-2 End uses of energy by sector in selected IEA countries, for which data are available for most end-uses [4].

Reducing the energy consumption of manufacturing processes is essential for sustainable development. The International Energy Agency (IEA) has reported the breakdown of end-uses of energy by sector in selected IEA countries [4]. As shown in Figure 1-2, manufacturing accounts for 24% of the end-uses of energy, suggesting that the manufacturing industry constitutes a significant proportion of the total global energy consumption. Replacing the currently used manufacturing processes that consume much energy with those that consume less energy is desirable for sustainable development.

Product performance and manufacturing cost are the limitations that hinder the introduction of manufacturing processes that consume less energy. Processes consuming low energy often have low productivity, leading to high manufacturing costs, or are not capable of fabricating products with sufficient performance that meet people's demands. Therefore, developing novel manufacturing processes that enable the fabrication of products with adequate performance while consuming lower energy and having lower manufacturing costs is desirable.

1.2 Thin Films Fabrication via Chemical Vapor Deposition

Thin film materials used in numerous products such as mobile devices, home electronics, and transport equipment are indispensable to our lives. In addition, thin film materials are expected to make our life more comfortable since they are key materials for building next-generation products, such as Internet of Things (IoT) devices and ultra-fast mobile communication systems. Therefore, the fabrication of thin films is essential for current and future manufacturing industries.

Chemical vapor deposition (CVD) is a common fabrication method for thin films. In conventional CVD, a vapor phase precursor is transferred to a heated substrate by gas. Then, chemical reactions induced by heat, light, or plasma occur near the substrate, forming film on the surface. CVD is extremely useful because it can fabricate dense films on substrates having complex shapes and can control the composition of films easily. CVD has been widely used in the industries to deposit thin films, such as silicon for solar cells, insulating films (SiO_2 and SiN) for electronic devices, and wear-resistant TiC coating for industrial tools [5].

However, CVD processes often require a vacuum environment to volatilize

precursor materials or application of plasma to induce chemical reactions, resulting in high energy consumption. To achieve sustainable development, a novel CVD technology that enables film deposition with low energy consumption is required.

1.3 Mist CVD Method

Mist CVD [6–11], also known as aerosol-assisted CVD, is a type of CVD. In this method, a solution dissolving metal salt is used as a precursor rather than a highly volatile material. The precursor solution is ultrasonically atomized to create a mist, which is transferred to a heated substrate by using a carrier gas, thereby forming a thin film on the substrate by chemical reaction.

Mist CVD can be used to fabricate films without using vacuum equipment or application of high energy such as plasma. Thus, this process can be used to fabricate films at lower energy consumption and at lower manufacturing cost. Mist CVD has similar advantages as conventional CVD, such as the ability to deposit films on substrates having complex shapes [12] and to control the composition of the film [13]. Owing to these advantages, mist CVD has been studied as the fabrication method for a variety of materials such as metals [14,15], oxides [6,7,11,16–18], sulfides [19–21], nitrides [22], and carbides [23].

The mist CVD method is primarily used for fabricating oxide thin films because the oxygen invasion from the ambient atmosphere into the reactor unit does not cause severe deterioration of the film's properties. To date, oxide thin films with excellent properties have been fabricated using this method, e.g., dielectric AlO_x [24–26], transparent conductive layer ZnO [17] and SnO_2 [27], wide-bandgap semiconductor Ga_2O_3 [7,28], and amorphous oxide semiconductor IGZO [29]. Using these films, high-performance devices such as Ga_2O_3-based Schottky barrier diodes with high breakdown voltage and low resistance have been reported [30]. These examples indicate that mist CVD is a promising fabrication method for high-performance devices using oxide thin films.

There are three types of mist CVD according to the configuration of the reactor unit: linear-source, fine-channel, and hot-wall types. In this study, hot-wall-type mist CVD, in which the substrate is heated in an electric furnace, is used (Chapter 2 details the

apparatus and procedure of the hot-wall-type mist CVD). The hot-wall-type mist CVD system is suitable for depositing crystalline films because of its ability to deposit films at high temperatures (up to 1000 °C).

1.4 MoO_2 and VO_2

Molybdenum dioxide (MoO_2) and vanadium dioxide (VO_2) have been investigated for their unique properties and potential use in next-generation electric and optical devices. Although various deposition methods have been proposed for these materials, some issues are associated with the properties of the resulting films, energy consumption, and the manufacturing cost of the process. The details of the properties, applications, and fabrication methods of these films are described below.

1.4.1 MoO_2

MoO_2 demonstrates high chemical stability against acids and bases [31], high electrical conductivity (~10^4 S cm^{-1}) [32,33], and a high work function (~6 eV) [34,35]. These properties make MoO_2 a suitable candidate for applications such as secondary batteries [36–38], hydrogen evolution catalysts [39], memory devices [32], and base layers for heteroepitaxy of other functional oxides [40]. For example, MoO_2 decorated with a 0.5 wt. % Pt shows greater mass activity than commercial 20 wt. % Pt/C catalyst, suggesting its potential to reduce the loading amount of Pt in electrocatalysts [41].

MoO_2 thin films are typically fabricated by CVD, physical vapor deposition (PVD), and solution processes [32,33,40,42–49]. Table 1-1 shows the electrical conductivity of MoO_2 films deposited by various methods. Conventional CVD and PVD such as pulsed laser deposition (PLD) and sputtering can be used to fabricate MoO_2 films with high electrical conductivity. However, they generally require vacuum equipment, which leads to high energy consumption and high manufacturing costs. Solution processes can deposit MoO_2 with lower energy consumption, but the electrical conductivity of the obtained films is not high [45]. Therefore, a novel deposition method is required to fabricate highly conductive MoO_2 films with low energy consumption and low manufacturing cost.

Table 1-1 Electrical conductivity of MoO_2 films deposited by different methods

Fabrication method	Electrical conductivity ($\times 10^3$ S cm^{-1})	Reference
PLD	6.3	[32]
PLD	11	[33]
PLD	1.4	[40]
Sputtering	1.4	[42]
Sputtering	2.3	[46]
Sputtering	3.0	[47]
CVD	0.48	[44]
CVD	6.0	[48]
Solution process	0.1	[45]

In some reports [33,43], the deposited film is denoted as MoO_x to express the stoichiometry of the resulting films, even though the crystal structure of the film corresponds to MoO_2. In this study, molybdenum oxide films with the crystal structure of MoO_2 are denoted as MoO_2 for simplicity.

1.4.2 VO_2

VO_2 shows a metal-to-insulator transition (MIT) at a phase transition temperature (T_c) of ~68 °C [50–52]. VO_2 has a monoclinic phase below T_c, and a tetragonal rutile phase above T_c. The phase transition from the monoclinic phase to the rutile phase is accompanied by a large decrease in resistivity of more than four orders of magnitude as well as a large decrease in transmittance in the infrared region [53,54]. The phase transition is triggered by various stimuli, such as voltage application [55], light irradiation [56,57], and electrolyte gating [58,59], in addition to heating and cooling. These properties of VO_2 render it suitable for potential application in optical switching devices [60], smart windows [52,61], actuators [62], and strain sensors [63]. For example, VO_2-based smart windows show great potential for saving energy in building air conditioning. Gao et al. [52] built two model house: one with non-coated glass and the other with VO_2-coated glass. They then irradiated the houses with infrared light and measured the

temperature in the houses. The temperature rise in the house with VO_2 coated glass was reduced by 9 °C compared with the house with non-coated glass, suggesting the capability of VO_2 to block infrared light significantly.

High-quality VO_2 films showing a large change in resistivity and infrared transmittance across the MIT are desirable for the above-mentioned applications. However, a fabrication method for high-quality VO_2 with low energy consumption and low manufacturing cost has not been developed yet. Fabrication methods of VO_2 thin films using CVD, PVD, and solution processes have been reported [64–69]. Conventional CVD and PVD can fabricate VO_2 films showing large resistivity changes across the MIT, but they often require vacuum equipment, incurring high energy consumption and high manufacturing costs. Solution processes can fabricate VO_2 films showing large transmittance changes across the MIT while maintaining high visible transmittance, but these processes require long-time reactions (typically over 6 h) resulting in high manufacturing costs [64,65,70]. Therefore, it is desirable to develop a method to fabricate VO_2 films with lower energy consumption and reduced manufacturing cost.

1.5 Mist CVD Application to MoO_2 and VO_2

Mist CVD is a promising method for fabricating oxide films with low energy consumption and lower manufacturing cost. To date, the mist CVD method has been primarily used to deposit metal oxides, in which the metal atoms have a maximum oxidation number (e.g., Ga_2O_3 and ZnO). On the other hand, strategies for fabricating metal oxides whose oxidation numbers are different from the maximum oxidation number (e.g., MoO_2 and VO_2) have not been successful because of the difficulty in obtaining objective valent metal oxides. In the case of molybdenum and vanadium, which have multiple oxidation states, the contamination of the unintentional valent atoms causes a deterioration of the MoO_2 and VO_2 films [33,71]. There are a few reports on using mist CVD for MoO_2 and VO_2; however, the resulting films show inferior properties compared to those prepared by other processes [72–78]. The properties of mist-CVD-grown MoO_2 and VO_2 need to be improved to facilitate their practical application.

1.6 Aims and Outline of This Thesis

MoO_2 and VO_2 are promising materials for use in next-generation devices. Although mist CVD methods can be used to fabricate MoO_2 and VO_2 thin films at lower energy consumption and at lower manufacturing costs, high-quality MoO_2 and VO_2 films have not been fabricated using this method. Therefore, the author aims to fabricate MoO_2 and VO_2 films with excellent properties using mist CVD.
This thesis is organized as follows:

Chapter 2 Growth of MoO_2 thin films

Chapter 2 details the growth of MoO_2 by mist CVD using a methanol solution of bis(acetylacetonato) molybdenum dioxide. Films deposited at various positions in a furnace at different furnace temperatures were investigated. The phase, morphology, oxidation state, and electrical resistivity of the obtained films were evaluated by X-ray diffraction (XRD), scanning electron microscopy (SEM), X-ray photoelectron spectroscopy (XPS), and four-probe methods, respectively.

Chapter 3 Growth of VO_2 thin films

Chapter 3 details the growth of VO_2 by mist CVD using a methanol and water solution of vanadyl acetylacetonate. The influence of the solvent of the precursor solution on the phase of the resulting films was investigated. XRD, XPS, SEM, four-probe method, and UV-Vis-NIR spectroscopy were used to characterize the phase, oxidation states, morphology, electrical properties, and optical properties respectively.

Chapter 4 VO_2 fabrication via topotactic oxidation

Chapter 4 details the VO_2 fabrication using the topotactic oxidation of V_2O_3 epitaxial films prepared using the mist CVD method. The precursor V_2O_3 epitaxial films were thermally oxidized at different temperatures and durations to obtain highly oriented VO_2. The phase, morphology, and electrical properties of the resulting films were investigated using XRD, SEM, and the two-probe method, respectively. In addition, the mechanism that determines the orientation of the resulting VO_2 is discussed.

Chapter 5 General Conclusion

The conclusion of this study and future perspective are presented in Chapter 5.

References

[1] World Commission on Environment and Development, Our Common Future, Oxford, 1987. https://sustainabledevelopment.un.org/content/documents/5987our-common-future.pdf.

[2] BP, Statistical Review of World Energy, 2021. https://www.bp.com/en/global/corporate/energy-economics/statistical-review-of-world-energy.html.

[3] V. Masson-Delmotte, P. Zhai, Y. Chen, L. Goldfarb, M.I. Gomis, J.B.R. Matthews, S. Berger, M. Huang, O. Yelekçi, R. Yu, B. Zhou, E. Lonnoy, T.K. Maycock, T. Waterfield, K. Leitzell, N. Caud, IPCC, 2021: Climate Change 2021: The Physical Science Basis. Contribution of Working Group I to the Sixth Assessment Report of the Intergovernmental Panel on Climate Change, Cambridge University Press, n.d. https://www.ipcc.ch/report/ar6/wg1/.

[4] IEA, Largest end-uses of energy by sector in selected IEA countries, IEA. (2018). https://www.iea.org/data-and-statistics/charts/largest-end-uses-of-energy-by-sector-in-selected-iea-countries-2018.

[5] H.O. Pierson, Handbook of Chemical Vapor Deposition (CVD), Second Edi, William Andrew Publishing, 1999.

[6] T. Ikenoue, S. Sakamoto, Y. Inui, Fabrication and characteristics of p-type Cu_2O thin films by ultrasonic spray-assisted mist CVD method, Jpn. J. Appl. Phys. 53 (2014) 05FF06. https://doi.org/10.7567/JJAP.53.05FF06.

[7] D. Shinohara, S. Fujita, Heteroepitaxy of corundum-structured α-Ga_2O_3 thin films on α-Al_2O_3 substrates by ultrasonic mist chemical vapor deposition, Jpn. J. Appl. Phys. 47 (2008) 7311–7313. https://doi.org/10.1143/JJAP.47.7311.

[8] T. Kawaharamura, H. Nishinaka, S. Fujita, Growth of crystalline zinc oxide thin films by fine-channel-mist chemical vapor deposition, Jpn. J. Appl. Phys. 47 (2008) 4669–4675. https://doi.org/10.1143/JJAP.47.4669.

[9] H. Nishinaka, T. Kawaharamura, S. Fujita, Low-temperature growth of ZnO thin films by linear source ultrasonic spray chemical vapor deposition, Jpn. J. Appl. Phys. 46 (2007) 6811–6813. https://doi.org/10.1143/JJAP.46.6811.

[10] H. Ito, K. Kaneko, S. Fujita, Growth and band gap control of corundum-structured α-$(AlGa)_2O_3$ thin films on sapphire by spray-assisted mist chemical vapor deposition, Jpn. J. Appl. Phys. 51 (2012) 100207. https://doi.org/10.1143/JJAP.51.100207.

[11] T. Uchida, T. Kawaharamura, K. Shibayama, T. Hiramatsu, H. Orita, S. Fujita, Mist chemical vapor deposition of aluminum oxide thin films for rear surface passivation of crystalline silicon solar cells, Appl. Phys. Express. 7 (2014) 021303.

https://doi.org/10.7567/APEX.7.021303.

[12] M.A. Ehsan, A. Khan, Aerosol-Assisted Chemical Vapor Deposition Growth of $NiMoO_4$ Nanoflowers on Nickel Foam as Effective Electrocatalysts toward Water Oxidation, ACS Omega. 6 (2021) 31339–31347. https://doi.org/10.1021/acsomega.1c05209.

[13] T. Ikenoue, S. Yoneya, M. Miyake, T. Hirato, Epitaxial Growth and Bandgap Control of $Ni_{1-x}Mg_xO$ Thin Film Grown by Mist Chemical Vapor Deposition Method, MRS Adv. 5 (2020) 1705–1712. https://doi.org/10.1557/adv.2020.219.

[14] M.A. Ehsan, M. Younas, A. Rehman, M. Altaf, M.Y. Khan, A. Al-Ahmed, S. Ahmad, A.A. Isab, Synthesis and utilization of platinum(II) dialkyldithiocarbamate precursors in aerosol assisted chemical vapor deposition of platinum thin films as counter electrodes for dye-sensitized solar cells, Polyhedron. 166 (2019) 186–195. https://doi.org/10.1016/j.poly.2019.03.058.

[15] Y. Nakabayashi, H. Sakai, R. Suzuki, S. Yamada, Formation of silver particles for SERS spectroscopy by mist chemical vapor deposition method, Jpn. J. Appl. Phys. 58 (2019) 120908. https://doi.org/10.7567/1347-4065/ab5482.

[16] B.-H. Kim, J.-Y. Lee, Y.-H. Choa, M. Higuchi, N. Mizutani, Preparation of TiO_2 thin film by liquid sprayed mist CVD method, Mater. Sci. Eng. B. 107 (2004) 289–294. https://doi.org/10.1016/j.mseb.2003.12.010.

[17] J.G. Lu, T. Kawaharamura, H. Nishinaka, Y. Kamada, T. Ohshima, S. Fujita, ZnO-based thin films synthesized by atmospheric pressure mist chemical vapor deposition, J. Cryst. Growth. 299 (2007) 1–10. https://doi.org/10.1016/j.jcrysgro.2006.10.251.

[18] J. Piao, S. Katori, T. Kawaharamura, C. Li, S. Fujita, Fabrication of Silicon Oxide Thin Films by Mist Chemical Vapor Deposition Method from Polysilazane and Ozone as Sources, Jpn. J. Appl. Phys. 51 (2012) 090201. https://doi.org/10.1143/JJAP.51.090201.

[19] K. Uno, Y. Yamasaki, I. Tanaka, Growth mechanisms of zinc oxide and zinc sulfide films by mist chemical vapor deposition, Appl. Phys. Express. 10 (2017) 015502. https://doi.org/10.7567/APEX.10.015502.

[20] K. Tanaka, M. Kowata, F. Yoshihisa, S. Imai, W. Yamazaki, Preparation of monoclinic Cu_2SnS_3 thin films by fine channel mist chemical vapor deposition method, Thin Solid Films. 697 (2020) 137820. https://doi.org/10.1016/j.tsf.2020.137820.

[21] M.A. Ehsan, A. Rehman, A. Afzal, A. Ali, A.S. Hakeem, U.A. Akbar, N. Iqbal, Highly Effective Electrochemical Water Oxidation by Millerite-Phased Nickel Sulfide Nanoflakes Fabricated on Ni Foam by Aerosol-Assisted Chemical Vapor Deposition, Energy & Fuels. 35 (2021) 16054–16064. https://doi.org/10.1021/acs.energyfuels.1c02186.

[22] T. Yamaguchi, H. Nagai, T. Kiguchi, N. Wakabayashi, T. Igawa, T. Hitora, T. Onuma, T. Honda, M. Sato, Epitaxial mist chemical vapor deposition growth and characterization of

Cu_3N films on (0001) α-Al_2O_3 substrates, Appl. Phys. Express. 13 (2020) 075505. https://doi.org/10.35848/1882-0786/ab9a8f.

[23] T. Ikenoue, T. Yoshida, M. Miyake, R. Kasada, T. Hirato, Fabrication and mechanical properties of tungsten carbide thin films via mist chemical vapor deposition, J. Alloys Compd. 829 (2020) 154567. https://doi.org/10.1016/J.JALLCOM.2020.154567.

[24] T. Uchida, T. Kawaharamura, K. Shibayama, T. Hiramatsu, H. Orita, S. Fujita, Mist chemical vapor deposition of aluminum oxide thin films for rear surface passivation of crystalline silicon solar cells, Appl. Phys. Express. 7 (2014) 021303. https://doi.org/10.7567/APEX.7.021303.

[25] T. Kawaharamura, T. Uchida, M. Sanada, M. Furuta, Growth and electrical properties of AlO_x grown by mist chemical vapor deposition, AIP Adv. 3 (2013) 032135. https://doi.org/10.1063/1.4798303.

[26] T. Kawaharamura, T. Uchida, D. Wang, M. Sanada, M. Furuta, Enhancing carrier mobility of IGZO TFT fabricated by non-vacuum mist CVD with O_3 assistance, Phys. Status Solidi. 10 (2013) 1565–1568. https://doi.org/10.1002/PSSC.201300247.

[27] J.I. Scott, R.F. Martinez-Gazoni, M.W. Allen, R.J. Reeves, Optical and electronic properties of high quality Sb-doped SnO_2 thin films grown by mist chemical vapor deposition, J. Appl. Phys. 126 (2019) 135702. https://doi.org/10.1063/1.5116719.

[28] G.T. Dang, T. Kawaharamura, M. Furuta, M.W. Allen, Mist-CVD grown Sn-doped α-Ga_2O_3 MESFETs, IEEE Trans. Electron Devices. 62 (2015) 3640–3644. https://doi.org/10.1109/TED.2015.2477438.

[29] M. Furuta, T. Kawaharamura, D. Wang, T. Toda, T. Hirao, Electrical properties of the thin-film transistor with an indium-gallium-zinc oxide channel and an aluminium oxide gate dielectric stack formed by solution-based atmospheric pressure deposition, IEEE Electron Device Lett. 33 (2012) 851–853. https://doi.org/10.1109/LED.2012.2192902.

[30] K. Kaneko, S. Fujita, T. Hitora, A power device material of corundum-structured α-Ga_2O_3 fabricated by MIST EPITAXY ® technique, Jpn. J. Appl. Phys. 57 (2018) 02CB18. https://doi.org/10.7567/JJAP.57.02CB18.

[31] Q. Zhang, X. Li, Q. Ma, Q. Zhang, H. Bai, W. Yi, J. Liu, J. Han, G. Xi, A metallic molybdenum dioxide with high stability for surface enhanced Raman spectroscopy, Nat. Commun. 8 (2017) 14903. https://doi.org/10.1038/ncomms14903.

[32] W. Lee, C.J. Cho, W.C. Lee, C.S. Hwang, R.P.H. Chang, S.K. Kim, MoO_2 as a thermally stable oxide electrode for dynamic random-access memory capacitors, J. Mater. Chem. C. 6 (2018) 13250–13256. https://doi.org/10.1039/C8TC04167A.

[33] V. Bhosle, A. Tiwari, J. Narayan, Epitaxial growth and properties of $MoO_x(2<x<2.75)$ films, J. Appl. Phys. 97 (2005) 083539. https://doi.org/10.1063/1.1868852.

[34] W.-J. Lee, N.S. Parmar, J.-W. Choi, High work function MoO_2 and ReO_2 contacts for p-type Si and GaN by a room-temperature non-vacuum process, Mater. Sci. Semicond. Process. 71 (2017) 374–377. https://doi.org/10.1016/j.mssp.2017.08.034.

[35] C.I. Wu, C.T. Lin, G.R. Lee, T.Y. Cho, C.C. Wu, T.W. Pi, Electronic and chemical properties of molybdenum oxide doped hole injection layers in organic light emitting diodes, J. Appl. Phys. 105 (2009) 033717. https://doi.org/10.1063/1.3077170.

[36] Y. Xu, R. Yi, B. Yuan, X. Wu, M. Dunwell, Q. Lin, L. Fei, S. Deng, P. Andersen, D. Wang, H. Luo, High Capacity MoO_2 /Graphite Oxide Composite Anode for Lithium-Ion Batteries, J. Phys. Chem. Lett. 3 (2012) 309–314. https://doi.org/10.1021/jz201619r.

[37] Y. Sun, X. Hu, W. Luo, Y. Huang, Self-assembled hierarchical MoO_2/graphene nanoarchitectures and their application as a high-performance anode material for lithium-ion batteries, ACS Nano. 5 (2011) 7100–7107. https://doi.org/10.1021/nn201802c.

[38] F. Xia, X. Hu, Y. Sun, W. Luo, Y. Huang, Layer-by-layer assembled MoO_2–graphene thin film as a high-capacity and binder-free anode for lithium-ion batteries, Nanoscale. 4 (2012) 4707. https://doi.org/10.1039/c2nr30742a.

[39] H. Zeng, S. Chen, Y.Q. Jin, J. Li, J. Song, Z. Le, G. Liang, H. Zhang, F. Xie, J. Chen, Y. Jin, X. Chen, H. Meng, Electron Density Modulation of Metallic MoO_2 by Ni Doping to Produce Excellent Hydrogen Evolution and Oxidation Activities in Acid, ACS Energy Lett. 5 (2020) 1908–1915. https://doi.org/10.1021/acsenergylett.0c00642.

[40] C.-H. Ma, J.-C. Lin, H.-J. Liu, T.H. Do, Y.-M. Zhu, T.D. Ha, Q. Zhan, J.-Y. Juang, Q. He, E. Arenholz, P.-W. Chiu, Y.-H. Chu, Van der Waals epitaxy of functional MoO_2 film on mica for flexible electronics, Appl. Phys. Lett. 108 (2016) 253104. https://doi.org/10.1063/1.4954172.

[41] X. Li, J. Yu, J. Jia, A. Wang, L. Zhao, T. Xiong, H. Liu, W. Zhou, Confined distribution of platinum clusters on MoO_2 hexagonal nanosheets with oxygen vacancies as a high-efficiency electrocatalyst for hydrogen evolution reaction, Nano Energy. 62 (2019) 127–135. https://doi.org/10.1016/j.nanoen.2019.05.013.

[42] E. Ahn, Y.-S. Seo, J. Cho, I. Lee, J. Hwang, H. Jeen, Epitaxial growth and metallicity of rutile MoO_2 thin film, RSC Adv. 6 (2016) 60704–60708. https://doi.org/10.1039/C6RA09928A.

[43] C. Liu, Z. Li, Z. Zhang, MoO_x thin films deposited by magnetron sputtering as an anode for aqueous micro-supercapacitors, Sci. Technol. Adv. Mater. 14 (2013) 065005. https://doi.org/10.1088/1468-6996/14/6/065005.

[44] E. Pu, D. Liu, P. Ren, W. Zhou, D. Tang, B. Xiang, Y. Wang, J. Miao, Ultrathin MoO_2 nanosheets with good thermal stability and high conductivity, AIP Adv. 7 (2017) 025015. https://doi.org/10.1063/1.4977543.

[45] Y. Shi, B. Guo, S.A. Corr, Q. Shi, Y.-S. Hu, K.R. Heier, L. Chen, R. Seshadri, G.D. Stucky, Ordered mesoporous metallic MoO_2 materials with highly reversible lithium storage capacity, Nano Lett. 9 (2009) 4215–4220. https://doi.org/10.1021/nl902423a.

[46] E. Ahn, T. Min, J. Lee, I. Lee, Y. Kim, H. Jeen, Role of surface oxidation for thickness-driven insulator-to-metal transition in epitaxial MoO_2 films, Appl. Surf. Sci. 459 (2018) 92–97. https://doi.org/10.1016/j.apsusc.2018.07.188.

[47] K. Fujiwara, A. Tsukazaki, Formation of distorted rutile-type NbO_2, MoO_2, and WO_2 films by reactive sputtering, J. Appl. Phys. 125 (2019) 085301. https://doi.org/10.1063/1.5079719.

[48] Q. Xie, X. Zheng, D. Wu, X. Chen, J. Shi, X. Han, X. Zhang, G. Peng, Y. Gao, H. Huang, High electrical conductivity of individual epitaxially grown MoO_2 nanorods, Appl. Phys. Lett. 111 (2017) 093505. https://doi.org/10.1063/1.5001183.

[49] O. de Melo, Y. González, A. Climent-Font, P. Galán, A. Ruediger, M. Sánchez, C. Calvo-Mola, G. Santana, V. Torres-Costa, Optical and electrical properties of MoO_2 and MoO_3 thin films prepared from the chemically driven isothermal close space vapor transport technique, J. Phys. Condens. Matter. 31 (2019) 295703. https://doi.org/10.1088/1361-648X/ab18e2.

[50] Y. Zhang, W. Xiong, W. Chen, Y. Zheng, Recent Progress on Vanadium Dioxide Nanostructures and Devices: Fabrication, Properties, Applications and Perspectives, Nanomaterials. 11 (2021) 338. https://doi.org/10.3390/nano11020338.

[51] V. Devthade, S. Lee, Synthesis of vanadium dioxide thin films and nanostructures, J. Appl. Phys. 128 (2020) 231101. https://doi.org/10.1063/5.0027690.

[52] Y. Gao, H. Luo, Z. Zhang, L. Kang, Z. Chen, J. Du, M. Kanehira, C. Cao, Nanoceramic VO_2 thermochromic smart glass: A review on progress in solution processing, Nano Energy. 1 (2012) 221–246. https://doi.org/10.1016/j.nanoen.2011.12.002.

[53] D. Kucharczyk, T. Niklewski, Accurate X-ray determination of the lattice parameters and the thermal expansion coefficients of VO_2 near the transition temperature, J. Appl. Crystallogr. 12 (1979) 370–373. https://doi.org/10.1107/S0021889879012711.

[54] K. Liu, S. Lee, S. Yang, O. Delaire, J. Wu, Recent progresses on physics and applications of vanadium dioxide, Mater. Today. 21 (2018) 875–896. https://doi.org/10.1016/j.mattod.2018.03.029.

[55] Y. Zhou, X. Chen, C. Ko, Z. Yang, C. Mouli, S. Ramanathan, Voltage-triggered ultrafast phase transition in vanadium dioxide switches, IEEE Electron Device Lett. 34 (2013) 220–222. https://doi.org/10.1109/LED.2012.2229457.

[56] M.F. Becker, A.B. Buckman, R.M. Walser, T. Lépine, P. Georges, A. Brun, Femtosecond laser excitation dynamics of the semiconductor-metal phase transition in VO_2, J. Appl. Phys. 79 (1996) 2404–2408. https://doi.org/10.1063/1.361167.

[57] A. Cavalleri, C. Tóth, C.W. Siders, J.A. Squier, F. Ráksi, P. Forget, J.C. Kieffer,

Femtosecond structural dynamics in VO_2 during an ultrafast solid-solid phase transition, Phys. Rev. Lett. 87 (2001) 237401. https://doi.org/10.1103/PhysRevLett.87.237401.

[58] C. Wu, F. Feng, J. Feng, J. Dai, L. Peng, J. Zhao, J. Yang, C. Si, Z. Wu, Y. Xie, Hydrogen-Incorporation Stabilization of Metallic VO_2(R) Phase to Room Temperature, Displaying Promising Low-Temperature Thermoelectric Effect, J. Am. Chem. Soc. 133 (2011) 13798–13801. https://doi.org/10.1021/JA203186F.

[59] J. Park, C. Oh, J. Son, Anisotropic ionic transport-controlled synaptic weight update by protonation in a VO_2 transistor, J. Mater. Chem. C. 9 (2021) 2521–2529. https://doi.org/10.1039/D0TC05628F.

[60] H. Zhou, J. Li, Y. Xin, G. Sun, S. Bao, P. Jin, Optical and electrical switching properties of VO_2 thin film on MgF_2 (111) substrate, Ceram. Int. 42 (2016) 7655–7663. https://doi.org/10.1016/j.ceramint.2016.01.178.

[61] Y. Cui, Y. Ke, C. Liu, Z. Chen, N. Wang, L. Zhang, Y. Zhou, S. Wang, Y. Gao, Y. Long, Thermochromic VO_2 for Energy-Efficient Smart Windows, Joule. 2 (2018) 1707–1746. https://doi.org/10.1016/j.joule.2018.06.018.

[62] R. Shi, X. Cai, W. Wang, J. Wang, D. Kong, N. Cai, P. Chen, P. He, Z. Wu, A. Amini, N. Wang, C. Cheng, R. Shi, W.J. Wang, J.W. Wang, D.J. Kong, N.D. Cai, P.C. Chen, C. Cheng, X.B. Cai, P.G. He, Z.F. Wu, N. Wang, A. Amini, Single-Crystalline Vanadium Dioxide Actuators, Adv. Funct. Mater. 29 (2019) 1900527. https://doi.org/10.1002/ADFM.201900527.

[63] B. Hu, Y. Ding, W. Chen, D. Kulkarni, Y. Shen, V. V. Tsukruk, Z.L. Wang, External-Strain Induced Insulating Phase Transition in VO_2 Nanobeam and Its Application as Flexible Strain Sensor, Adv. Mater. 22 (2010) 5134–5139. https://doi.org/10.1002/adma.201002868.

[64] Z. Chen, Y. Gao, L. Kang, C. Cao, S. Chen, H. Luo, Fine crystalline VO_2 nanoparticles: synthesis, abnormal phase transition temperatures and excellent optical properties of a derived VO2 nanocomposite foil, J. Mater. Chem. A. 2 (2014) 2718. https://doi.org/10.1039/c3ta14612j.

[65] S.R. Popuri, M. Miclau, A. Artemenko, C. Labrugere, A. Villesuzanne, M. Pollet, Rapid Hydrothermal Synthesis of VO_2 (B) and Its Conversion to Thermochromic VO_2 (M1), Inorg. Chem. 52 (2013) 4780–4785. https://doi.org/10.1021/ic301201k.

[66] B.-G. Chae, H.-T. Kim, S.-J. Yun, B.-J. Kim, Y.-W. Lee, D.-H. Youn, K.-Y. Kang, Highly Oriented VO_2 Thin Films Prepared by Sol-Gel Deposition, Electrochem. Solid-State Lett. 9 (2006) C12. https://doi.org/10.1149/1.2135430.

[67] L. Mathevula, B.D. Ngom, L. Kotsedi, P. Sechogela, T.B. Doyle, M. Ghouti, M. Maaza, Thermochromic VO_2 on Zinnwaldite Mica by pulsed laser deposition, Appl. Surf. Sci. 314 (2014) 476–480. https://doi.org/10.1016/j.apsusc.2014.07.035.

[68] P. Jin, S. Tanemura, Formation and Thermochromism of VO_2 Films Deposited by RF Magnetron Sputtering at Low Substrate Temperature, Jpn. J. Appl. Phys. 33 (1994) 1478–1483. https://doi.org/10.1143/JJAP.33.1478.

[69] E. Gagaoudakis, E. Aperathitis, G. Michail, M. Panagopoulou, D. Katerinopoulou, V. Binas, Y.S. Raptis, G. Kiriakidis, Low-temperature rf sputtered VO_2 thin films as thermochromic coatings for smart glazing systems, Sol. Energy. 165 (2018) 115–121. https://doi.org/10.1016/j.solener.2018.03.010.

[70] M. Li, S. Magdassi, Y. Gao, Y. Long, Hydrothermal Synthesis of VO_2 Polymorphs: Advantages, Challenges and Prospects for the Application of Energy Efficient Smart Windows, Small. 13 (2017) 1701147. https://doi.org/10.1002/smll.201701147.

[71] H. Kim, N. Charipar, M. Osofsky, S.B. Qadri, A. Piqué, Optimization of the semiconductor-metal transition in VO_2 epitaxial thin films as a function of oxygen growth pressure, Appl. Phys. Lett. 104 (2014) 081913. https://doi.org/10.1063/1.4866806.

[72] C. Piccirillo, R. Binions, I.P. Parkin, Nb-Doped VO_2 Thin Films Prepared by Aerosol-Assisted Chemical Vapour Deposition, Eur. J. Inorg. Chem. 2007 (2007) 4050–4055. https://doi.org/10.1002/ejic.200700284.

[73] C. Piccirillo, R. Binions, I.P. Parkin, Synthesis and characterisation of W-doped VO_2 by Aerosol Assisted Chemical Vapour Deposition, Thin Solid Films. 516 (2008) 1992–1997. https://doi.org/10.1016/j.tsf.2007.06.009.

[74] C. Piccirillo, R. Binions, I.P. Parkin, Synthesis and functional properties of vanadium oxides: V_2O_3, VO_2, and V_2O_5 deposited on glass by aerosol-assisted CVD, Chem. Vap. Depos. 13 (2007) 145–151. https://doi.org/10.1002/cvde.200606540.

[75] P. Kiri, M.E.A. Warwick, I. Ridley, R. Binions, Fluorine doped vanadium dioxide thin films for smart windows, Thin Solid Films. 520 (2011) 1363–1366. https://doi.org/10.1016/j.tsf.2011.01.401.

[76] M.E.A. Warwick, R. Binions, Thermochromic vanadium dioxide thin films from electric field assisted aerosol assisted chemical vapour deposition, Sol. Energy Mater. Sol. Cells. 143 (2015) 592–600. https://doi.org/10.1016/j.solmat.2015.01.025.

[77] I. Top, R. Binions, M.E.A. Warwick, C.W. Dunnill, M. Holdynski, I. Abrahams, VO_2/TiO_2 bilayer films for energy efficient windows with multifunctional properties, J. Mater. Chem. C. 6 (2018) 4485–4493. https://doi.org/10.1039/C8TC00835C.

[78] S. Ashraf, C.S. Blackman, G. Hyett, I.P. Parkin, Aerosol assisted chemical vapour deposition of MoO_3 and MoO_2 thin films on glass from molybdenum polyoxometallate precursors; thermophoresis and gas phase nanoparticle formation, J. Mater. Chem. 16 (2006) 3575. https://doi.org/10.1039/b607335b.

Chapter 2
Mist Chemical Vapor Deposition of MoO_2 Thin Films

2.1 Introduction

In this chapter, the author reports the fabrication of MoO_2 thin films using the mist CVD method. Ashraf et al. performed mist CVD of MoO_2 using polyoxometalates as the precursor [1], but only obtained rough, sparse, and powdery MoO_2. However, dense oxide films with flat surfaces of Ga_2O_3, NiO, Cu_2O, and $LiMn_2O_4$ have been obtained by mist CVD using metal acetylacetonates as the precursor [2–5]. Mist CVD of MoO_2 using metal acetylacetonates as the precursor has not been reported before. In this chapter, the author reports mist CVD using bis(acetylacetonato) molybdenum dioxide as the precursor to obtain flat MoO_2 films. Optimal deposition conditions including the deposition temperature and the position of the substrate in the reactor were determined by examining the crystal phase, morphology, and electrical resistivity of the resulting films.

2.2 Experimental

2.2.1 Materials

The precursor solution was prepared by dissolving 0.65 g of bis(acetylacetonato) molybdenum (VI) dioxide ($MoO_2(acac)_2$; Wako) in 80 mL of methanol containing 0.1 wt. % water. The concentration of water in methanol (99.8%, Wako) was measured using a Karl Fischer coulometer (KEM Kyoto, MKC-610) and was adjusted to be 0.1 wt. % by the addition of distilled water. The precursor solution was stirred for 6 h in a sealed container in dark and then used for mist CVD. Glass slides (Matsunami; 25 mm × 76 mm, thickness: 1.0–1.2 mm) and quartz plates (26 mm × 76 mm; thickness: 1.0 mm) were used as the substrate for the MoO_2 films. Prior to their use, the substrates were cleaned with acetone, distilled water, and isopropanol using an ultrasonic bath and dried by blowing air.

2.2.2 Mist CVD of MoO_2

A custom-built hot-wall mist CVD system (Figure 2-1a) was used for the deposition of MoO_2 films. The system consists of a unit for generating the precursor mist and a reactor unit for film deposition. The precursor solution was taken in a glass cylinder (ϕ 95 mm) with a plastic film (~10 μm in thickness) covering the bottom of the cylinder, and the cylinder containing the solution was placed in a water bath, underneath which three ultrasonic atomizers (HM-2412, Honda Electronics) were installed. The mist of the precursor solution was generated by the ultrasonic vibration of the atomizers. The generated mist particles were transported to the reactor unit by a carrier gas (N_2). Additional N_2 gas was flown from the mist generator unit to the reactor unit to dilute the precursor mist in the gas flow. In the reactor unit, the substrates were placed in a quartz tube with an inner diameter of 40 mm and heated by an electric tube furnace (ϕ 51 mm × 300 mm, ARF-50KC, Asahi Rika Seisakusyo). Films were formed on the substrates through thermal decomposition of the precursor mist. Three pieces of the substrates were placed in the quartz tube side-by-side to cover the distance of 4–27 cm from the furnace inlet. The furnace temperature was monitored with a thermocouple attached to the outer

wall of the quartz tube at the central part of the furnace, and the furnace temperature was maintained at a given value in the range of 400–550 °C.

The film deposition procedure is as follows: After placing the substrates in the quartz tube, the furnace was heated to a predetermined temperature and the quartz tube was purged with N_2. With the N_2 gas remaining in the furnace, the precursor solution was atomized for 5 min to stabilize the atomizers. Then, the carrier gas (N_2) and diluting gas (N_2) were flown at the rates of 4 and 2 L min^{-1}, respectively, and thus the mist was transported to the substrates in the furnace to start film deposition. After 10 min of film deposition, the carrier gas, atomizers, and furnace were turned off, while the flow of the diluting gas was continued. Finally, the substrates were cooled to room temperature (~ 25 °C) in the furnace under N_2 gas flow.

The temperature distribution on the substrate surface was measured almost under the same conditions as those during the film deposition; however, a mist of methanol without $MoO_2(acac)_2$ was flown during this measurement. A thermocouple inserted from the end of the quartz tube was used to measure the temperature of the glass substrate surface. The temperature was recorded 10 min after the start of the mist flow. Direct measurement of substrate temperature was carried out at furnace temperatures of 350–480 °C, while the substrate temperatures at furnace temperatures of 500 and 550 °C were determined by extrapolation of the data collected at the lower furnace temperatures.

2.2.3 Characterization of films

XRD was performed with an X-ray diffractometer (X'pertPRO-MPD, PANalytical) using Cu-*Kα* radiation to evaluate the phase of the deposited film. The morphology of the deposited film was observed by field emission scanning electron microscopy (SEM, IT300HR, JEOL) and atomic force microscopy (AFM, Nano Navi IIs Nanocute, SII Nano Technology). The electrical resistivity was measured at room temperature (~25 °C) by the four-probe method with an applied current of 10 μA using a source meter (2450 SourceMeter, KEITHLEY). The glass substrate after film deposition was cut into several pieces, and the resistivity of the film on each piece was measured to determine the distribution of the resistivity.

XPS was performed on a JPS-9030 spectrometer (JEOL) using a Mg *Kα* X-ray source (1253.6 eV) operated at 12.0 kV and 10.0 mA to analyze the oxidation state of the elements present in the prepared films. The base pressure of the instrument was typically less than 5×10^{-6} Pa. The XPS spectra were calibrated using the C 1s peak from hydrocarbon contamination fixed at 285.0 eV. A pass energy of 50 eV with 1 eV step was used for collecting the wide-scan survey spectrum, while a pass energy of 30 eV with 0.2 and 0.05 eV step, respectively, was used for collecting the spectra in the C 1s and Mo 3d regions. Sputter etching of the samples was carried out using an argon ion gun operated at 400 V for 5 s with a duty ratio of 50%. Under the acceleration voltage of 400 V, a standard SiO_2 film is etched at the rate of approximately 0.3 nm s^{-1}. The XPS spectra were analyzed using SPECSURF (version 2.0.5.7, JEOL) software. The Mo 3d spectrum typically consists of two envelopes as a consequence of spin-orbit coupling. The ratio of the oxidation states of Mo in the specimens was estimated by the deconvolution of the spectra using a method suggested by Choi et al. [6] The Mo $3d_{5/2}$–Mo $3d_{3/2}$ doublet was fitted such that each peak had the same mixed Gaussian-Lorentzian line shape and width. The intensity ratio and the splitting energy for the Mo $3d_{5/2}$–Mo $3d_{3/2}$ doublet was fixed at $I(3d_{5/2})/I(3d_{3/2}) = 3/2$ and 3.15 eV, respectively. The XPS spectrum of the prepared film was compared with those of MoO_2 and MoO_3 powders. The MoO_2 powder (99.9%) was purchased from Kojundo Chemical Laboratory and the MoO_3 powder was prepared by annealing molybdenum metal powder (99.9%, Wako) in air at 500 °C for more than 8 h. These powders were confirmed to be single phases of monoclinic MoO_2 and orthogonal MoO_3 from XRD analysis.

2.3 Results and Discussion

2.3.1 Appearance of the films

The temperature of the substrate is one of the key factors that can significantly affect the quality of the resulting film in mist CVD. Figure 2-1b shows the temperature distributions over the substrate surface under the mist flow in the furnace heated to various preset temperatures in the range of 400–550 °C. At every furnace temperature, the temperature of the substrate surface was found to have the maximum value at a position slightly downstream from the center of the furnace. Without the mist flow, the maximum temperature is observed at the center, which is 15 cm from the inlet of the furnace. The quality of the resulting film is likely to be affected both by the substrate temperature and time taken by the mist to travel through the heating zone to the substrate. Therefore, the author examined the films formed at different positions in the furnace at various preset temperatures.

Figure 2-2a shows the photographs of the films formed on the glass substrates by the mist CVD at furnace temperatures of 550 and 480 °C. Films were formed over a length of >14 cm on the substrates. The films obtained at the furnace temperature of 550 °C have a dull gray appearance near the center of the substrate and a dark reflective appearance near both ends. Meanwhile, the entire film obtained at the furnace temperature of 480 °C has a uniform reflective appearance.

Figure 2-2b schematizes the appearance of the films formed at different locations in the furnace at different temperatures. No film formation was observed at a furnace temperature of 400 °C. Film deposition occurred at furnace temperatures higher than 440 °C. At the furnace temperatures of 440–500 °C, films with metallic luster (see the photograph in Figure 2-2a) were obtained, while at 550 °C, a dark mirror-like or grayish dull film was obtained.

At the furnace temperature of 440 °C, the film was formed in the range of $X = 15$ cm to 25 cm, where X is the distance from the inlet of the furnace (Figure 2-2b). The starting edge of the formed film shifted upstream as the furnace temperature was increased, and thus, the area over which the film formed increased with increasing furnace

temperature. A comparison between the temperature distribution (Figure 2-1b) and the starting edge of the formed film (Figure 2-2b) indicates that the film deposition started at the position where the substrate temperature was approximately 325 °C.

The characteristics of the films obtained at different furnace temperatures and the differences in the characteristics at different positions of a given film grown at a particular furnace temperature (the regions indicated by the circles in the diagram in Figure 2-2b) are discussed hereafter.

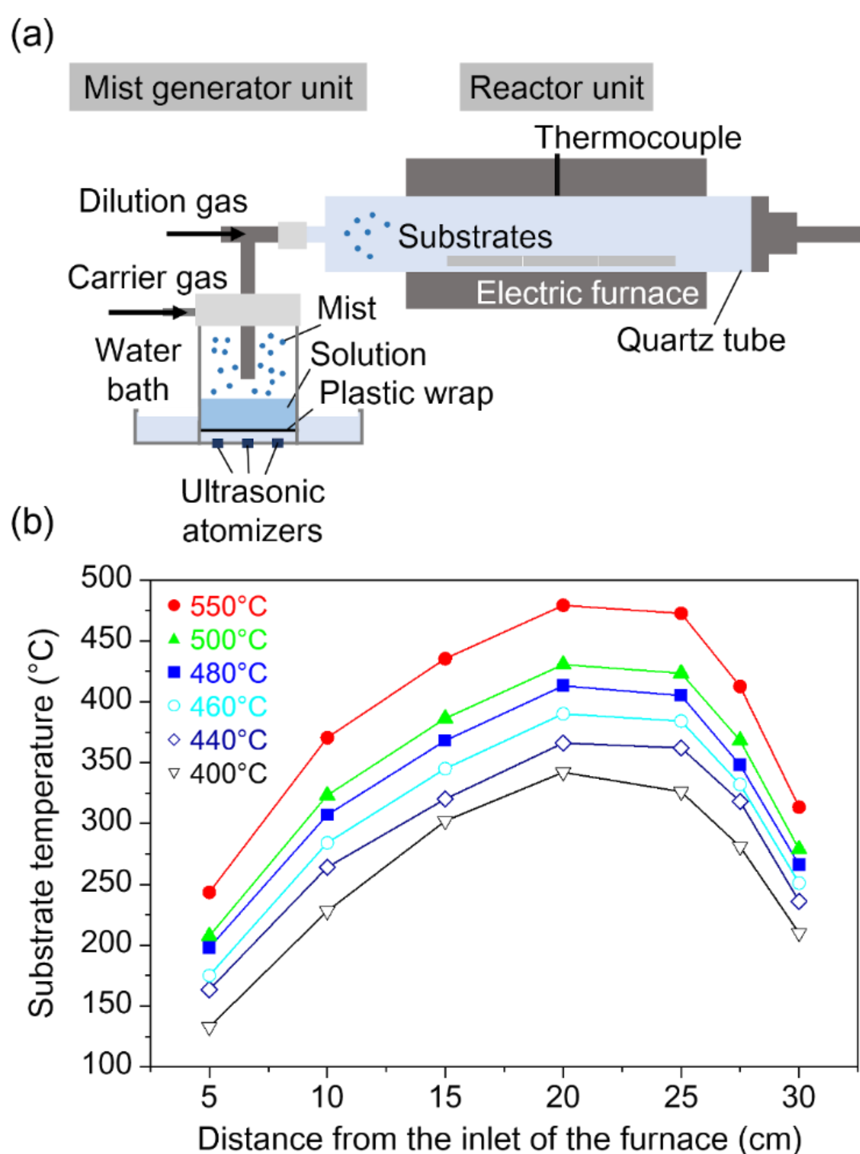

Figure 2-1 (a) Schematic illustration of a hot-wall mist CVD system. (b) Temperature distribution on the substrate under mist flow in the furnace at different preset temperatures.

(a)

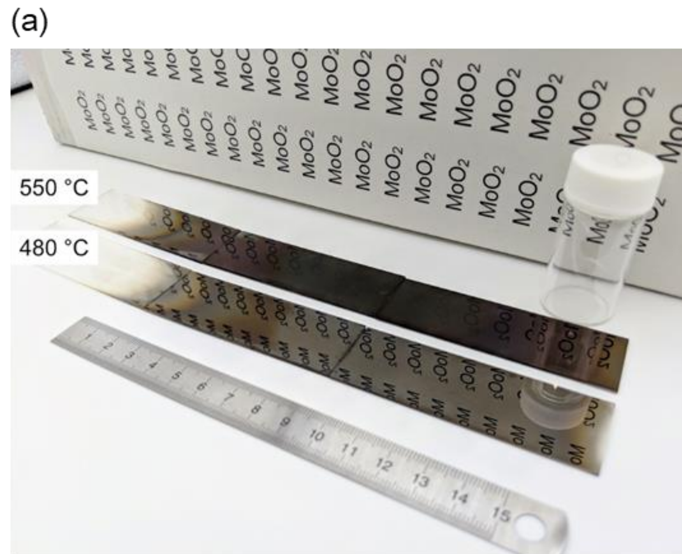

(b)

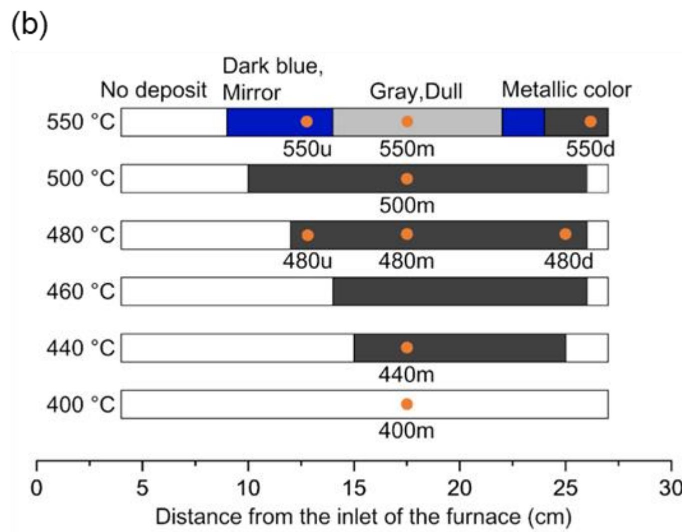

Figure 2-2 (a) Photograph of the films prepared at furnace temperatures of 550 °C (top) and 480 °C (bottom). The mist was flown in from the left side of the substrate during the process. (b) Diagram showing the physical appearance of the films deposited at different positions in the furnace at various temperatures. The circles indicate the positions of the films characterized intensively in this study.

2.3.2 Phase of films

Figure 2-3a shows the XRD patterns of the films obtained from the area near the middle of the furnace (at X = 18 cm). The XRD pattern of the sample obtained at the furnace temperature of 400 °C showed only a halo from the glass substrate, confirming that no film deposition occurred at this temperature. In the XRD patterns for films prepared at 440 °C and 480 °C, peaks are observed at 2θ = 37° and 53°, respectively. These peaks correspond to the crystal planes of monoclinic MoO_2 [7]. No diffraction peak was observed from the film at 2θ = 26°, where MoO_2 (011) diffraction peak should appear if the deposited film consists of randomly oriented grains. The film, therefore, appears to be composed of MoO_2 with a preferred orientation. The strong diffraction peak observed at 2θ = 37° can be attributed to either $(20\bar{2})$, $(21\bar{1})$, (020), or (002) plane of MoO_2. The diffraction peaks from these lattice planes are so close that it was impossible to uniquely identify the oriented lattice plane.

In the XRD patterns of the films prepared at 500 °C and 550 °C, the diffractions of MoO_2 and an additional phase were observed. The diffraction pattern from the additional phase corresponded to that of $K_2Mo_8O_{16}$. $K_2Mo_8O_{16}$ may have formed by the diffusion of K, which is incorporated as an additive in the glass substrate, into the growing film at high temperatures. XPS analysis was performed for the film fabricated at 550 °C to confirm the presence of K. However, along with K and Mo, Si from the glass substrate was also detected by XPS, presumably due to the unevenness of the film and low film thickness at some parts as described later. Therefore, it was impossible to verify whether the detected K was present in the film or substrate using XPS. However, the idea that K present in the glass substrate led to the formation of $K_2Mo_8O_{16}$ was supported by fabricating a film on a quartz substrate which does not contain K; an XRD pattern without the additional phase was obtained for the MoO_2 film formed on the quartz substrate at 550 °C (Figure 2-3b). Therefore, the formation of the additional phase can be prevented by using a quartz substrate. However, at the furnace temperature of 550 °C, the films deposited on both quartz and glass were rough and not as smooth as the ones deposited at 480 °C, a temperature that is low enough to prevent the formation of the additional phase.

The films formed at different positions in the furnace at temperatures of 480 °C and

550 °C (indicated as 480u, 480m, 480d, 550u, 550m, and 550d in Figure 2-2b) were analyzed to examine the differences in the deposited phase according to the substrate position in the furnace. Figures 2-3c and d show the XRD patterns of these films. At the furnace temperature of 480 °C, the single-phase MoO_2 film with the preferred orientation was obtained at every substrate position from upstream to downstream. The peak at 2θ = 37° for 480m is broader than those for 480u and 480d. As mentioned above, the strong diffraction at 2θ = 37° can be attributed to the $(20\bar{2})$, $(21\bar{1})$, (020), or (002) plane, which cause diffractions at slightly different angles. The difference in peak width may suggest that some of these crystal planes are preferentially oriented and the degree of the orientation is different in 480m, 480u, and 480d. The film obtained at the furnace temperature of 550 °C contained MoO_2 and the additional phase at every position.

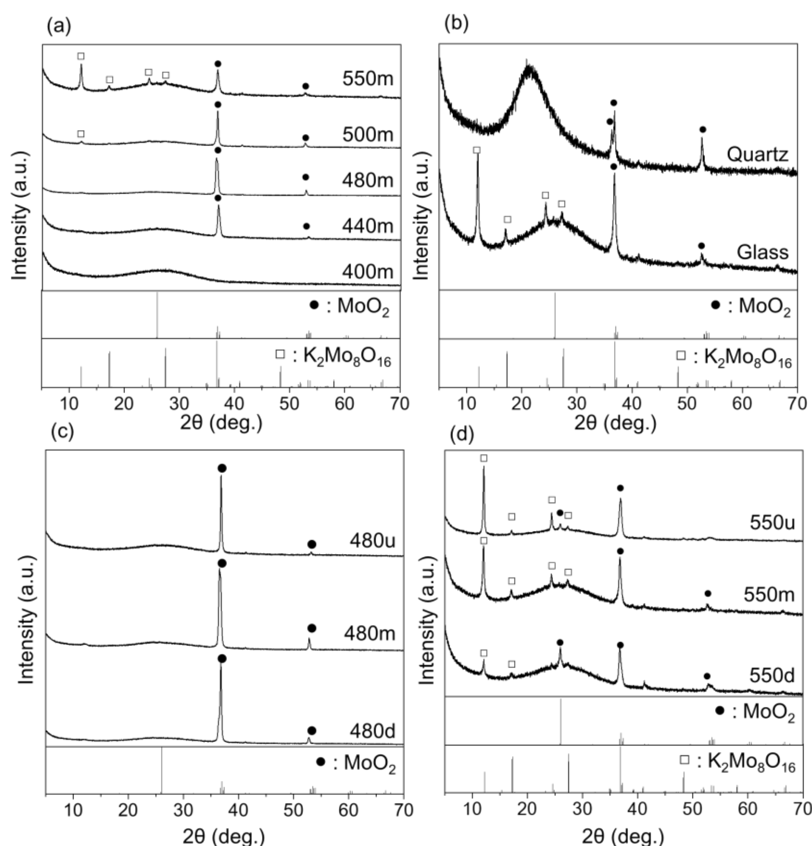

Figure 2-3 XRD patterns of (a) films deposited at a position of 18 cm away from the inlet of the furnace set at different temperatures (400–550 °C), (b) films deposited at 550 °C on the quartz and glass substrates, (c,d) films deposited at various positions in the furnace set at temperatures of 480 °C and 550 °C.

2.3.3 Composition and chemical states of films

The film formed at X = 18 cm in the furnace at 480 °C was further analyzed by XPS. For comparison, the XPS spectra of MoO_2 and MoO_3 powders were also acquired. Figure 2-4a shows the survey scan spectrum in the binding energy range of 0–1000 eV, where only the signals of molybdenum, oxygen, and carbon are observed. The signals of carbon from the film diminished to the noise level after Ar^+ ion etching, indicating that the carbon signal detected before etching originated from hydrocarbon contamination on the film surface and the film is essentially composed only of molybdenum and oxygen.

Figures 2-4b and c show the XPS spectra in the Mo 3d region. In the spectrum acquired before Ar^+ ion etching, Mo (V) is dominant on the surface of the prepared film. Note that Mo (V) is dominant even in MoO_2 powder, while Mo (VI) is mostly detected from MoO_3 powder. The presence of Mo (V) in the MoO_2 powder is due to surface oxidation. It is well known that the surface (thickness: ~ 5 nm) of MoO_2 is easily oxidized to form MoO_{2+x} in air.[8,9] After etching for 5 s, the signal of Mo (IV) was detected more significantly from the film as well as MoO_2 powder. The decrease in the Mo (V) signals can be attributed to the removal of the surface oxidation layer by Ar^+ ion etching as well as the reduction of some molybdenum to Mo (IV) due to Ar^+ ion bombardment [10,11]. Comparison of the spectra of MoO_3 powder before and after etching indicates that Mo (VI) was reduced to Mo (V) by Ar^+ ion bombardment, but hardly to Mo (IV).

The similarity in the spectral features of the film and MoO_2 powder suggests that the film is composed of MoO_2, although there is a possibility that the average valence of Mo could be slightly higher in the film than in MoO_2. The possible reduction of Mo (V) to Mo (IV) by Ar^+ ion bombardment leaves this ambiguity in the analysis.

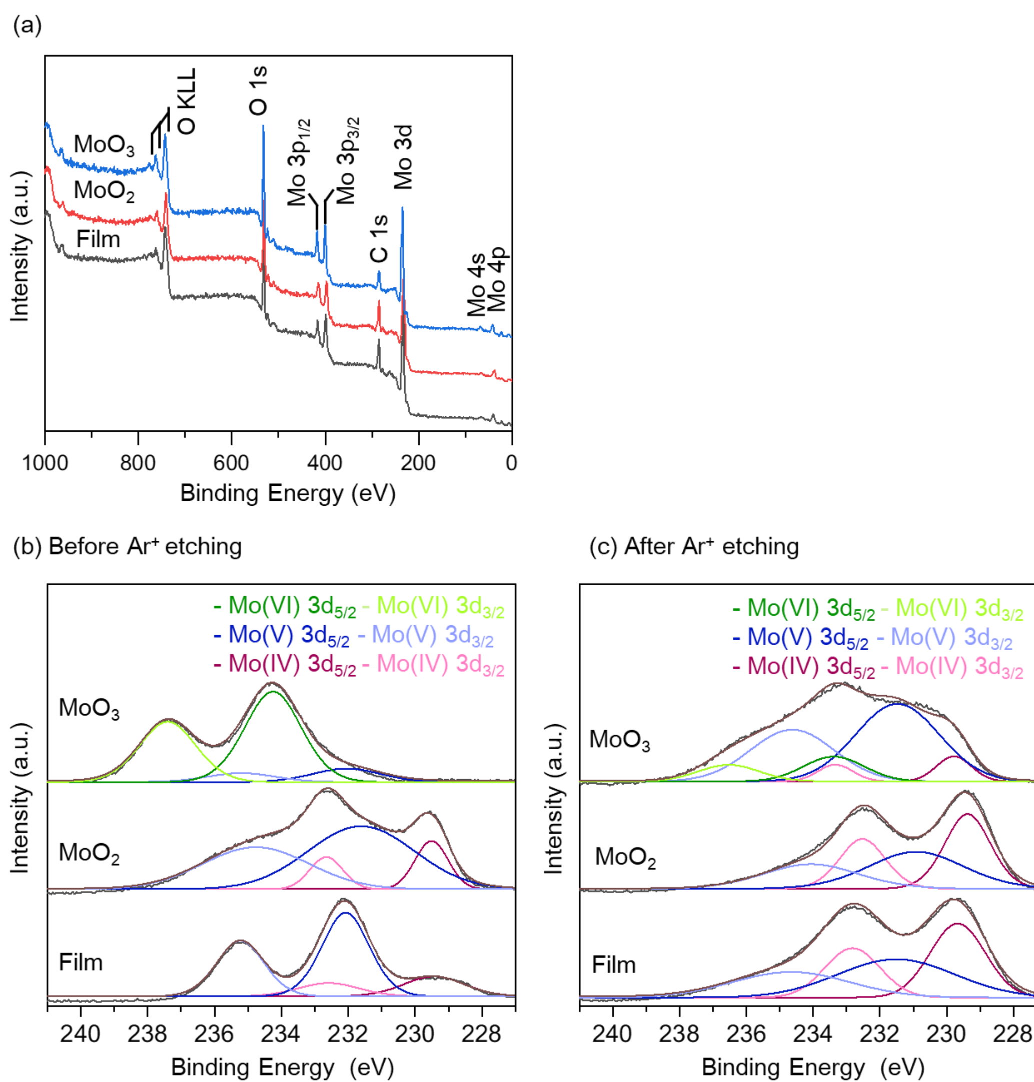

Figure 2-4 (a) Wide-scan XPS spectra and (b, c) Mo 3d spectra of the MoO_2 thin film prepared by mist CVD, MoO_2 powder, and MoO_3 powder before and after Ar^+ ion etching for 5s.

2.3.4 Morphology of films

Figure 2-5 shows the surface and cross-sectional SEM images of the films. Figure 2-5 (a–c) show that the film prepared at the furnace temperature of 550 °C is composed of sparsely deposited crystalline grains along with a rough surface, particularly at the upstream and midstream areas. Figure 2-5 (b, d–f) show that the films prepared at lower furnace temperatures are composed of fine crystalline grains that densely cover the substrate surface. The films prepared at the furnace temperatures of 480 °C and 440 °C are especially smooth and dense. Atomic force microscopy images of the films also confirmed the smoothness of the film deposited at 480 °C (Figure 2-6). The root mean square roughness of the films deposited at 480 and 550 °C are 13 nm and 83 nm, respectively. The cross-sectional SEM images suggest that at 550 °C, new crystalline grains were generated constantly during the film growth, whereas at temperatures of 480 °C and 440 °C, the growth occurred after the nucleation of grains on the substrate. At the furnace temperatures of 480 °C and 440 °C, the MoO_2 films were densely deposited and the entire film surface was smooth. This result demonstrates that smooth and dense MoO_2 films can be obtained over a wide area by mist CVD.

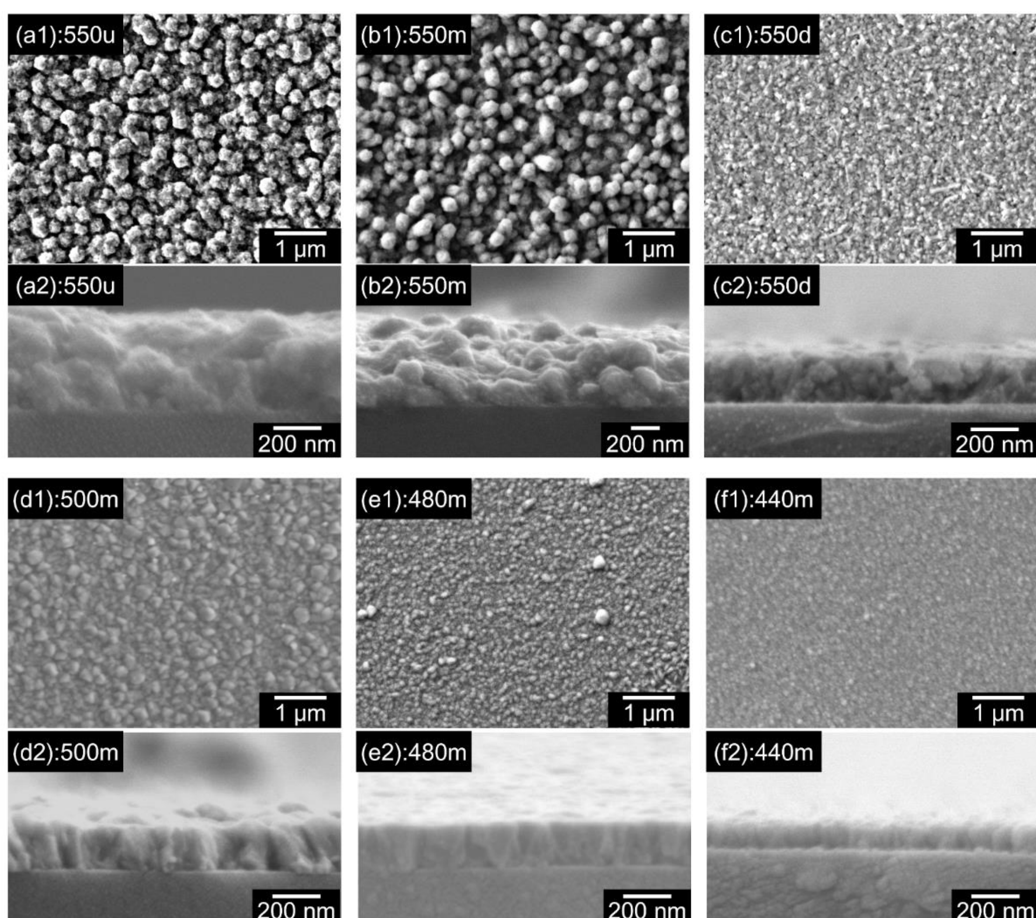

Figure 2-5 Surface and cross-sectional SEM images of (a, b, c) films obtained at upper, middle, and downstream areas in the furnace at 550 °C, and (d, e, f) films obtained at the middle stream area in the furnace at 500, 480, and 440 °C.

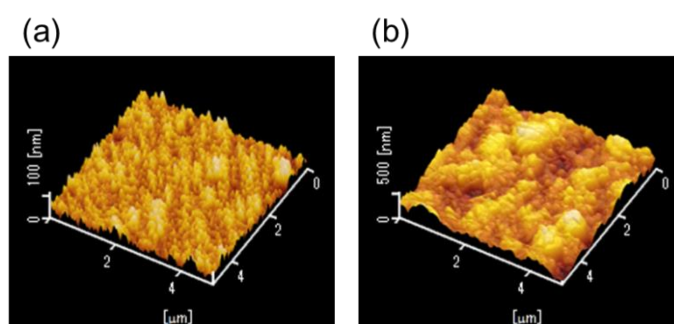

Figure 2-6 Atomic force microscopy images of the films deposited at a position of 18 cm away from the inlet of a furnace set at (a) 480 and (b) 550 °C.

Figure 2-7 shows the distribution of the film thickness determined from the cross-sectional SEM images. At the furnace temperatures of 500 °C and 480 °C, the film thickness was ~200 nm evenly at the position of ~15–23 cm from the furnace inlet. The films prepared at a lower furnace temperature (440 °C) were relatively thinner, and the film was not uniform in any region. The film prepared at a higher temperature of 550 °C was significantly thicker, but contained no uniform region.

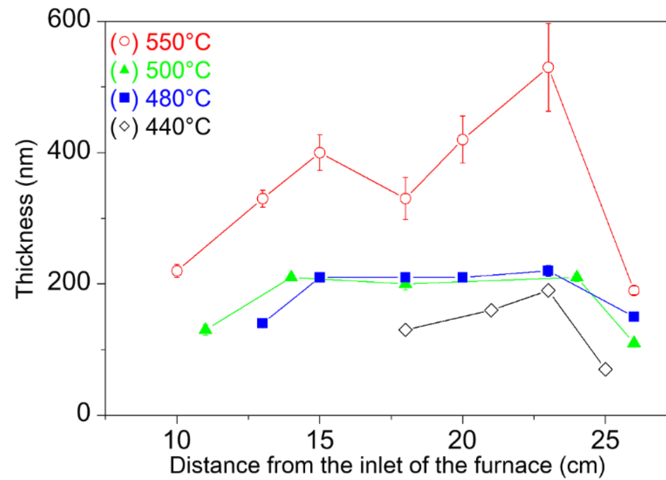

Figure 2-7 Distribution of the thickness of films prepared at different furnace temperatures.

2.3.5 Electrical resistivity

Figure 2-8 shows the electrical resistivity of the films. The films prepared at the furnace temperatures of 440–500 °C showed a low resistivity of the order of 10^{-3} Ω·cm throughout the film. This value of resistivity obtained is one order of magnitude higher than that of the MoO_2 film prepared by vacuum processes [12,13] (10^{-4} Ω·cm), but one order of magnitude smaller than that of the MoO_2 prepared by a solution process [14] (10^{-2} Ω·cm). The film prepared at 550 °C showed a relatively high resistivity of 10^{-2} Ω·cm which can be attributed to the additional phase included in the film and the less dense morphology of the film.

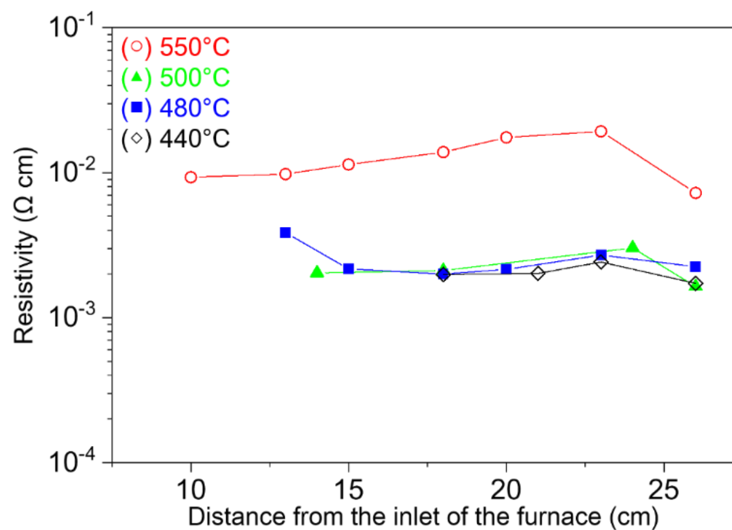

Figure 2-8 Electrical resistivity of the MoO_2 film as a function of the distance from the inlet of the furnace at different preset temperatures.

2.3.6 Discussion

In general, a CVD process includes the following four steps: (1) transport of precursors, (2) diffusion and adsorption of precursors to the substrate, (3) progress of the chemical reaction on the substrate surface, and (4) removal of byproducts. The rate-limiting step depends on the temperature; it tends to be the chemical reaction on the substrate surface (step 3) at low temperatures and the diffusion/adsorption of precursors to the substrate (step 2) at high temperatures. When the temperature is increased further, solid particles are precipitated in the gas phase during the transportation (step 1) before the precursors reach the substrate.

In the present study, the thickness of the film deposited at the furnace temperature of 550 °C was significantly greater than that of the films obtained at lower temperatures. As discussed previously, the SEM images of the film (Figure 2-5) revealed that new crystal grains were generated during the film deposition at 550 °C. This result suggests that solid particles were precipitated in the gas phase during the transport of the mist and the precipitates settled on the growing film. In other words, at 550 °C, the precipitation of MoO_2 powder occurred concomitant with the crystal growth on the substrate by the chemical reaction of the precursor. At lower furnace temperatures of 500 °C and 480 °C, a uniformly thick film was formed over a wide area (Figure 2-7), although the substrate temperature varied depending on the position of the substrate. Furthermore, as shown in Figure 2-5, all the crystal grains appeared to have grown on the substrate at these temperatures. Therefore, the diffusion and adsorption of the precursor from the gas phase to the substrate (step 2) appears to be the rate-limiting step at these temperatures. At 440 °C, the film thickness varied depending on the substrate temperature, indicating that the chemical reaction on the surface is the rate-limiting step at this temperature.

2.4 Conclusion

Dense and smooth MoO_2 films were obtained by mist CVD using acetylacetonate salt as the precursor. The MoO_2 films were deposited at furnace temperatures of ≥440 °C; however, an additional phase was obtained for the MoO_2 films deposited at the furnace temperature of 550 °C. Despite the uneven distribution over the substrate surface, a smooth MoO_2 film with a constant thickness of 200 nm was uniformly deposited over a wide area of the substrates at furnace temperatures in the range 480–500 °C. The prepared MoO_2 films showed a low resistivity of 2×10^{-3} Ω·cm.

References

[1] S. Ashraf, C.S. Blackman, G. Hyett, I.P. Parkin, Aerosol assisted chemical vapour deposition of MoO_3 and MoO_2 thin films on glass from molybdenum polyoxometallate precursors; thermophoresis and gas phase nanoparticle formation, J. Mater. Chem. 16 (2006) 3575. https://doi.org/10.1039/b607335b.

[2] D. Shinohara, S. Fujita, Heteroepitaxy of corundum-structured α-Ga_2O_3 thin films on α-Al_2O_3 substrates by ultrasonic mist chemical vapor deposition, Jpn. J. Appl. Phys. 47 (2008) 7311–7313. https://doi.org/10.1143/JJAP.47.7311.

[3] T. Ikenoue, J. Inoue, M. Miyake, T. Hirato, Epitaxial growth of undoped and Li-doped NiO thin films on α-Al_2O_3 substrates by mist chemical vapor deposition, J. Cryst. Growth. 507 (2019) 379–383. https://doi.org/10.1016/j.jcrysgro.2018.11.032.

[4] T. Ikenoue, S. Sakamoto, Y. Inui, Fabrication and characteristics of p-type Cu_2O thin films by ultrasonic spray-assisted mist CVD method, Jpn. J. Appl. Phys. 53 (2014) 05FF06. https://doi.org/10.7567/JJAP.53.05FF06.

[5] K. Tadanaga, A. Yamaguchi, A. Sakuda, A. Hayashi, M. Tatsumisago, A. Duran, M. Aparacio, Preparation of $LiMn_2O_4$ cathode thin films for thin film lithium secondary batteries by a mist CVD process, Mater. Res. Bull. 53 (2014) 196–198. https://doi.org/10.1016/j.materresbull.2014.01.032.

[6] J.-G. Choi, L.T. Thompson, XPS study of as-prepared and reduced molybdenum oxides, Appl. Surf. Sci. 93 (1996) 143–149. https://doi.org/10.1016/0169-4332(95)00317-7.

[7] A. Bolzan, B. Kennedy, C. Howard, Neutron powder diffraction study of molybdenum and tungsten dioxides, Aust. J. Chem. 48 (1995) 1473. https://doi.org/10.1071/CH9951473.

[8] E. Ahn, T. Min, J. Lee, I. Lee, Y. Kim, H. Jeen, Role of surface oxidation for thickness-driven insulator-to-metal transition in epitaxial MoO_2 films, Appl. Surf. Sci. 459 (2018) 92–97. https://doi.org/10.1016/j.apsusc.2018.07.188.

[9] H.-S. Kim, J.B. Cook, S.H. Tolbert, B. Dunn, The development of pseudocapacitive properties in nanosized-MoO_2, J. Electrochem. Soc. 162 (2015) A5083–A5090. https://doi.org/10.1149/2.0141505jes.

[10] N. V. Alov, XPS study of MoO_3 and WO_3 oxide surface modification by low-energy Ar^+ ion bombardment, Phys. Status Solidi. 12 (2015) 263–266. https://doi.org/10.1002/pssc.201400108.

[11] R. Holm, S. Storp, ESCA studies on changes in surface composition under ion bombardment, Appl. Phys. 12 (1977) 101–112. https://doi.org/10.1007/BF00900076.

[12] W. Lee, C.J. Cho, W.C. Lee, C.S. Hwang, R.P.H. Chang, S.K. Kim, MoO_2 as a thermally stable oxide electrode for dynamic random-access memory capacitors, J. Mater. Chem. C. 6

(2018) 13250–13256. https://doi.org/10.1039/C8TC04167A.

[13] V. Bhosle, A. Tiwari, J. Narayan, Epitaxial growth and properties of $MoO_x$$(2<x<2.75)$ films, J. Appl. Phys. 97 (2005) 083539. https://doi.org/10.1063/1.1868852.

[14] Y. Shi, B. Guo, S.A. Corr, Q. Shi, Y.-S. Hu, K.R. Heier, L. Chen, R. Seshadri, G.D. Stucky, Ordered mesoporous metallic MoO_2 materials with highly reversible lithium storage capacity, Nano Lett. 9 (2009) 4215–4220. https://doi.org/10.1021/nl902423a.

Chapter 3
Mist CVD of Vanadium Dioxide Thin Films with Excellent Thermochromic Properties Using a Water-Based Precursor Solution

3.1 Introduction

In this chapter, the author reports the fabrication of VO_2 thin films by the mist CVD method and the thermochromic properties of the resulting films. As described in Chapter 1, VO_2 exhibits MIT at approximately room temperature (~68 °C). Both visible and infrared light are transmitted through VO_2 below the phase transition temperature (T_c); however, above T_c, only visible light is transmitted [1,2]. Owing to this property of VO_2, windows coated with VO_2 block infrared light from entering when it is hot outside, while still allowing the transmission of visible light. Infrared radiation, which accounts for approximately 50% of the solar radiation energy, is the heat source that flows into buildings. Therefore, the control of the heat intake through VO_2-based smart windows can effectively reduce the amount of energy consumed for air conditioning in a building.

Mist CVD can fabricate films at low energy consumption, and thus VO_2 thin films are expected to be fabricated by this method. However, to date, no VO_2 thin films with sufficient performance have been obtained via mist CVD. The visible transmittance reported for VO_2 films fabricated through mist CVD is generally <40% at a wavelength of 550 nm, and the change in the infrared transmittance at a wavelength of 2500 nm below and above T_c is also as small as <30 percentage point (pp) [3–8]. For other oxide films, such as Ga_2O_3 and ZnO, high-quality films comparable to those obtained by vacuum processes are produced through mist CVD [9,10]. Therefore, it is expected that high-quality VO_2 films can also be obtained through mist CVD by exploring the deposition conditions in further detail.

The optical properties of VO_2 are strongly affected by its stoichiometry. Contaminating a VO_2 crystal with V^{3+} and V^{5+} deteriorates its visible transmittance and

infrared transmittance change [11–13]. Although films composed of a VO_2 single phase were reportedly obtained through mist CVD using an ethanol solution of vanadyl acetylacetonate ($VO(acac)_2$) as the precursor [5], further control of the stoichiometry of the VO_2 film is necessary to enhance its properties.

In mist CVD, metal salt and the solvent of the precursor solution are the factors that can significantly affect the crystal phase and physical properties of the resulting film, because the latter can change the oxygen potential of the deposition atmosphere [5,14,15]. A study on the oxidation of V_2O_3 to VO_2 reported that a water vapor atmosphere is suitable for stabilizing vanadium in the tetravalent state [16,17]. Although it was reported that mist CVD using a precursor solution composed of vanadium(III) acetylacetonate ($V(acac)_3$) and water resulted in V_2O_3 [5], mist CVD using a combination of tetravalent vanadium salt and water has not yet been investigated.

In this chapter, the author reports fabrication of vanadium oxide by mist CVD using a methanol solution and a water solution of $VO(acac)_2$ to investigate the effect of the solvent on the crystal phase of the resulting film. Furthermore, the author demonstrates that VO_2 films with high visible transmittance and a large infrared transmittance change by MIT are obtained through mist CVD using a water-based precursor solution.

3.2 Experimental

3.2.1 Materials

The precursor solutions were prepared by dissolving bis(acetylacetonato) vanadium oxide ($VO(acac)_2$; 98%, STREM) in distilled water or methanol at a concentration of 0.010 mol L^{-1}. A quartz plate (25 mm × 25 mm; thickness = 0.7 mm) was used as the substrate for mist CVD. Before use, the quartz substrate was washed sequentially in acetone, distilled water and isopropanol in an ultrasonic cleaner and dried by blowing air.

3.2.2 Mist CVD of VO_2

The apparatus and deposition procedure of mist CVD used for the deposition of VO_2 were the same as those described in Chapter 2, except for the method of placing the substrate. Herein, the substrate was placed on a holder installed at the center of the tube furnace. The precursor mist was supplied to the substrate through N_2 flow for 10 min and 20 min in the cases of using a methanol solution and water solution, respectively. The durations for the film growth were determined by considering the difference in the amount of mist generated from two different solvents. The flow rate of the carrier gas and dilution gas was 3.0 L min^{-1}. After the mist supply was turned off, the substrate was cooled to <100 °C in a furnace under N_2 gas flow.

3.2.3 Characterization of films

XRD and XPS measurements and SEM and AFM observation were carried out with the same instruments as those described in Chapter 2. In the XRD measurements, the incident angle of X-ray was fixed at $\omega = 1.5°$. In XPS measurements, according to a report [18], the O1s signal taken at 530 eV was used as the binding energy reference. A pass energy of 50 eV with 1 eV step was used for collecting the wide-scan survey spectrum, while a pass energy of 30 eV with 0.2 step and 20 eV with 0.05 eV step, respectively, was

used for collecting the C1s spectrum and V2p and O1s spectrum. Sputter etching of the obtained samples was carried out using an argon ion gun operated at 400 V for 60s with a duty ratio of 50%. Under the acceleration voltage of 400 V, a standard SiO_2 film is etched at the rate of approximately 0.3 nm s^{-1}. The XPS spectra were analyzed using SPECSURF (version 2.0.5.7, JEOL) software. Based on a previous report [18], the deconvolution of the V2p and O1s spectrum was performed using mixed Lorentzian-Gaussian function on the assumption that the $V2p_{3/2}$ and $V2p_{1/2}$ signals intensities have a 2:1 ratio. A Shirley function was used to subtract the background of the spectra.

The electrical resistivity was measured by a four-probe method using a source meter (2450 SourceMeter, KEITHLEY) while changing the temperature of the films using a hot plate. The temperature of the film was measured using a thermocouple attached to the film. The logarithmic derivatives of the temperature dependence of resistivity ($d(\log R)/dT$) were extracted to evaluate the phase transition temperature (T_c) and width of the hysteresis loop (ΔH). Further, T_c and ΔH were defined using the temperature corresponding to the maximum of $d(\log R)/dT$ in heating and cooling cycles (defined as $T_{heating}$ and $T_{cooling}$, respectively) as follows.

$$T_c = \frac{T_{heating}+T_{cooling}}{2} \dots (1)$$

$$\Delta H = T_{heating} - T_{cooling} \dots (2)$$

For an obtained VO_2 films, the temperature dependence of the resistivity was also measured by the van der Pauw method with a Hall effect measurement system (ResiTest8300, Toyo Technica) to validate the accuracy of the measurement. The difference in the values of log (R) obtained by the two methods at the same temperature was typically less than 0.2. The transmittance spectra of the films were measured using a UV-Vis-NIR spectrophotometer (SolidSpec-3700DUV, Shimadzu) at room temperature (~26 °C) and 100 °C using a heating stage (Mettler FP82 hotstage). The measurement error of the transmittance, which was mainly caused by baseline variation, was less than a few percent. The visible transmittance ($T_{lum}(\theta)$, 390–760 nm) and solar spectrum transmittance ($T_{sol}(\theta)$, 280–2500 nm) at a measurement temperature of θ were calculated using the following equations:

$$T_{\mathrm{lum}}(\theta) = \frac{\int \varphi_{\mathrm{lum}}(\lambda) T(\lambda,\theta) \mathrm{d}\lambda}{\int \varphi_{\mathrm{lum}}(\lambda) \mathrm{d}\lambda} \quad \ldots (3)$$

$$T_{\mathrm{sol}}(\theta) = \frac{\int \varphi_{\mathrm{sol}}(\lambda) T(\lambda,\theta) \mathrm{d}\lambda}{\int \varphi_{\mathrm{sol}}(\lambda) \mathrm{d}\lambda} \quad \ldots (4)$$

where $T(\lambda,\theta)$ is transmittance at wavelength λ and measurement temperature θ, $\varphi_{\mathrm{lum}}(\lambda)$ is the standard luminous efficiency function for the photopic vision of human eyes, $\varphi_{\mathrm{sol}}(\lambda)$ is the solar irradiance spectrum for an air mass of 1.5 (corresponding to the sun standing 37° above the horizon). T_{lum} and ΔT_{sol} values of the obtained films were calculated using the following equations:

$$T_{\mathrm{lum}} = \frac{T_{\mathrm{lum}\,(26\,°\mathrm{C})} + T_{\mathrm{lum}(100\,°\mathrm{C})}}{2} \quad \ldots (5)$$

$$\Delta T_{\mathrm{sol}} = T_{\mathrm{sol}(26\,°\mathrm{C})} - T_{\mathrm{sol}(100\,°\mathrm{C})} \quad \ldots (6)$$

3.3 Results and Discussion

3.3.1 Appearance and phase of the films

Mist CVD was performed using a methanol or water solution of $VO(acac)_2$ to examine the effect of the solvent of the precursor solution on the resulting film. Figures 3-1a and b show the appearance of the films deposited at 400–750 °C from methanol and water solutions, respectively. The colors of the samples show that the films were formed from methanol and water solutions at temperatures above 450 and 400 °C, respectively. The films deposited from methanol solution were gray or black, while the films deposited from water solution were brown, which is the color of monoclinic VO_2 reported in the literature [19,20].

Figure 3-1c shows the XRD patterns of the samples before and after the deposition using methanol solution. After the deposition at 400 °C, the sample showed only a halo from the quartz substrate, confirming the absence of film formation at 400 °C. In addition to the halo from the substrate, the films deposited from methanol solution at 450–650 °C showed XRD patterns corresponding to that of V_2O_3 (JCPDS 074-2037). The XRD pattern of the film deposited at 750 °C did not match any reference pattern, which indicates that an unidentified crystalline phase was formed at this temperature. Figure 3-1d shows the XRD patterns of the films deposited from water solution. The sample after the deposition at 400 °C showed no diffraction peaks from the film (Figure 3-1d), although the formation of the film was visually confirmed (Figure 3-1b), thereby suggesting that the film was amorphous. The film deposited at 450 °C exhibited only a small peak at 2θ = 11°; thus, the phase of the film could not be identified. The films deposited at 550 and 650 °C exhibited the XRD patterns of VO_2 (JCPDS 072-0514), in addition to a halo from the substrates. Further, the films showed no additional peaks, thereby indicating that the films were composed of a single phase of VO_2. The film deposited at 750 °C showed no XRD peaks. However, the extension of the deposition time from 20 to 60 min resulted in the formation of a film with the XRD patterns of VO_2 (Figure 3-2). This indicates that the deposition time of 20 min was significantly short to form a VO_2 film that is sufficiently thick for producing a detectable XRD pattern. In

general, when mist CVD is performed at low temperatures, amorphous or unintended phases are formed because the decomposition of the precursor and the crystallization of the deposited material do not proceed sufficiently. At excessively high temperatures, the deposition rate tends to decrease owing to the increase in the re-evaporation rate of the adsorbed precursor atoms on the substrates [21–24]. The aforementioned results are consistent with these general trends and indicate that the optimal temperature for the formation of VO_2 film through mist CVD using a water solution was 550–650 °C. The reproducibility of the formation of single-phase VO_2 films was confirmed by performing the deposition under the same growth conditions several times. While VO_2 was obtained from water solution, V_2O_3 was obtained from methanol solution at 550–650 °C. The vanadium precursor employed for the film deposition was $VO(acac)_2$, which consists of V^{4+}. The XRD results indicated that the vanadium precursor was reduced to V^{3+} by methanol during the deposition process, whereas the oxidation state of the precursor was unchanged during the deposition process using water solution.

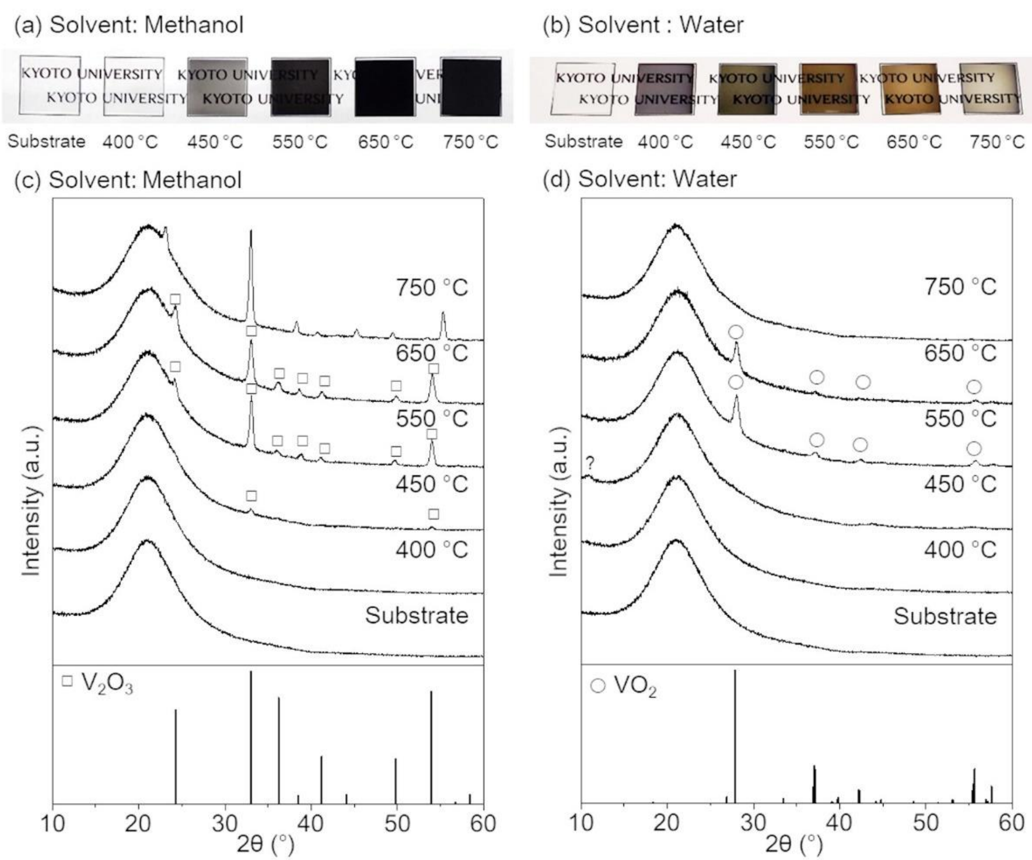

Figure 3-1 (a, b) Photographs and (c, d) XRD patterns of the substrates before and after film deposition at 400–750 °C using (a, c) methanol and (b, d) water solutions of $VO(acac)_2$.

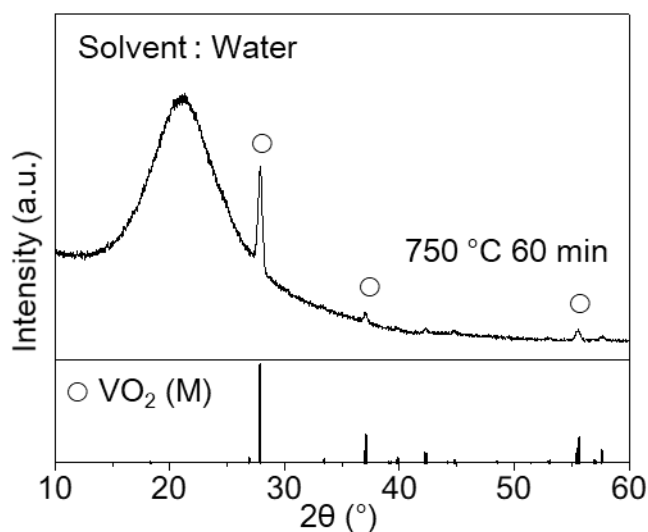

Figure 3-2 XRD pattern of the film deposited at 750 °C for 60 min using water solution of $VO(acac)_2$.

3.3.2 Composition and chemical states of films

XPS measurements were performed on the V_2O_3 and VO_2 films deposited at 650 °C from methanol and water solutions, respectively, to analyze the chemical states of the elements in the films. The survey spectra (Figure 3-3) indicate the presence of V, O and contaminated C in both the films. Figures 3-4a and c show the XPS spectra of the O1s and V2p regions. The spectra were deconvoluted into several peaks assuming the presence of oxygen with two different chemical states and vanadium with valence states ranging from +3 to +5. As shown in Table 3-1, the peak positions for each chemical state resulting from the deconvolution are in agreement with the reported peak positions [18,25–27]. The deconvolution of the V2p peaks indicates the presence of V^{3+}, V^{4+} and V^{5+} in the V_2O_3 film and V^{4+} and V^{5+} in the VO_2 film. The presence of vanadium atoms with higher oxidation numbers (V^{4+} and V^{5+} in V_2O_3, and V^{5+} in VO_2) can be attributed to the surface oxidation of the films exposed to ambient air [18,28]. No V^{3+} signal was observed in the VO_2 film, which indicates that the precursor was not reduced during the deposition process using water solution. This is consistent with the XRD pattern of the film (Figure 3-1d). It should be noted that Ar^+ etching, a well-known technique for removing the surface oxidation layer, is not applicable for identifying the valence state of vanadium oxides because it results in the reduction of vanadium [29].

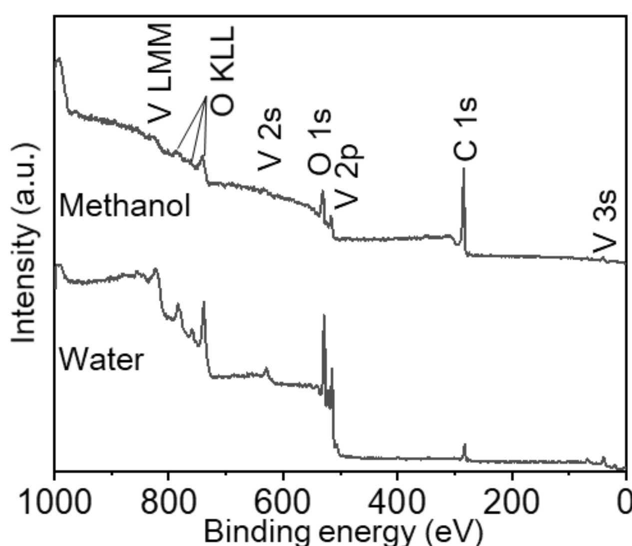

Figure 3-3 Wide-scan XPS spectra of the films deposited at 650 °C from water and methanol solutions.

In the O1s region (Figures 3-4a and c), two peaks corresponding to O in the V–O bond and O in the C–O, C=O and –OH bonds (denoted as O–C, H) were observed in both the V_2O_3 and VO_2 films. In the C1s region (Figures 3-4b and d), two peaks corresponding to C in the C–C and C–O bonds were observed. The O–C, H, C–C and C–O peaks were not observed after Ar^+ ion etching (Figures 3-4b, 3-4d and 3-5); thus, they were assigned to surface contamination. However, another peak emerged at a binding energy slightly lower than that of the C–C bond in the C1s region for the V_2O_3 film after etching (Figure 3-4b). The intensity of this peak remained almost unchanged even after increasing the etching time. The peak position (283.6 eV) was close to that of C1s in V–C [30], and thus the detection of this peak presumably indicates the presence of carbon atoms in the V_2O_3 crystal. In contrast, the VO_2 film exhibited no peaks in the C1s region after Ar^+ ion etching. This indicates that the VO_2 crystal deposited from water solution was not contaminated with carbon, except for the surface contamination layer.

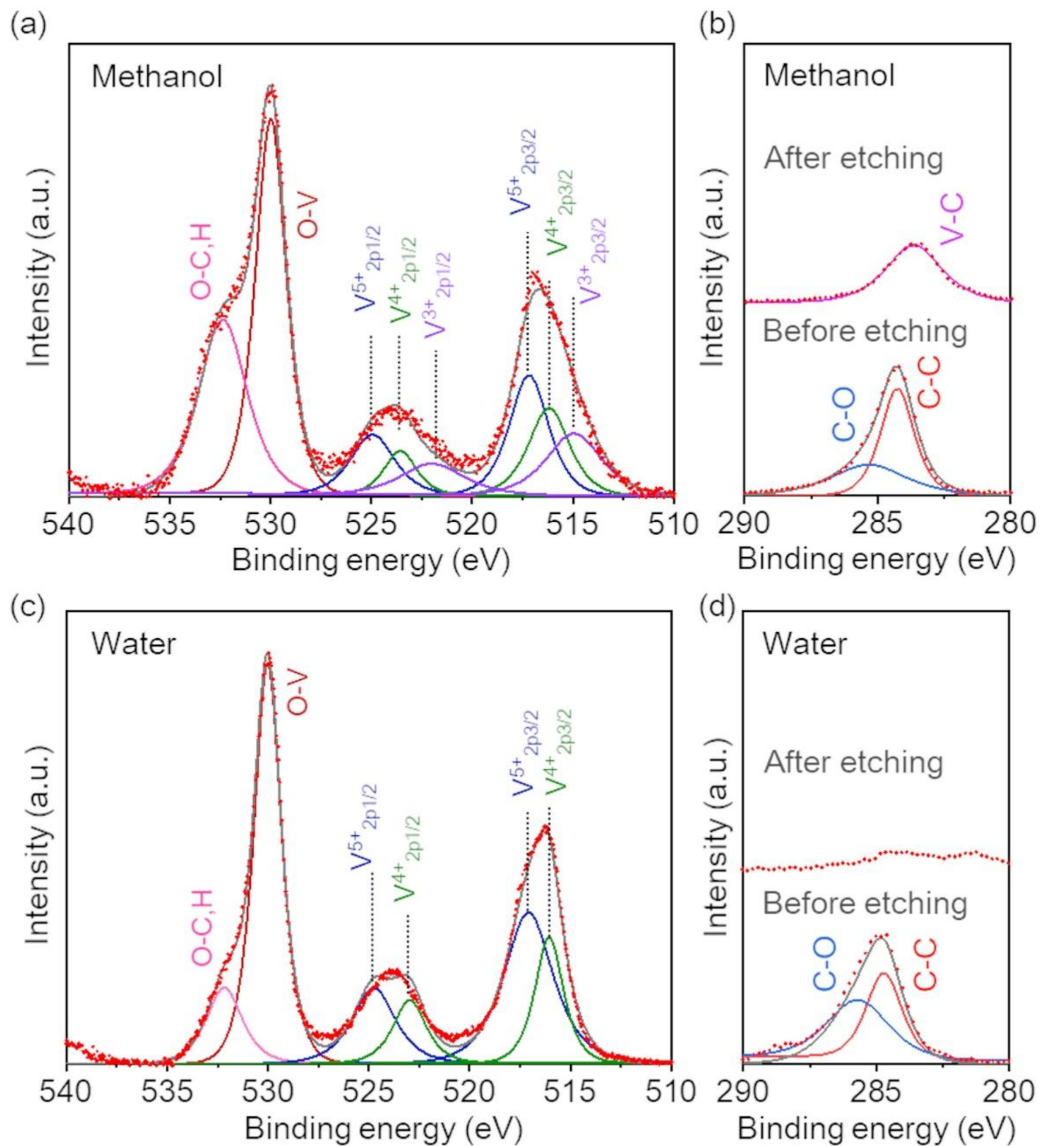

Figure 3-4 (a,c) O1s and V2p spectra of the films deposited at 650 °C from (a) methanol and (c) water solutions. (b,d) Deconvolution of C1s spectra for the films deposited at 650 °C from the (b) methanol and (d) water solutions before and after Ar^{+} ion etching.

Table 3-1 XPS binding energies for the V2p and O1s signals of the films deposited at 650 °C from (a) methanol and (b) water solutions. (c) Values of binding energy for V2p and O1s reported in the literature.

	(a) Methanol	(b) Water	(c) References [18,25–27]
Core line	B.E. (eV)	B.E. (eV)	B.E. (eV)
V^{3+} $2p_{3/2}$	515.0	-	513.3–515.9
V^{4+} $2p_{3/2}$	516.2	516.1	515.5–516.4
V^{5+} $2p_{3/2}$	517.2	517.1	516.8–517.5
V^{3+} $2p_{1/2}$	522.0	-	520.9–522.8
V^{4+} $2p_{1/2}$	523.6	523.0	522.9–524.1
V^{5+} $2p_{1/2}$	524.9	524.8	523.6–524.9
O-V	530.0 (fixed)	530.0 (fixed)	529.8–530.5
O-C, H	532.4	532.2	530.7–533.1

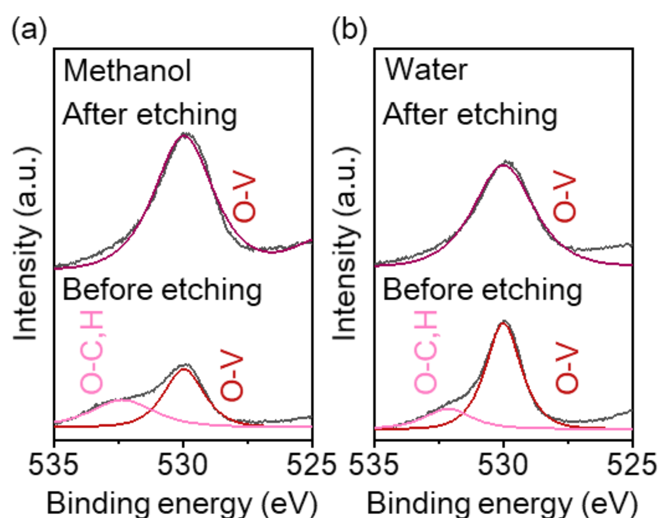

Figure 3-5 O1s spectra of the films deposited at 650 °C from (a) methanol and (b) water solutions before and after Ar^{+} ion etching.

3.3.3 Morphology of films

Figure 3-6 shows the morphology of the VO_2 films deposited at 550 and 650 °C from water solution. The surface SEM images (Figures 3-6a, b, e and f) revealed that both the films were composed of densely deposited crystal grains with a diameter of several tens of nanometers. The thicknesses of the films deposited at 550 and 650 °C were 56 and 49 nm, respectively (Figures 3-6c and g). These are within the thickness range of 40–80 nm, where VO_2 films show a balanced combination of high visible transmittance and infrared switching efficiency [31]. The root-mean-square (RMS) roughness values of the surface of the films were determined to be 19 and 12 nm, respectively, through AFM (Figures 3-6d and h). The film deposited at 650 °C was slightly smoother than that deposited at 550 °C.

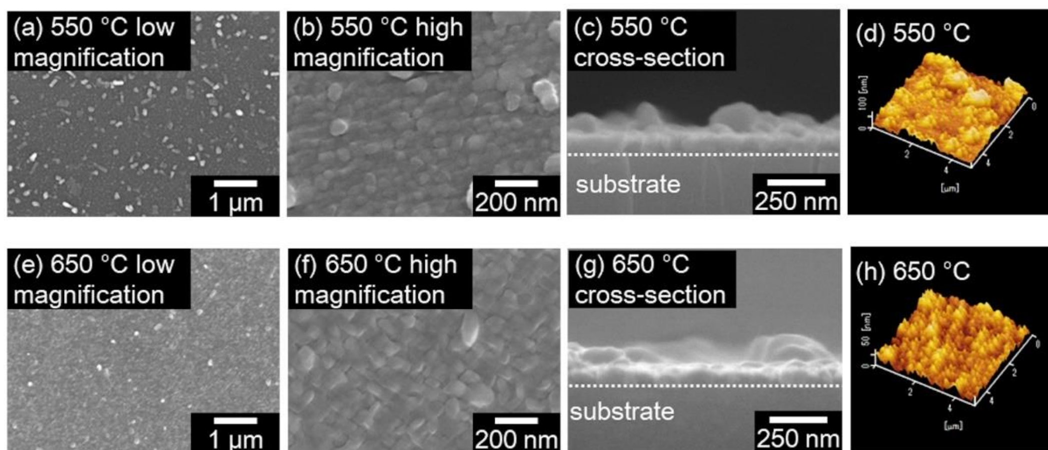

Figure 3-6 Surface and cross-sectional SEM and AFM images of the VO_2 films deposited (a–d) at 550 and (e–h) at 650 °C

3.3.4 Metal–insulator transition behavior

The temperature-dependent resistivities of the obtained films were measured to evaluate their phase transition behaviors. The resistivity of the VO_2 films deposited from water solution at 550 and 650 °C drastically decreased when heated above a certain temperature, and returned to its original value when cooled, thereby showing the typical MIT behavior (Figure 3-7). In contrast, the films showing no XRD peaks of VO_2 (for instance, the film deposited at 450 °C) exhibited no MIT behavior. The resistivity of the V_2O_3 films deposited from methanol solution was nearly constant, independent of temperature, thereby confirming that no MIT occurred within the measured temperature range (Figure 3-8).

The MIT characteristics of the VO_2 films, such as the magnitudes of resistivity change, phase transition temperature (T_c) and width of hysteresis loop (ΔH) determined from the resistivity–temperature curves are summarized in Table 3-2. T_c and ΔH values of the films were calculated from the $d(\log R)/d\theta$ curve (Figure 3-9) using Equations (1) and (2), respectively. The obtained VO_2 films exhibited a resistivity change of more than two orders of magnitude. T_c and ΔH of the films were approximately 70 and 10 °C, respectively. These values are similar to those obtained by vacuum and solution processes [32,33], thus demonstrating that mist CVD is capable of producing VO_2 films with excellent phase transition properties.

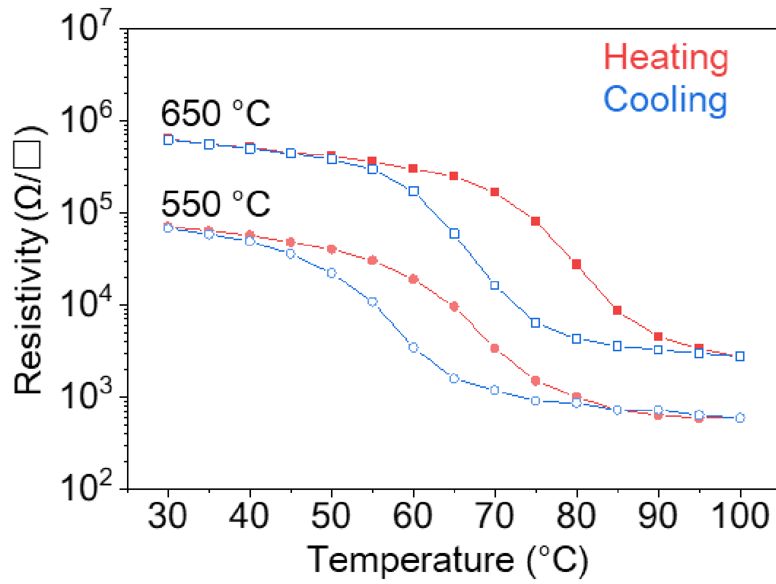

Figure 3-7 Electrical resistance of the films deposited from water solution at 550–650 °C as a function of temperature.

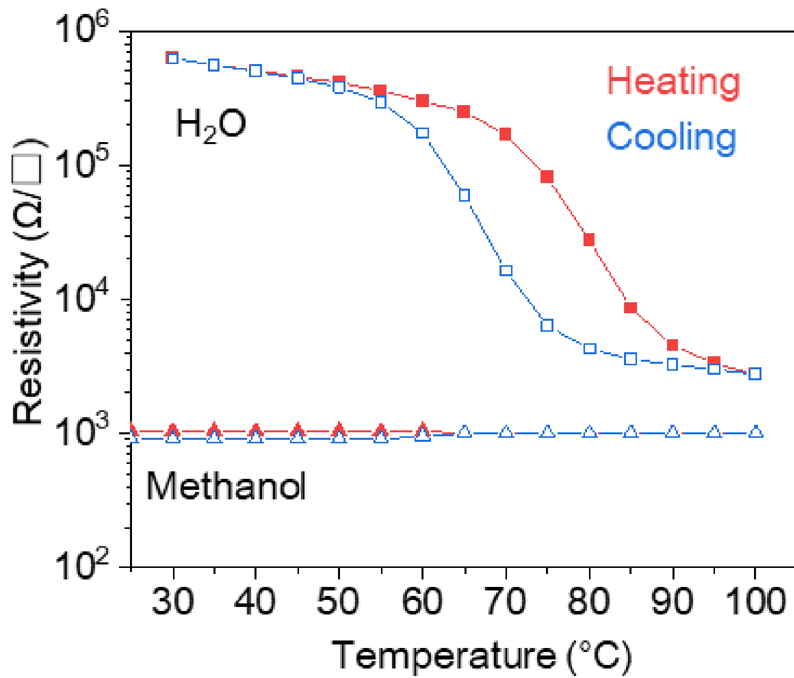

Figure 3-8 Electrical resistance curves as a function of temperature of the films deposited at 650 °C from methanol and water solutions.

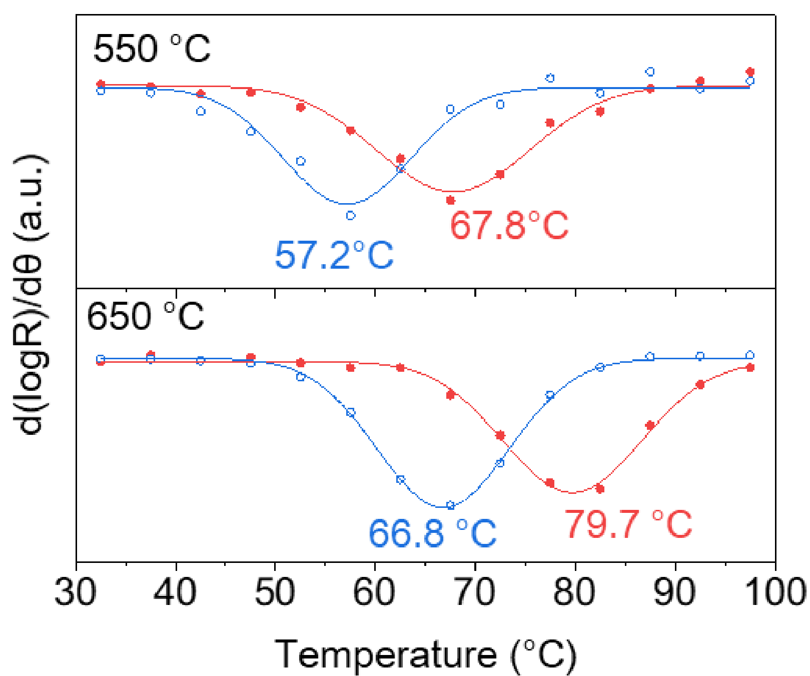

Figure 3-9 The first derivative curve with respect to temperature (θ) of the log of the resistivity (R) used for the determination of the phase transition temperature.

Table 3-2 Resistivity change, transition temperature (T_c) and width of the hysteresis loop (ΔH) of the VO_2 film deposited at 550 and 650 °C using water solution.

Deposition temperature (°C)	$Log(R_{30\ °C}/R_{100\ °C})$	T_c (°C)	ΔH (°C)
550	2.1	63	11
650	2.4	73	13

3.3.5 Optical properties

Figure 3-10 shows the transmittance spectra measured at 26 and 100 °C for the VO_2 film deposited at 650 °C from water solution. The near-infrared (NIR) transmittance of the VO_2 film decreased with an increase in temperature from 26 to 100 °C. The transmittance change was as large as 50 pp at a wavelength of 2500 nm. On the other hand, the visible transmittance was nearly constant or increased with the increasing temperature. The temperature-dependent salient change in the NIR transmittance is the typical MIT behavior of VO_2.

From the transmittance spectra, T_{lum} and ΔT_{sol} of the film were determined to be 48.1% and 5.2 pp, respectively. Gao et al. [34] reported that T_{lum} and ΔT_{sol} of VO_2 films are in the range of 10%–50% and 1–10 pp, respectively. The VO_2 film obtained in this study showed a high T_{lum} of 48.1% and a moderate ΔT_{sol} of 5.2 pp, as compared to the reported values.

Although T_{lum} and ΔT_{sol} are often used as performance indicators for smart windows, not all studies on VO_2 films have reported these values. In particular, the values for VO_2 films grown by mist CVD in previous studies are unavailable in most cases. Therefore, instead of T_{lum} and ΔT_{sol}, the transmittance at a wavelength of 550 nm ($T_{550\,nm}$) and the transmittance change at a wavelength of 2500 nm between the low and high temperatures ($\Delta T_{2500\,nm}$) [35–38] were used to compare the performance of the VO_2 films obtained in this study with those prepared through other processes. High $T_{550\,nm}$ and $\Delta T_{2500\,nm}$ are desirable for smart windows, as the former can save lighting, while the latter can effectively control heat flow [39].

Figure 3-11 shows the values of $T_{550\,nm}$ and $\Delta T_{2500\,nm}$ for the non-doped VO_2 single-layer films prepared through various processes. $T_{550\,nm}$ and $\Delta T_{2500\,nm}$ of the VO_2 film obtained in this study were 47.8% and 57.6 pp, respectively. Compared to the values for previously reported mist-CVD-grown VO_2 films, $T_{550\,nm}$ of the film obtained in this study was nearly the highest and its $\Delta T_{2500\,nm}$ was significantly higher.

Some VO_2 films prepared by other processes have higher values of either $T_{550\,nm}$ or $\Delta T_{2500\,nm}$ than the VO_2 film obtained in this study; however, the author did not find any studies reporting higher values of both the parameters. As many studies have pointed out,

$T_{550\ nm}$ and $\Delta T_{2500\ nm}$ show a trade-off relationship [34], assuming the same quality of VO_2. For example, depending on the thickness of VO_2, one of these values will increase at the expense of the other. Therefore, among the reported VO_2 films, those with the data points ($T_{550\ nm}$, $\Delta T_{2500\ nm}$) located within the zone connecting the highest $\Delta T_{2500\ nm}$ and $T_{550\ nm}$ (the blue region) in Figure 3-11 can be considered to be of similar high quality. The VO_2 film obtained in this study was located within this zone, thereby exhibiting excellent smart window properties comparable to those of high-quality VO_2 films fabricated by other methods.

The enhancement in the quality of the mist-CVD-grown VO_2 films can be attributed to the use of water as the solvent of the precursor solution; previous films were formed from ethanol-based precursor solutions. According to previous studies, water vapor atmosphere is suitable for stabilizing vanadium in the tetravalent state [16,17]. It is known that the performance of smart windows decreases when V^{3+} and V^{5+} contaminate VO_2 [11–13]. The excellent thermochromic properties of the VO_2 film obtained in this study can be attributed to the suppression of V^{3+} and V^{5+} contamination during the deposition by the water solution used in the mist CVD process. Note that, although V^{5+} was detected in the VO_2 film by XPS (Figure 3-4a and c), it does not indicate the presence of V^{5+} in the bulk of the film because XPS only detects the surface elements.

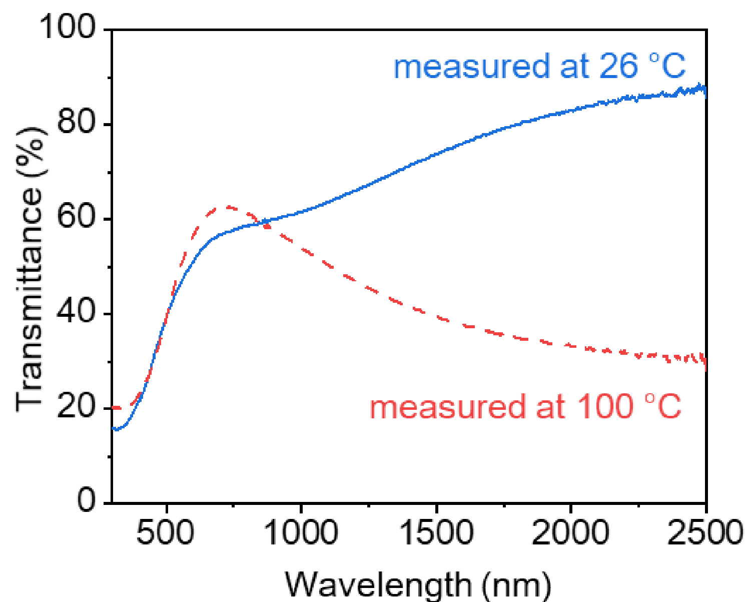

Figure 3-10 Transmittance spectra measured at 26 and 100 °C for the VO_2 films deposited at 650 °C

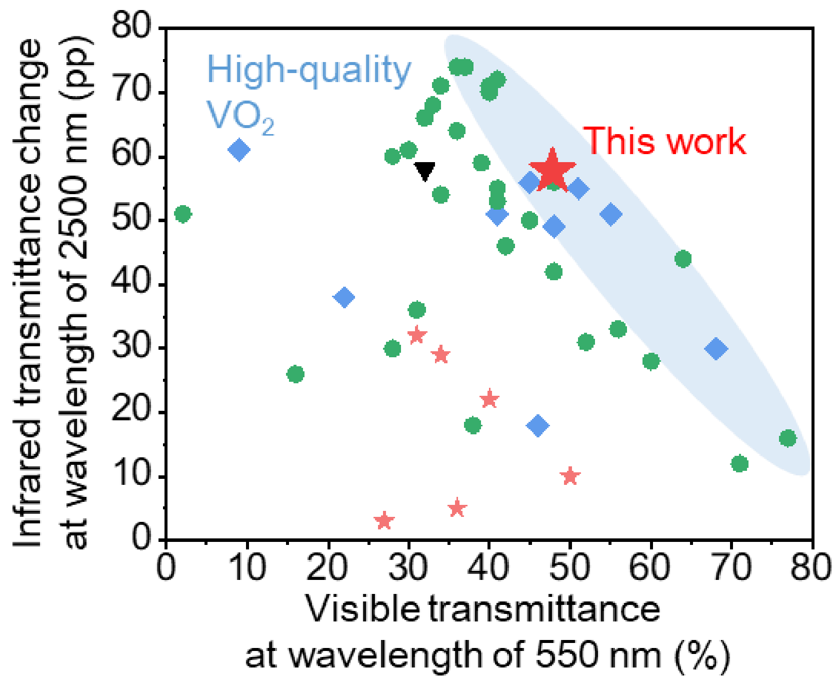

Figure 3-11 Visible transmittance at a wavelength of 550 nm ($T_{550\ nm}$) and infrared transmittance difference at a wavelength of 2500 nm between low (26 °C) and high temperature states (100 °C) ($\Delta T_{2500\ nm}$) of VO_2 fabricated through vacuum processes (●) [35,40–59], atmospheric pressure process (▼) [60], solution processes (◆) [31,38,61–65] and the mist CVD method (★) [3–8].

3.4 Conclusion

High-quality VO_2 films were fabricated through a mist CVD method, which can deposit films at low cost and with high productivity. VO_2 and V_2O_3 films were obtained using water-based and methanol-based precursor solutions, respectively. The obtained VO_2 film showed a high visible transmittance and a large infrared transmittance change compared to those of previously reported mist-CVD-grown VO_2 films. These values are similar to those of high-quality VO_2 deposited by solution and vacuum processes, demonstrating that mist CVD is a promising method for the fabrication of VO_2-based smart windows.

References

[1] F. Béteille, J. Livage, Optical Switching in VO_2 Thin Films, J. Sol-Gel Sci. Technol. 13 (1998) 915–921. https://doi.org/10.1023/A:1008679408509.

[2] A.S. Barker, H.W. Verleur, H.J. Guggenheim, Infrared optical properties of vanadium dioxide above and below the transition temperature, Phys. Rev. Lett. 17 (1966) 1286–1289. https://doi.org/10.1103/PhysRevLett.17.1286.

[3] C. Piccirillo, R. Binions, I.P. Parkin, Nb-Doped VO_2 Thin Films Prepared by Aerosol-Assisted Chemical Vapour Deposition, Eur. J. Inorg. Chem. 2007 (2007) 4050–4055. https://doi.org/10.1002/ejic.200700284.

[4] C. Piccirillo, R. Binions, I.P. Parkin, Synthesis and characterisation of W-doped VO_2 by Aerosol Assisted Chemical Vapour Deposition, Thin Solid Films. 516 (2008) 1992–1997. https://doi.org/10.1016/j.tsf.2007.06.009.

[5] C. Piccirillo, R. Binions, I.P. Parkin, Synthesis and functional properties of vanadium oxides: V_2O_3, VO_2, and V_2O_5 deposited on glass by aerosol-assisted CVD, Chem. Vap. Depos. 13 (2007) 145–151. https://doi.org/10.1002/cvde.200606540.

[6] P. Kiri, M.E.A. Warwick, I. Ridley, R. Binions, Fluorine doped vanadium dioxide thin films for smart windows, Thin Solid Films. 520 (2011) 1363–1366. https://doi.org/10.1016/j.tsf.2011.01.401.

[7] M.E.A. Warwick, R. Binions, Thermochromic vanadium dioxide thin films from electric field assisted aerosol assisted chemical vapour deposition, Sol. Energy Mater. Sol. Cells. 143 (2015) 592–600. https://doi.org/10.1016/j.solmat.2015.01.025.

[8] I. Top, R. Binions, M.E.A. Warwick, C.W. Dunnill, M. Holdynski, I. Abrahams, VO_2/TiO_2 bilayer films for energy efficient windows with multifunctional properties, J. Mater. Chem. C. 6 (2018) 4485–4493. https://doi.org/10.1039/C8TC00835C.

[9] D. Shinohara, S. Fujita, Heteroepitaxy of corundum-structured α-Ga_2O_3 thin films on α-Al_2O_3 substrates by ultrasonic mist chemical vapor deposition, Jpn. J. Appl. Phys. 47 (2008) 7311–7313. https://doi.org/10.1143/JJAP.47.7311.

[10] J.G. Lu, T. Kawaharamura, H. Nishinaka, Y. Kamada, T. Ohshima, S. Fujita, ZnO-based thin films synthesized by atmospheric pressure mist chemical vapor deposition, J. Cryst. Growth. 299 (2007) 1–10. https://doi.org/10.1016/j.jcrysgro.2006.10.251.

[11] C. Wu, F. Feng, Y. Xie, Design of vanadium oxide structures with controllable electrical properties for energy applications, Chem. Soc. Rev. 42 (2013) 5157. https://doi.org/10.1039/c3cs35508j.

[12] Z. Yang, C. Ko, S. Ramanathan, Oxide Electronics Utilizing Ultrafast Metal-Insulator Transitions, Annu. Rev. Mater. Res. 41 (2011) 337–367. https://doi.org/10.1146/annurev-

matsci-062910-100347.

[13] T.W. Chiu, K. Tonooka, N. Kikuchi, Influence of oxygen pressure on the structural, electrical and optical properties of VO_2 thin films deposited on ZnO/glass substrates by pulsed laser deposition, in: Thin Solid Films, Elsevier, 2010: pp. 7441–7444. https://doi.org/10.1016/j.tsf.2010.05.019.

[14] J.-Y. Bae, J. Park, H.Y. Kim, H.-S. Kim, J.-S. Park, Facile Route to the Controlled Synthesis of Tetragonal and Orthorhombic SnO_2 Films by Mist Chemical Vapor Deposition, ACS Appl. Mater. Interfaces. 7 (2015) 12074–12079. https://doi.org/10.1021/acsami.5b02251.

[15] D.-H. Kim, H.-J. Jeong, J. Park, J.-S. Park, The effect of solvent water content on the dielectric properties of Al_2O_3 films grown by atmospheric pressure mist-CVD, Ceram. Int. 44 (2018) 459–463. https://doi.org/10.1016/j.ceramint.2017.09.198.

[16] H. Ren, B. Li, X. Zhou, S. Chen, Y. Li, C. Hu, J. Tian, G. Zhang, Y. Pan, C. Zou, Wafer-size VO_2 film prepared by water-vapor oxidant, Appl. Surf. Sci. 525 (2020) 146642. https://doi.org/10.1016/j.apsusc.2020.146642.

[17] W. Liang, M. Gao, C. Lu, Z. Zhang, C.H. Chan, L. Zhuge, J. Dai, H. Yang, C. Chen, B.H. Park, Q. Jia, Y. Lin, Enhanced Metal-Insulator Transition Performance in Scalable Vanadium Dioxide Thin Films Prepared Using a Moisture-Assisted Chemical Solution Approach, ACS Appl. Mater. Interfaces. 10 (2018) 8341–8348. https://doi.org/10.1021/acsami.7b18533.

[18] G. Silversmit, D. Depla, H. Poelman, G.B. Marin, R. De Gryse, Determination of the V2p XPS binding energies for different vanadium oxidation states (V^{5+} to V^{0+}), J. Electron Spectros. Relat. Phenomena. 135 (2004) 167–175. https://doi.org/10.1016/j.elspec.2004.03.004.

[19] J. Zheng, S. Bao, P. Jin, TiO_2(R)/VO_2(M)/TiO_2(A) multilayer film as smart window: Combination of energy-saving, antifogging and self-cleaning functions, Nano Energy. 11 (2015) 136–145. https://doi.org/10.1016/j.nanoen.2014.09.023.

[20] Y. Gao, S. Wang, H. Luo, L. Dai, C. Cao, Y. Liu, Z. Chen, M. Kanehira, Enhanced chemical stability of VO_2 nanoparticles by the formation of SiO_2/VO_2 core/shell structures and the application to transparent and flexible VO_2-based composite foils with excellent thermochromic properti, Energy Environ. Sci. 5 (2012) 6104. https://doi.org/10.1039/c2ee02803d.

[21] T. Oshima, T. Nakazono, A. Mukai, A. Ohtomo, Epitaxial growth of γ-Ga_2O_3 films by mist chemical vapor deposition, J. Cryst. Growth. 359 (2012) 60–63. https://doi.org/10.1016/j.jcrysgro.2012.08.025.

[22] T. Ikenoue, J. Inoue, M. Miyake, T. Hirato, Epitaxial growth of undoped and Li-doped NiO thin films on α-Al_2O_3 substrates by mist chemical vapor deposition, J. Cryst. Growth. 507

(2019) 379–383. https://doi.org/10.1016/j.jcrysgro.2018.11.032.

[23] X. Zhao, J. Cheng, Atmospheric preparation of ZnO thin films by mist chemical vapor deposition for spray-coated organic solar cells, J. Mater. Sci. Mater. Electron. 27 (2016) 2676–2681. https://doi.org/10.1007/s10854-015-4076-y.

[24] Z. Sun, D. Oka, T. Fukumura, Epitaxial Growth of β-Bi_2O_3 Thin Films and Particles with Mist Chemical Vapor Deposition, Cryst. Growth Des. 19 (2019) 7170–7174. https://doi.org/10.1021/acs.cgd.9b01033.

[25] V. Bondarenka, V. Jasulaitienė, R. Sereika, A. Stirkė, Sol–gel synthesis and XPS study of vanadium pentoxide xerogels intercalated with glucose, J. Sol-Gel Sci. Technol. 71 (2014) 385–390. https://doi.org/10.1007/s10971-014-3385-6.

[26] E. Hryha, E. Rutqvist, L. Nyborg, Stoichiometric vanadium oxides studied by XPS, Surf. Interface Anal. 44 (2012) 1022–1025. https://doi.org/10.1002/sia.3844.

[27] J.K. Tripathi, T.J. Novakowski, A. Hassanein, Tuning surface porosity on vanadium surface by low energy He^+ ion irradiation, Appl. Surf. Sci. 378 (2016) 63–72. https://doi.org/10.1016/j.apsusc.2016.03.196.

[28] F. Ureña-Begara, A. Crunteanu, J.-P. Raskin, Raman and XPS characterization of vanadium oxide thin films with temperature, Appl. Surf. Sci. 403 (2017) 717–727. https://doi.org/10.1016/j.apsusc.2017.01.160.

[29] G. Silversmit, D. Depla, H. Poelman, G.B. Marin, R. De Gryse, An XPS study on the surface reduction of V_2O_5(001) induced by Ar^+ ion bombardment, Surf. Sci. 600 (2006) 3512–3517. https://doi.org/10.1016/j.susc.2006.07.006.

[30] A. Pajares, H. Prats, A. Romero, F. Viñes, P.R. de la Piscina, R. Sayós, N. Homs, F. Illas, Critical effect of carbon vacancies on the reverse water gas shift reaction over vanadium carbide catalysts, Appl. Catal. B Environ. 267 (2020) 118719. https://doi.org/10.1016/j.apcatb.2020.118719.

[31] Z. Zhang, Y. Gao, Z. Chen, J. Du, C. Cao, L. Kang, H. Luo, Thermochromic VO_2 thin films: Solution-based processing, improved optical properties, and lowered phase transformation temperature, Langmuir. 26 (2010) 10738–10744. https://doi.org/10.1021/la100515k.

[32] T.. Hanlon, R.. Walker, J.. Coath, M.. Richardson, Comparison between vanadium dioxide coatings on glass produced by sputtering, alkoxide and aqueous sol–gel methods, Thin Solid Films. 405 (2002) 234–237. https://doi.org/10.1016/S0040-6090(01)01753-9.

[33] M. Zhu, H. Wang, C. Li, H. Qi, D. Zhang, W. Lv, Thickness-modulated thermochromism of vanadium dioxide thin films grown by magnetron sputtering, Surf. Coatings Technol. 359 (2019) 396–402. https://doi.org/10.1016/j.surfcoat.2018.12.077.

[34] Y. Gao, H. Luo, Z. Zhang, L. Kang, Z. Chen, J. Du, M. Kanehira, C. Cao, Nanoceramic VO_2 thermochromic smart glass: A review on progress in solution processing, Nano Energy. 1

(2012) 221–246. https://doi.org/10.1016/j.nanoen.2011.12.002.

[35] D. Zhang, M. Zhu, Y. Liu, K. Yang, G. Liang, Z. Zheng, X. Cai, P. Fan, High performance VO_2 thin films growth by DC magnetron sputtering at low temperature for smart energy efficient window application, J. Alloys Compd. 659 (2016) 198–202. https://doi.org/10.1016/j.jallcom.2015.11.047.

[36] J. Vlček, D. Kolenatý, J. Houška, T. Kozák, R. Čerstvý, Controlled reactive HiPIMS—effective technique for low-temperature (300 °C) synthesis of VO_2 films with semiconductor-to-metal transition, J. Phys. D. Appl. Phys. 50 (2017) 38LT01. https://doi.org/10.1088/1361-6463/aa8356.

[37] M. Xygkis, E. Gagaoudakis, L. Zouridi, O. Markaki, E. Aperathitis, K. Chrissopoulou, G. Kiriakidis, V. Binas, Thermochromic Behavior of VO_2/Polymer Nanocomposites for Energy Saving Coatings, Coatings. 9 (2019) 163. https://doi.org/10.3390/coatings9030163.

[38] L. Zhao, L. Miao, S. Tanemura, J. Zhou, L. Chen, X. Xiao, G. Xu, A low cost preparation of VO_2 thin films with improved thermochromic properties from a solution-based process, Thin Solid Films. 543 (2013) 157–161. https://doi.org/10.1016/j.tsf.2012.11.154.

[39] Y. Cui, Y. Ke, C. Liu, Z. Chen, N. Wang, L. Zhang, Y. Zhou, S. Wang, Y. Gao, Y. Long, Thermochromic VO_2 for Energy-Efficient Smart Windows, Joule. 2 (2018) 1707–1746. https://doi.org/10.1016/j.joule.2018.06.018.

[40] J. Kim, T. Ejiri, M. Sugiyama, Investigation of VO_2 directly deposited on a glass substrate using RF sputtering for a smart window, Jpn. J. Appl. Phys. 59 (2020) 105506. https://doi.org/10.35848/1347-4065/abbb1d.

[41] C. Ji, Z. Wu, X. Wu, J. Wang, J. Gou, Z. Huang, H. Zhou, W. Yao, Y. Jiang, Al-doped VO_2 films as smart window coatings: Reduced phase transition temperature and improved thermochromic performance, Sol. Energy Mater. Sol. Cells. 176 (2018) 174–180. https://doi.org/10.1016/j.solmat.2017.11.026.

[42] S. Long, X. Cao, G. Sun, N. Li, T. Chang, Z. Shao, P. Jin, Effects of V_2O_3 buffer layers on sputtered VO_2 smart windows: Improved thermochromic properties, tunable width of hysteresis loops and enhanced durability, Appl. Surf. Sci. 441 (2018) 764–772. https://doi.org/10.1016/j.apsusc.2018.02.083.

[43] X. Wu, Z. Wu, H. Zhang, R. Niu, Q. He, C. Ji, J. Wang, Y. Jiang, Enhancement of VO_2 thermochromic properties by Si doping, Surf. Coatings Technol. 276 (2015) 248–253. https://doi.org/10.1016/j.surfcoat.2015.07.007.

[44] M.K. Dietrich, B.G. Kramm, M. Becker, B.K. Meyer, A. Polity, P.J. Klar, Influence of doping with alkaline earth metals on the optical properties of thermochromic VO_2, J. Appl. Phys. 117 (2015) 185301. https://doi.org/10.1063/1.4919433.

[45] M. Jiang, S. Bao, X. Cao, Y. Li, S. Li, H. Zhou, H. Luo, P. Jin, Improved luminous

transmittance and diminished yellow color in VO_2 energy efficient smart thin films by Zn doping, Ceram. Int. 40 (2014) 6331–6334. https://doi.org/10.1016/j.ceramint.2013.10.083.

[46] H. Guan, D. Zhang, Y. Yang, Y. Liu, A. Zhong, Q. He, J. Qi, P. Fan, A Novel Method for Notable Reducing Phase Transition Temperature of VO_2 Films for Smart Energy Efficient Windows, Nanomaterials. 10 (2019) 58. https://doi.org/10.3390/nano10010058.

[47] S. Long, X. Cao, Y. Wang, T. Chang, N. Li, L. Jin, L. Ma, F. Xu, G. Sun, P. Jin, Karst landform-like VO_2 single layer solution: Controllable morphology and excellent optical performance for smart glazing applications, Sol. Energy Mater. Sol. Cells. 209 (2020) 110449. https://doi.org/10.1016/j.solmat.2020.110449.

[48] M.J. Miller, J. Wang, Influence of grain size on transition temperature of thermochromic VO_2, J. Appl. Phys. 117 (2015) 034307. https://doi.org/10.1063/1.4906122.

[49] E. Gagaoudakis, E. Aperathitis, G. Michail, M. Panagopoulou, D. Katerinopoulou, V. Binas, Y.S. Raptis, G. Kiriakidis, Low-temperature rf sputtered VO_2 thin films as thermochromic coatings for smart glazing systems, Sol. Energy. 165 (2018) 115–121. https://doi.org/10.1016/j.solener.2018.03.010.

[50] H. Koo, H. You, K.-E. Ko, O.-J. Kwon, S.-H. Chang, C. Park, Thermochromic properties of VO_2 thin film on SiN_x buffered glass substrate, Appl. Surf. Sci. 277 (2013) 237–241. https://doi.org/10.1016/j.apsusc.2013.04.031.

[51] G. Fu, A. Polity, N. Volbers, B.K. Meyer, Annealing effects on VO_2 thin films deposited by reactive sputtering, Thin Solid Films. 515 (2006) 2519–2522. https://doi.org/10.1016/j.tsf.2006.04.025.

[52] T. Lin, Y. Zhang, D. Zheng, The ultrathin VO2(M) film with ultrahigh visible transmittance synthesized on the quartz glass substrate by HiPIMS, Vacuum. 156 (2018) 449–455. https://doi.org/10.1016/j.vacuum.2018.08.008.

[53] H.-C. Ho, Y.-C. Lai, K. Chen, T.D. Dao, C.-H. Hsueh, T. Nagao, High quality thermochromic VO_2 films prepared by magnetron sputtering using V_2O_5 target with in situ annealing, Appl. Surf. Sci. 495 (2019) 143436. https://doi.org/10.1016/j.apsusc.2019.07.178.

[54] P. Jin, S. Tanemura, Formation and Thermochromism of VO_2 Films Deposited by RF Magnetron Sputtering at Low Substrate Temperature, Jpn. J. Appl. Phys. 33 (1994) 1478–1483. https://doi.org/10.1143/JJAP.33.1478.

[55] B. Zhu, H. Tao, X. Zhao, Effect of buffer layer on thermochromic performances of VO_2 films fabricated by magnetron sputtering, Infrared Phys. Technol. 75 (2016) 22–25. https://doi.org/10.1016/j.infrared.2016.01.004.

[56] Y. Shigesato, M. Enomoto, H. Odaka, Thermochromic VO_2 Films Deposited by RF Magnetron Sputtering Using V_2O_3 or V_2O_5 Targets, Jpn. J. Appl. Phys. 39 (2000) 6016–6024. https://doi.org/10.1143/JJAP.39.6016.

[57] Y. Yang, X. Cao, G. Sun, S. Long, T. Chang, X. Li, P. Jin, Transmittance change with thickness for polycrystalline VO_2 films deposited at room temperature, J. Alloys Compd. 791 (2019) 648–654. https://doi.org/10.1016/j.jallcom.2019.03.278.

[58] X. Lv, Y. Cao, L. Yan, Y. Li, L. Song, Atomic layer deposition of VO_2 films with Tetrakis-dimethyl-amino vanadium (IV) as vanadium precursor, Appl. Surf. Sci. 396 (2017) 214–220. https://doi.org/10.1016/j.apsusc.2016.10.044.

[59] H. Kim, N. Charipar, E. Breckenfeld, A. Rosenberg, A. Piqué, Active terahertz metamaterials based on the phase transition of VO_2 thin films, Thin Solid Films. 596 (2015) 45–50. https://doi.org/10.1016/j.tsf.2015.07.062.

[60] D. Malarde, M.J. Powell, R. Quesada-Cabrera, R.L. Wilson, C.J. Carmalt, G. Sankar, I.P. Parkin, R.G. Palgrave, Optimized Atmospheric-Pressure Chemical Vapor Deposition Thermochromic VO_2 Thin Films for Intelligent Window Applications, ACS Omega. 2 (2017) 1040–1046. https://doi.org/10.1021/acsomega.7b00042.

[61] S. Ji, F. Zhang, P. Jin, Preparation of high performance pure single phase VO_2 nanopowder by hydrothermally reducing the V_2O_5 gel, Sol. Energy Mater. Sol. Cells. 95 (2011) 3520–3526. https://doi.org/10.1016/j.solmat.2011.08.015.

[62] W. Li, S. Ji, Y. Li, A. Huang, H. Luo, P. Jin, Synthesis of VO_2 nanoparticles by a hydrothermal-assisted homogeneous precipitation approach for thermochromic applications, RSC Adv. 4 (2014) 13026–13033. https://doi.org/10.1039/c3ra47666a.

[63] L. Dai, S. Chen, J. Liu, Y. Gao, J. Zhou, Z. Chen, C. Cao, H. Luo, M. Kanehira, F-doped VO_2 nanoparticles for thermochromic energy-saving foils with modified color and enhanced solar-heat shielding ability, Phys. Chem. Chem. Phys. 15 (2013) 11723–11729. https://doi.org/10.1039/c3cp51359a.

[64] Z. Zhao, Y. Liu, D. Wang, C. Ling, Q. Chang, J. Li, Y. Zhao, H. Jin, Sn dopants improve the visible transmittance of VO_2 films achieving excellent thermochromic performance for smart window, Sol. Energy Mater. Sol. Cells. 209 (2020) 110443. https://doi.org/10.1016/j.solmat.2020.110443.

[65] N. Wang, M. Duchamp, R.E. Dunin-Borkowski, S. Liu, X. Zeng, X. Cao, Y. Long, Terbium-Doped VO_2 Thin Films: Reduced Phase Transition Temperature and Largely Enhanced Luminous Transmittance, Langmuir. 32 (2016) 759–764. https://doi.org/10.1021/acs.langmuir.5b04212.

Chapter 4
Formation of Uniquely Oriented VO_2 Thin Film by Topotactic Oxidation of V_2O_3 Epitaxial Film on R-plane Al_2O_3

4.1 Introduction

In Chapter 3, the author described the fabrication of randomly oriented VO_2 films by mist CVD and their thermochromic properties. The results indicated that the deposited VO_2 is promising for application in smart windows. However, the usage of VO_2 films in switching devices requires a large resistivity change across the MIT rather than excellent thermochromic properties. Highly oriented VO_2 films are suitable for switching applications because they show larger resistivity changes across MIT (in the order of 10^3–10^5) than randomly oriented polycrystalline VO_2 films (in the order of 10^1–10^3) [1–7].

In addition to the degree of orientation, the direction of orientation plays an important role in improving the performance of the material and developing devices with new functions. The crystal orientation of oxide films is known to affect their properties, such as catalytic activity [8], chemical reaction rate [9], and electrical properties [10]. In VO_2, the reaction rate of the insertion of H^+ ions, which triggers the phase transition process, has been found to be anisotropic [11]. Taking the advantage of this anisotropy, a synaptic transistor based on two differently oriented VO_2 films has been developed [12].

As a route for the fabrication of oriented VO_2 films, in addition to the direct epitaxial deposition of VO_2 on a single crystal substrate [1,4], the topotactic oxidation of V_2O_3 epitaxial films has been reported [13,14]. Topotactic oxidation is an oxidation reaction in which the crystallographic orientation of the reactant determines the orientation of the oxidation product. The formation of a biaxially oriented VO_2 film by the thermal oxidation of a V_2O_3 epitaxial film on a C-plane Al_2O_3 substrate has been reported [13]. Furthermore, Okimura et al. reported that a VO_2 film prepared via topotactic oxidation exhibits larger resistivity change across MIT than an epitaxial VO_2

film directly deposited by sputtering [14].

Previous studies on the topotactic oxidation of V_2O_3 to VO_2 were performed only for V_2O_3 epitaxial films on a C-plane Al_2O_3 substrate. It should be interesting to know whether the topotactic oxidation occurs in the same way even when an R-plane Al_2O_3 substrate is used because according to simple geometric calculations, the VO_2 topotactically transformed from epitaxial V_2O_3 on R-plane Al_2O_3 shows unique orientations to the substrate, which is difficult to achieve by direct epitaxial deposition.

In this chapter, the author reports thermal oxidation of V_2O_3 epitaxial films on an R-plane Al_2O_3 substrate deposited by mist CVD. In addition, the crystallographic orientations of the resulting VO_2 films are presented. The V_2O_3 epitaxial films were thermally oxidized at different temperatures for various durations, and the optimal conditions for obtaining a highly-oriented single-phase VO_2 film were determined. The VO_2 films showed unique orientations with the $(2\bar{3}\bar{1})$ or $(23\bar{1})$ planes almost parallel to the substrate. These are out-of-plane orientations that have never been reported before. The mechanism for the topotactic oxidation of V_2O_3 to VO_2 and the contribution of the substrate to the oxidation process were investigated. The VO_2 films formed via the topotactic oxidation of V_2O_3 films showed a decrease of more than four orders of magnitude in resistance across MIT, which is comparable to that of VO_2 epitaxial films.

4.2 Experimental

4.2.1 Materials

The precursor solution for the mist CVD of V_2O_3 was prepared by dissolving bis(acetylacetonato) vanadium oxide (98%, STREM, USA) in methanol (Wako, Japan) at a concentration of 0.010 mol/L. An R-plane sapphire plate (R-plane Al_2O_3, KYOCERA, Japan) was used as the substrate for the mist CVD process. Before use, the substrate was washed sequentially with acetone, distilled water, and isopropanol in an ultrasonic cleaner and dried by blowing air.

4.2.2 Mist CVD of V_2O_3

A custom-built hot-wall mist CVD system was used for the deposition of V_2O_3 films. The apparatus and procedure for mist CVD were the same as those described in Chapter 3. The mist CVD was performed by supplying the precursor mist through N_2 at a flow rate of 6.0 L min^{-1} to the substrate heated to a predetermined temperature (450–650 °C) for 10 min. After the mist supply was turned off, the substrate was cooled to <100 °C in a furnace under the flow of N_2 gas.

4.2.3 Thermal oxidation

The thermal oxidation of the deposited films was carried out in the CVD system. The films were heated to 400–550 °C under the flow of N_2-1 vol.% O_2 gas at a rate of 5 L min^{-1}. After reaching the predetermined temperature, the film was maintained at this temperature for 30–240 min and then cooled to < 100 °C in the furnace under the flow of N_2 gas.

4.2.4 Characterization of the films

XRD θ–2θ measurements and pole figure measurements, SEM observation were

carried out with same instruments as those described in Chapter 2 and 3. The electrical resistance of the films was measured using the two-probe method with a source meter (2450 SourceMeter, KEITHLEY) while changing the temperature of the films using a custom-made oil bath. VESTA was used to analyze the atomic arrangements of V_2O_3 and VO_2 [15].

Although the crystal structure of VO_2 was monoclinic during the characterization at room temperature and rutile during the thermal oxidation, all the crystal orientations of the VO_2 films are expressed in the (pseudo) rutile notation for simplicity in this chapter, in line with many other studies [12,13,16].

4.3 Result and Discussion

4.3.1 V_2O_3 epitaxial growth by mist CVD

Prior to the fabrication of VO_2 by thermal oxidation, the precursor V_2O_3 films were prepared on R-plane Al_2O_3 substrates by mist CVD. V_2O_3 is expected to grow epitaxially on an R-plane Al_2O_3 substrate, following the substrate crystallographic orientation, because both V_2O_3 and Al_2O_3 show the corundum structure and the lattice mismatches between them along the a-and c-axes are 4.1% and 8.3%, respectively.

Figure 4-1a shows the XRD θ–2θ patterns of the films deposited at 450–650 °C. All the films showed three diffraction peaks at $2\theta = 24°$, 50°, and 79° corresponding to the (012), (024), and (036) planes of V_2O_3, respectively. The absence of other detectable peaks indicates that the films consisted of a single V_2O_3 phase. Furthermore, the detection of only the diffraction peaks of the (012) and higher-order planes of V_2O_3 indicates that the (012) plane in the as-deposited V_2O_3 films was parallel to the substrate surface.

The in-plane orientation of the V_2O_3 film deposited at 550 °C was identified by analyzing its V_2O_3 (104) ($2\theta = 33.1°$) and Al_2O_3 (104) ($2\theta = 35.1°$) pole figures (Figure 4-1b and Figure 4-2a) after the deposition. By comparing the pole figures measured for the bare substrate at the same 2θ angle (Figure 4-1b vs. Figure 4-1d and Figure 4-2a vs. Figure 4-2b), the diffraction spots for the film and substrate could be distinguished. All the six diffraction spots in the V_2O_3 (104) pole figure (Figure 4-1b) could be attributed to the film and not to the substrate. Among the five spots in the Al_2O_3 (104) pole figure (Figure 4-2a), the three intense spots marked by red circles correspond to the substrate, while the other two weak spots marked with green squares correspond to V_2O_3 (110), whose diffraction peak angle ($2\theta = 36.2°$) is close to that of Al_2O_3 (104) ($2\theta = 35.1°$).

The pattern of the spots marked with red circles in the V_2O_3 (104) pole figure of the film (Figure 4-1b) is consistent with that of the Al_2O_3 (104) pole figure (Figure 4-2a), indicating that the deposited film contained V_2O_3 crystals grown epitaxially in accordance with the crystal orientation of the Al_2O_3 substrate, i.e., Al_2O_3 (012)[100] // V_2O_3 (012)[100]. The V_2O_3 crystals with this orientation were denoted as (012)-oriented V_2O_3. The other three spots marked with white circles in the V_2O_3 (104) pole figure (Figure

4-1b) indicate the presence of a V_2O_3 crystal with another orientation, which coincided with the (012)-oriented V_2O_3 when rotated by 60° around the c-axis. The orientation of this crystal with respect to the substrate was Al_2O_3 (012)[100] // V_2O_3 (102)[0$\bar{1}$0]. The crystal with this orientation was denoted as (102)-oriented V_2O_3. The orientation relationship between the two V_2O_3 crystals is shown in Figure 4-3. The positions of the V_2O_3 (110) diffraction spots detected in the Al_2O_3 (104) pole figure (Figure 4-2a) can also be explained by the presence of V_2O_3 crystals with these two orientations (Figure 4-2c). The V_2O_3 (104) pole figures of the (012)- and (102)-oriented V_2O_3 (Figure 4-1c) were in good agreement with the pattern observed in the film (Figure 4-1b).

The films prepared at the other temperatures exhibited the same spot patterns in the pole figures (Figure 4-4), indicating the presence of crystals with the aforementioned orientations. Furthermore, the size of the diffraction spots indicates that the film deposited at the higher temperature of 650 °C showed lower crystallinity. As shown in the later section (4.3.3 Topotactic relationship), the presence of the crystals with a rotated orientation in the V_2O_3 film did not affect the orientation of the resulting VO_2 films.

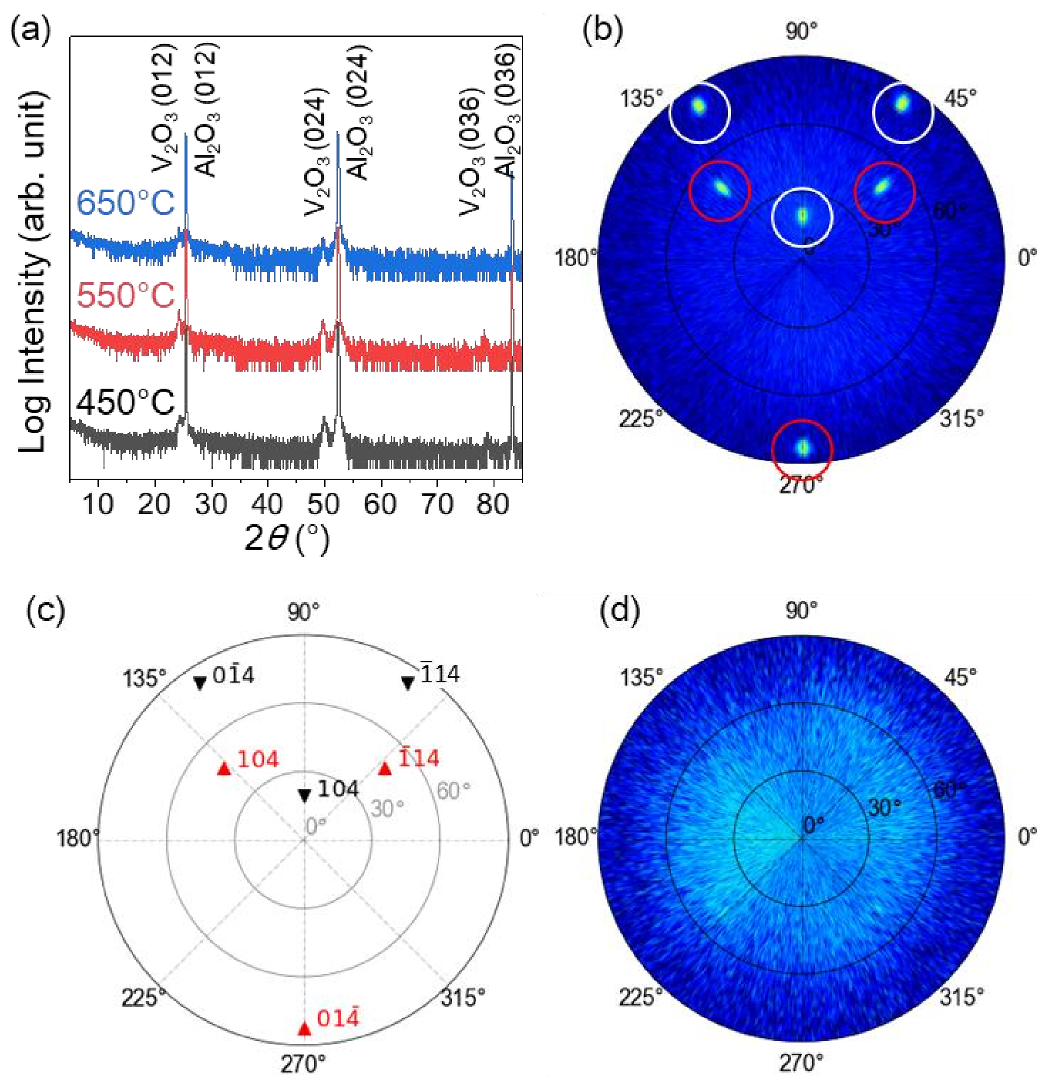

Figure 4-1 (a) XRD θ–2θ patterns of the films deposited by mist CVD at 450–650 °C on R-plane Al_2O_3 substrates. (b) V_2O_3 (104) pole figure of the sample obtained after the deposition at 550 °C. (c) Simulation of the V_2O_3 (104) pole figure for a film composed of (012)-oriented (▲) and (102)-oriented V_2O_3 (▼). (d) Pole figure measured for the bare substrate at $2\theta = 33.1°$ corresponding to the V_2O_3 (104) diffraction angle.

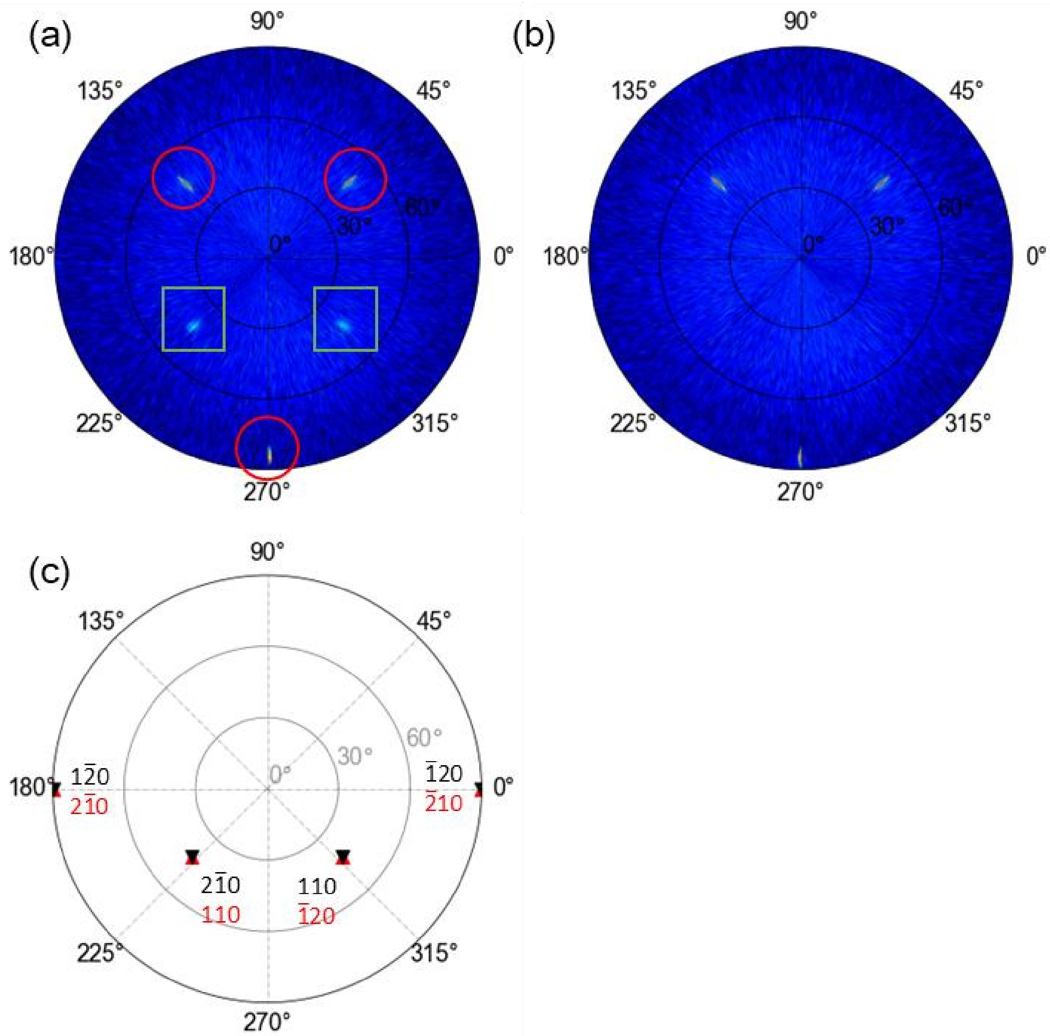

Figure 4-2 Al_2O_3 (104) pole figures measured for (a) the sample after the film deposition at 550 °C and (b) the substrate. (c) V_2O_3 (110) pole figure simulated for a film composed of (012)-oriented V_2O_3 (▲) and (102)-oriented V_2O_3 (▼).

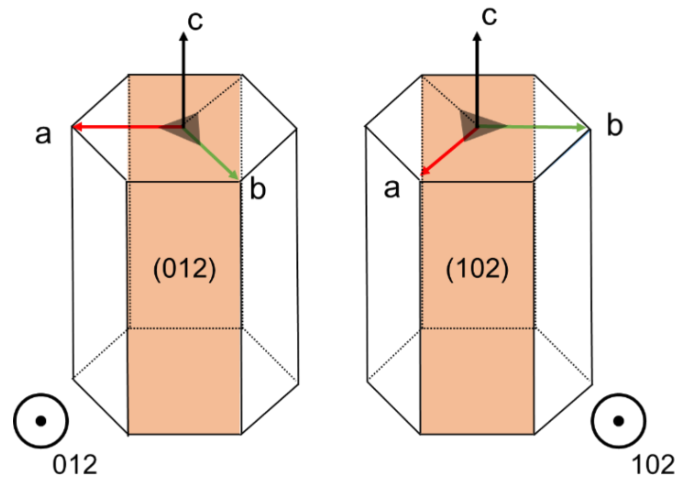

Figure 4-3 Orientation relationship between the (012)- and (102)-oriented V_2O_3 crystals. The black triangles are included to show the three-fold symmetric nature of V_2O_3 around the c-axis.

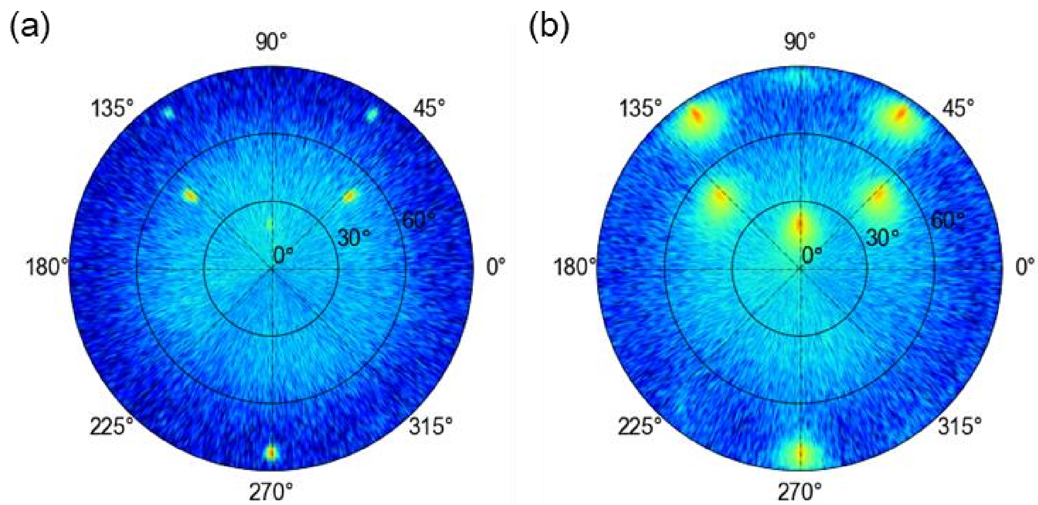

Figure 4-4 Pole figures measured for the V_2O_3 thin films deposited on an R-plane Al_2O_3 substrate at (a) 450 and (b) 650 °C.

4.3.2 Oxidation to VO_2

The V_2O_3 epitaxial film deposited at 550 °C was thermally oxidized at various temperatures for various durations to obtain VO_2. Figure 4-5a shows the XRD θ–2θ patterns of the samples oxidized at 400–550 °C for 30 min. The diffraction peaks characteristic of V_2O_3 could be detected even after the oxidation at $\leq$450 °C. However, the intensity of these peaks decreased with an increase in the oxidation temperature. When the oxidation temperature was increased to 500 °C, the diffraction peaks corresponding to V_2O_3 disappeared and no peaks were detected in the film. When the oxidation temperature was further increased to 550 °C, diffraction peaks corresponding to V_2O_5 appeared. The trivalent oxide (V_2O_3) existed below 450 °C, while the pentavalent oxide (V_2O_5) was generated at 550 °C. Therefore, the tetravalent oxide (VO_2) was expected to be generated at approximately 500 °C. However, no diffraction peaks of VO_2 were detected for the sample oxidized at 500 °C.

Similarly, in the case of the samples oxidized at 450 °C for different durations, the intensity of the V_2O_3 diffraction peaks decreased with an increase in the oxidation time, and no diffractions were detected for the films oxidized for $\geq$120 min (Figure 4-5b).

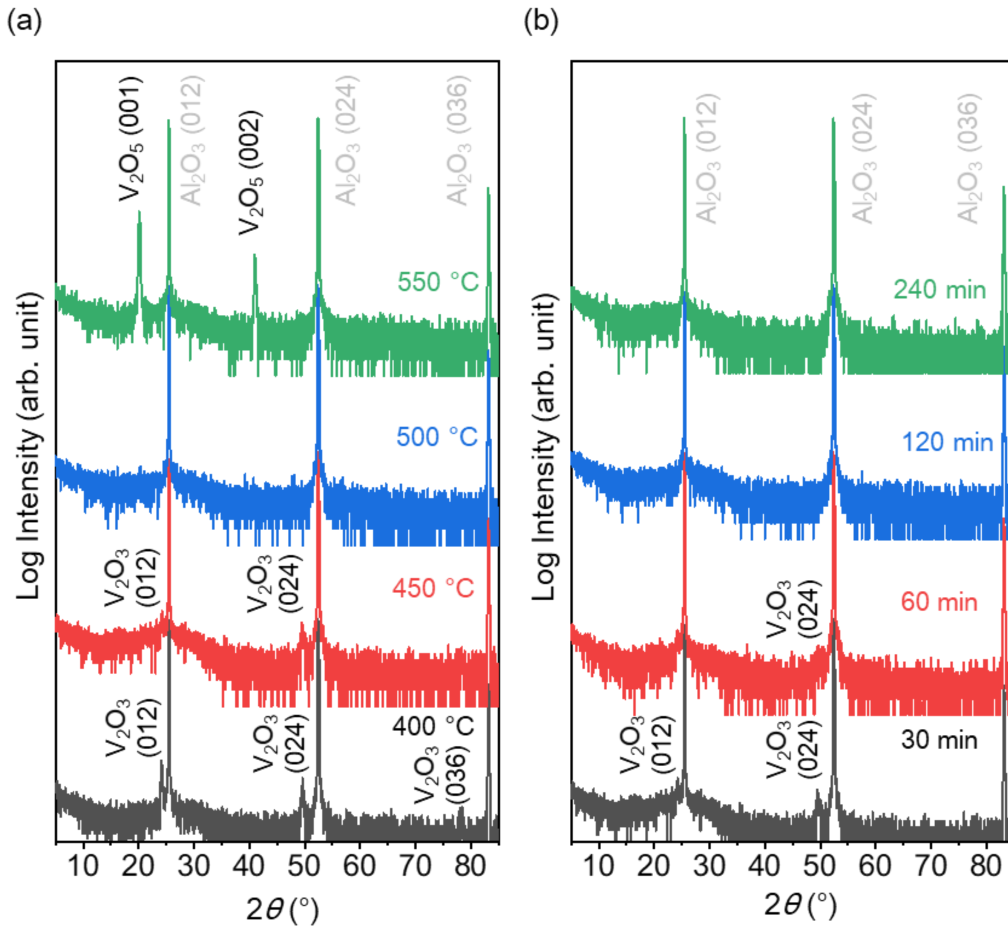

Figure 4-5 XRD θ–2θ patterns of the samples after the oxidation (a) at 400–550 °C for 30 min and (b) at 450 °C for 30–240 min.

Although no VO_2 diffraction peak was detected, VO_2 was expected to be formed before the oxidation of V_2O_3 to V_2O_5. Suspecting the formation of VO_2 with a peculiar orientation that was slightly off the substrate normal, the author performed pole figure measurements at the 2θ angles corresponding to the (101), (111), and $(2\bar{3}\bar{1})$ diffraction peaks of VO_2 for the sample oxidized at 450 °C for 120 min. As shown in Figure 4-6a–c, the diffractions at these 2θ angles were clearly observed in the film when the sample was tilted and rotated to specific angles, confirming the formation of VO_2 crystals with certain orientations.

The crystal orientation of the VO_2 film obtained after the thermal oxidation at 450 °C for 120 min was identified by analyzing the VO_2 (101) pole figure (Figure 4-6a). Assuming that the diffraction spot at $(\varphi, \chi) = (180°, 90°)$ in the pole figure was attributed

to $(0\bar{1}1)$, the calculations showed that the spot due to $(0\bar{1}\bar{1})$ could appear on the red line drawn on the pole figure (Figure 4-7). Accordingly, the diffraction spot on the line at (φ, χ) = (312°, 39°) could be attributed to $(0\bar{1}\bar{1})$. The directions of these planes uniquely determined the orientation of the VO_2 crystal, and the spots at (φ, χ) = (316°, 84°), (0°, 90°), and (17°, 48°) corresponded to the $(\bar{1}0\bar{1})$, $(01\bar{1})$, and $(10\bar{1})$ planes, respectively. In this orientation, the $(2\bar{3}\bar{1})$ plane of the VO_2 crystal tilted a few degrees to the substrate. The VO_2 crystal with this orientation is denoted as near $(2\bar{3}\bar{1})$-oriented VO_2. Here, the author assumed that the diffraction spot at (φ, χ) = (180°, 90°) was attributed to $(0\bar{1}1)$. However, even if this discussion started with the assumption that any one of the diffraction spots marked by the red circles in Figure 4-6a corresponded to any of the {101} planes, the equivalent crystal orientation would have been derived.

However, the near $(2\bar{3}\bar{1})$-oriented VO_2 did not explain the spots marked by the white circles in the pole figure. Then, another assumption that the diffraction spot at (φ, χ) = (0°, 90°) was attributed to $(0\bar{1}1)$ leads to the conclusion that the spots at (φ, χ) = (224°, 84°), (180°, 90°), (228°, 39°), and (163°, 48°) corresponded to the $(\bar{1}0\bar{1})$, $(0\bar{1}\bar{1})$, $(01\bar{1})$, and $(10\bar{1})$ planes, respectively. The VO_2 in this orientation had $(23\bar{1})$ planes tilted a few degrees to the substrate and was coincident with the VO_2 identified earlier when it was rotated approximately 115° around the a-axis. The VO_2 crystal in this orientation was denoted as near $(23\bar{1})$-oriented VO_2. The simulated patterns of the (101), (111), and $(2\bar{3}\bar{1})$ pole figures of the near $(2\bar{3}\bar{1})$-and $(23\bar{1})$-oriented VO_2 are shown in Figure 4-6d-f, reproducing the measured pole figures. The $(2\bar{3}\bar{1})$ pole figure (Figure 4-6c) included the diffractions from the substrate (Figure 4-8). The matching of the simulated and measured patterns confirms the orientation of VO_2 discussed here.

Figures 4-9d and e show the pole figures of the representative crystal planes of the VO_2 crystals with the two orientations. The $(2\bar{3}\bar{1})$ and $(23\bar{1})$ planes of these crystals were almost parallel to the substrate surface but tilted by a few degrees. In these orientations, any plane showing diffraction within the 2θ range of 0–90° was not parallel to the substrate, explaining the fact that no diffraction was detected in the normal θ–2θ scan. No VO_2 film with these orientations has been reported previously.

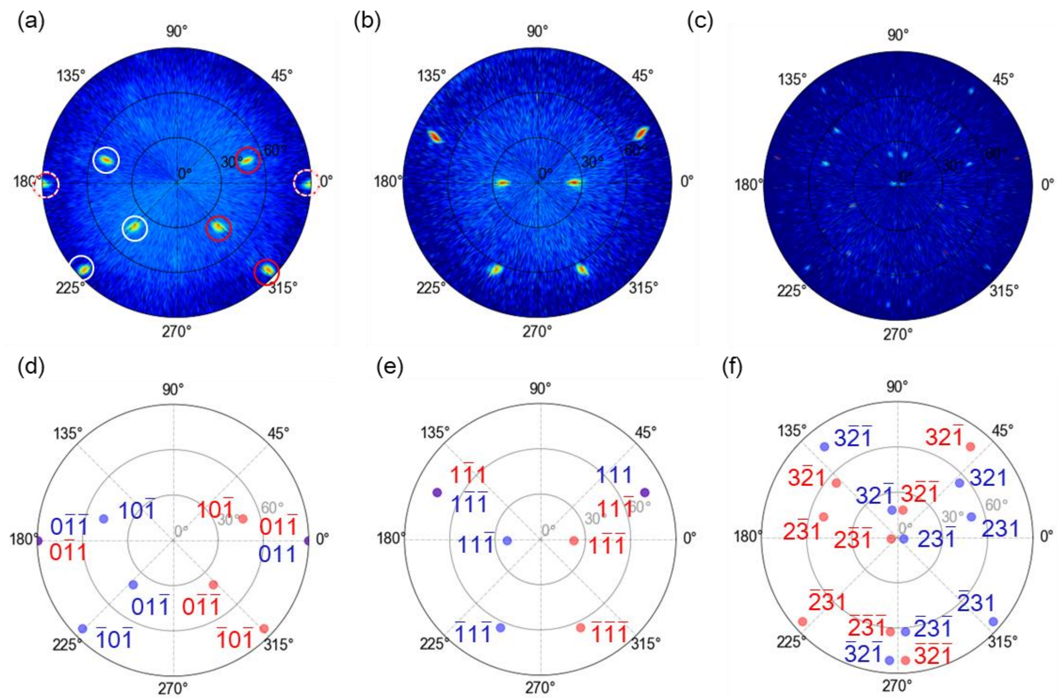

Figure 4-6 (a–c) XRD pole figures for the sample oxidized at 450 °C for 120 min measured at the 2θ angles corresponding to the diffraction angles of (a) VO_2 (101), (b) VO_2 (111), and (c) VO_2 ($2\bar{3}\bar{1}$). (d–f) Simulation of the (c) VO_2 (101), (d) VO_2 (111), and (e) VO_2 ($2\bar{3}\bar{1}$) pole figures for a film composed of near ($2\bar{3}\bar{1}$)- (●) and ($23\bar{1}$)-oriented VO_2(●).

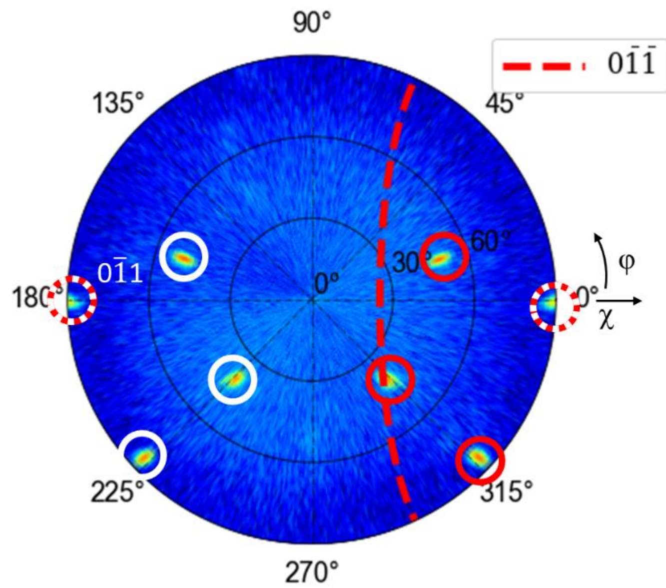

Figure 4-7 $VO_2(101)$ pole figure. Calculation on the assumption that the diffraction spot at (φ, χ) = (180°, 90°) corresponded to the $(0\bar{1}1)$ plane indicates that the $(0\bar{1}\bar{1})$ diffraction spot could appear on the dashed line.

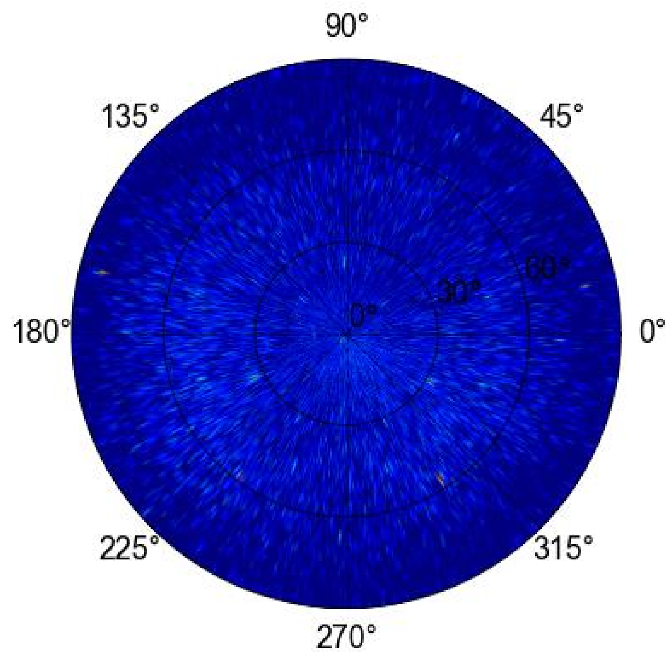

Figure 4-8 XRD pole figures measured for the bare substrate at 2θ angles corresponding to the diffraction angles of VO_2 $(2\bar{3}\bar{1})$.

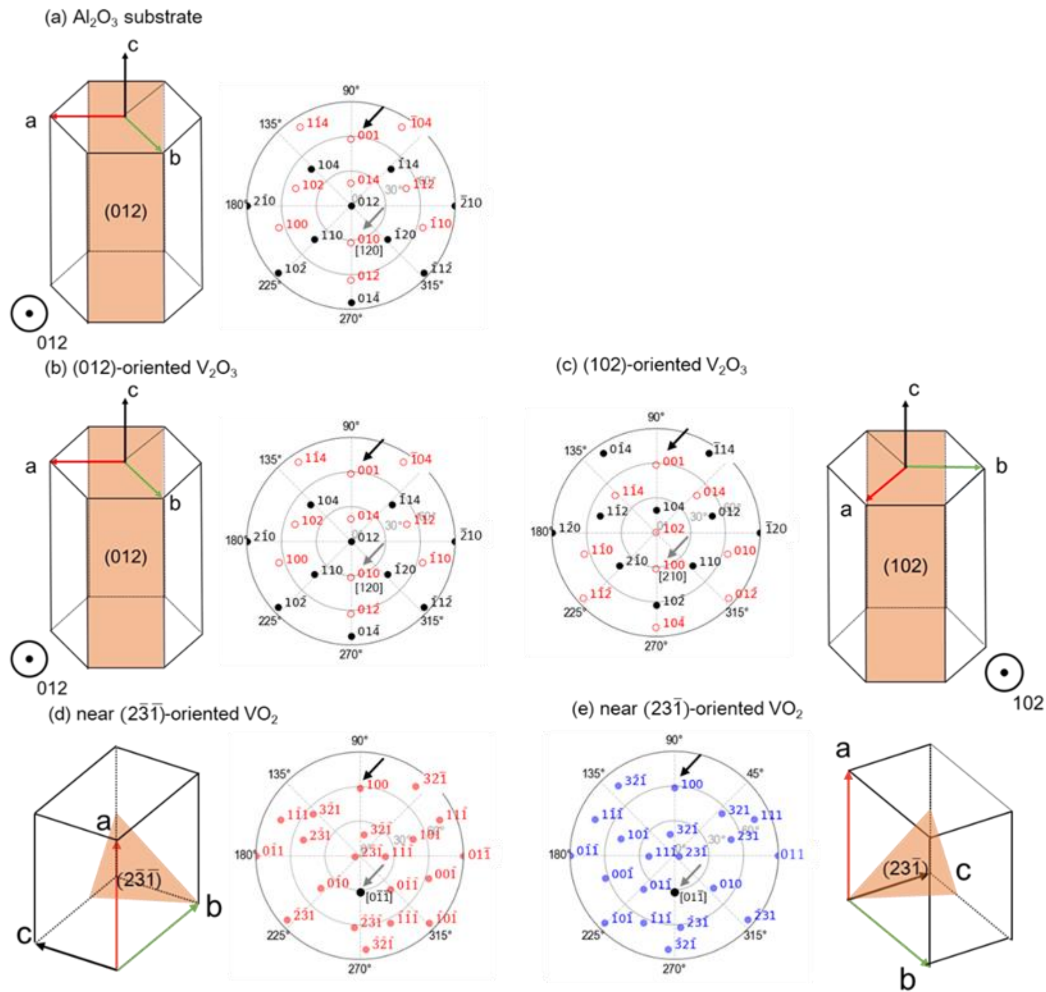

Figure 4-9 Schematic representation showing the orientation relationship among the (a) Al_2O_3 crystals of the substrate, (b, c) V_2O_3 crystals deposited on the substrate, and (d, e) VO_2 crystals produced by the oxidation of V_2O_3.The orientation of each crystal is indicated by the poles of the representative crystal planes.

The same diffraction pattern was observed in the VO_2 (101) pole figures of the samples oxidized at different temperatures for different durations (Figure 4-10), indicating that all the samples oxidized under the conditions investigated in this study consisted of near $(2\bar{3}\bar{1})$- and $(23\bar{1})$-oriented VO_2. However, on the basis of the θ–2θ scan, it can be stated that only the films oxidized at 450 °C for ≥120 min and at 500 °C for 30 min consisted of single-phase VO_2.

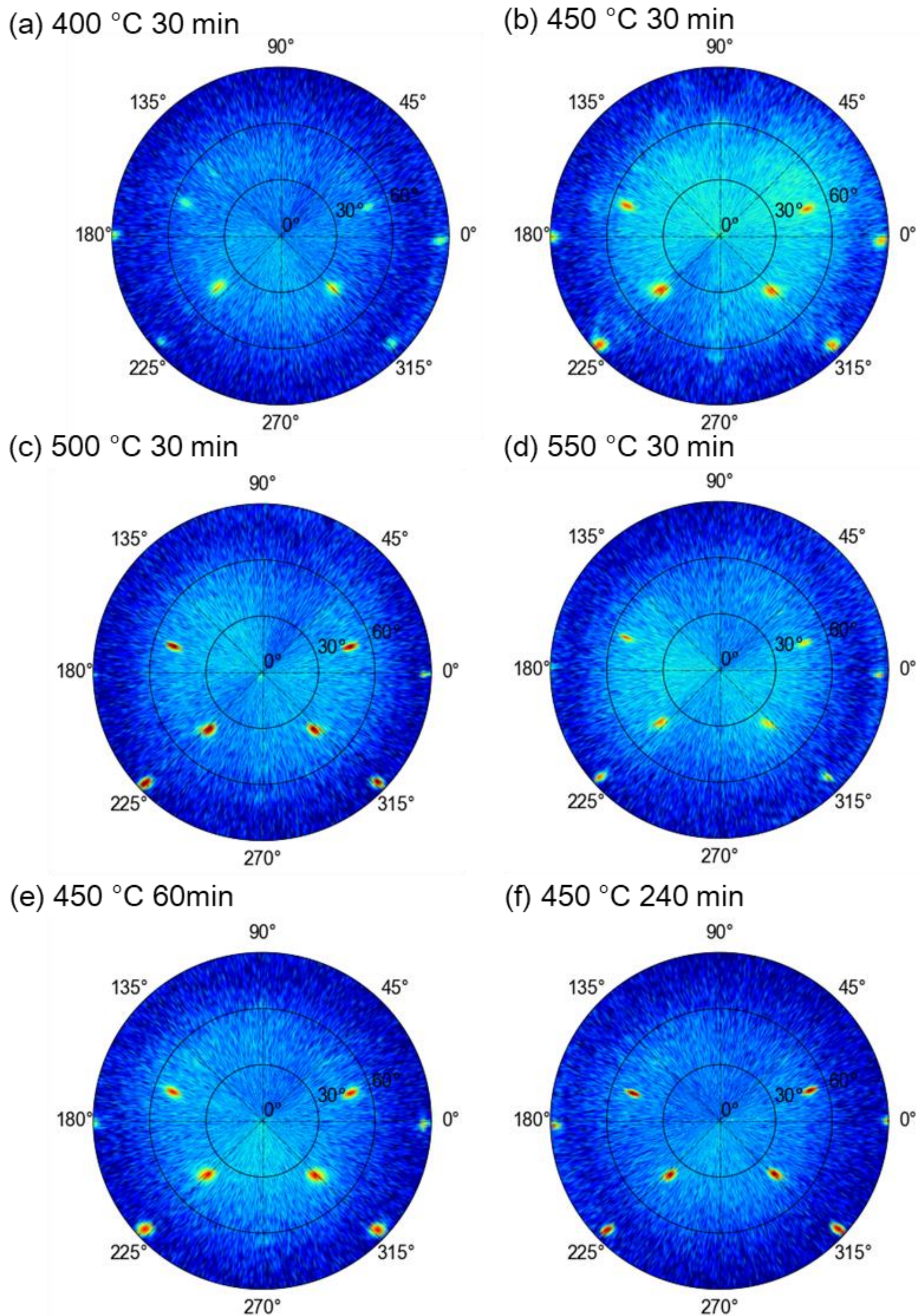

Figure 4-10 VO_2(101) pole figures of the samples after oxidation (a–d) at 400–550 °C for 30 min and (e, f) at 450 °C for 60 and 240 min.

The surface morphologies of the films before and after the oxidation were investigated using SEM. The as-deposited V_2O_3 film showed a relatively rough surface composed of grains with a size of approximately 100 nm (Figure 4-11a). When the film was oxidized at $\leq$ 500 °C, VO_2 was formed, as confirmed by the XRD results, and the grains became finer, forming a smoother surface (Figure 4-11b–d). However, the film oxidized at the highest temperature of 550 °C, in which V_2O_5 was formed (as indicated by the XRD results), consisted of flake-shaped grains (Figure 4-11e). Flake-shaped grains were also observed in the film oxidized at 500 °C (Figure 4-11d). Although the XRD pattern of the film oxidized at 500 °C showed only VO_2 diffraction peaks, its morphology indicated the presence of a small amount of V_2O_5. The films oxidized at 450 °C for 30–120 min also showed smooth surface because of the formation of VO_2 with an increase in the oxidation time. However, the film oxidized for a longer duration of 240 min showed flake-shaped grains on the surface, suggesting contamination with V_2O_5. Therefore, the oxidation temperature and duration of 450 °C and 120 min, respectively, were the best conditions for obtaining films with a smooth surface composed of single-phase VO_2. The cross-sectional SEM images (Figure 4-11i and j) showed that the surface of the V_2O_3 film smoothened after the oxidation and its thickness increased from approximately 100 to 120 nm. The volume expansion ratio of the film measured from the SEM images was consistent with the value calculated for the oxidation of V_2O_3 to VO_2 (~1.3) based on their densities (4.87 g cm^{-3} for V_2O_3 and 4.34 g cm^{-3} for VO_2).

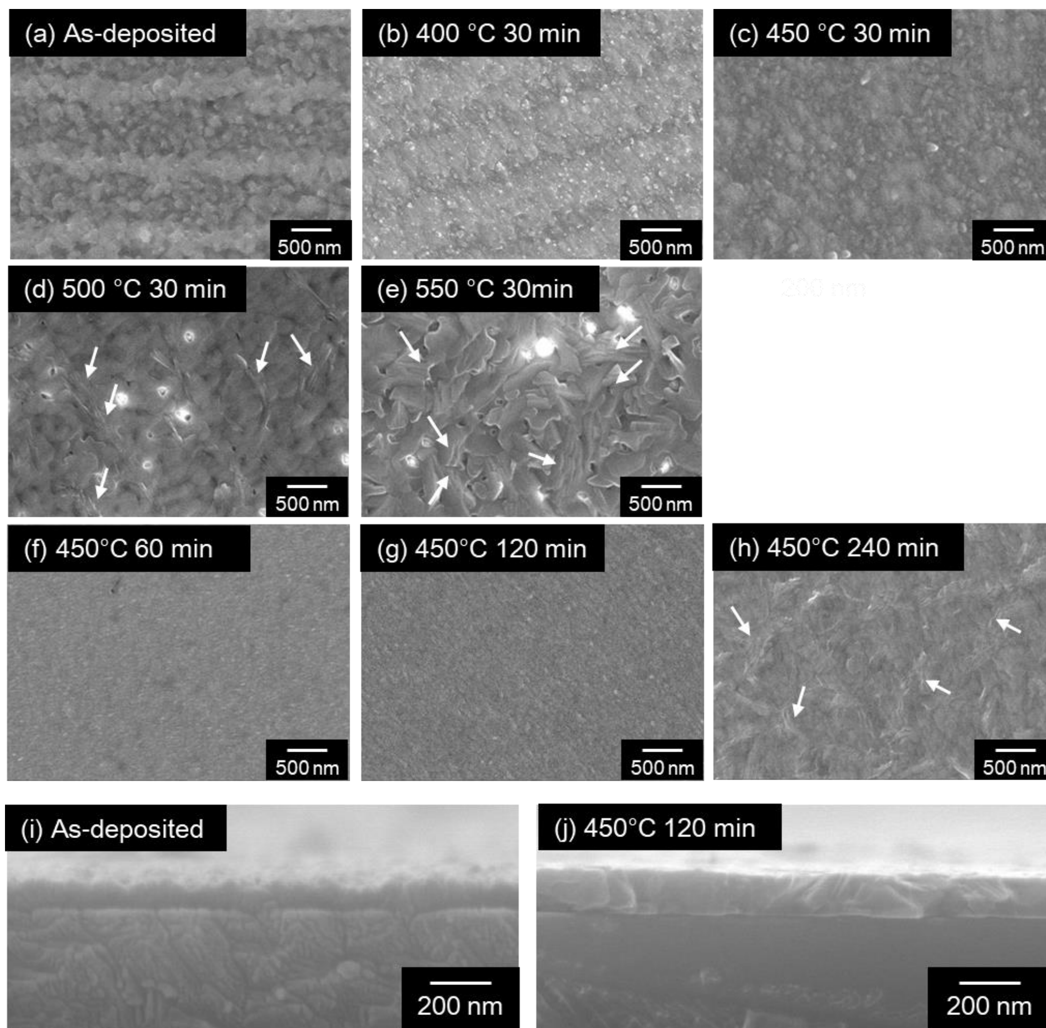

Figure 4-11 (a–h) Surface morphologies of the (a) as-deposited V_2O_3 film; (b–e) films oxidized for 30 min at (b) 400 °C, (c) 450 °C, (d) 500 °C, and (e) 550 °C; and (f–h) films oxidized at 450 °C for (f) 60 min, (g) 120 min, and (h) 240 min. The arrows in the images indicate flake-shaped grains. (i,j) Cross-sectional SEM images of the films (i) before and (j) after the oxidation at 450 °C for 120 min.

4.3.3 Topotactic relationship

The formation of VO_2 films with specific orientations from the epitaxial V_2O_3 film indicates that the oxidation was topotactic. Both the V_2O_3 and VO_2 crystals (before and after the oxidation, respectively) had two orientations. Each V_2O_3 crystal could be randomly transformed into a VO_2 crystal in either direction. This was confirmed by the fact that the intensities of the diffraction peaks of the two oriented VO_2 crystals were always the same irrespective of the abundance ratio of the two orientations of the V_2O_3 crystals before the oxidation (Figure 4-12). The abundance ratio of the V_2O_3 orientations depended on the deposition temperature, as indicated by the diffraction intensities in the pole figures (Figure 4-1b and Figure 4-4).

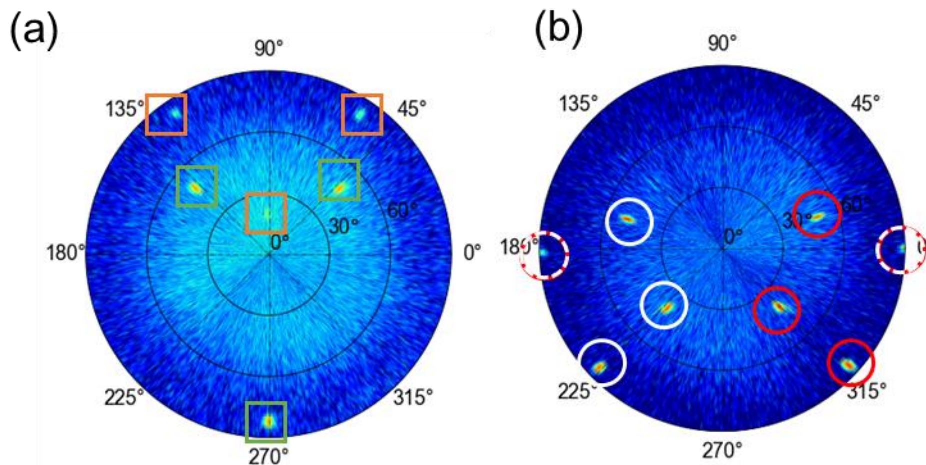

Figure 4-12 (a) V_2O_3 (104) pole figure of the V_2O_3 film deposited at 450 °C. The diffraction spots indicated by green and orange squares are attributed to the (012)- and (102) oriented-V_2O_3 crystals, respectively. The intense diffraction from the (012)- and (102) oriented-V_2O_3 crystals indicates that (012)-oriented crystals are present more than the (102)- oriented crystals. (b) VO_2 (101) pole figure of the sample formed after the oxidation of the V_2O_3 film. The diffraction spots indicated by red and white circles are attributed to the near $(2\bar{3}\bar{1})$-oriented VO_2 and $(23\bar{1})$-oriented VO_2 crystals. The similar diffraction intensities from the two differently oriented crystals indicate that the two orientations were equally present in the film.

To clarify the topotactic relationship, the orientation relationship between the as-deposited V_2O_3 and the VO_2 resulting from the thermal oxidation of V_2O_3 was analyzed based on their pole figures. The comparison of the pole figures in Figure 4-9 shows that because the position of the V_2O_3 (001) pole was consistent with that of the VO_2 (100) pole irrespective of the orientation of the crystals, the V_2O_3 and VO_2 crystals had a relative orientation such that V_2O_3 (001) // VO_2 (100) (see black arrows in Figure 4-9). With respect to the in-plane orientation of these planes, four relationships appeared to be established depending on the combination of the V_2O_3 and VO_2 crystals: e.g., V_2O_3 [120] // VO_2 $[0\bar{1}\bar{1}]$ between (012)-oriented V_2O_3 and near $(2\bar{3}\bar{1})$-oriented VO_2, and V_2O_3 [120] // VO_2 $[01\bar{1}]$ between (012)-oriented V_2O_3 and near $(23\bar{1})$-oriented VO_2 (see gray arrows in Figure 4-9). However, taking into account the three- and two-fold symmetry of the crystal structures of V_2O_3 and VO_2 along the axes normal to V_2O_3 (001) and VO_2 (100), respectively, these four relationships can be summarized as follows:

V_2O_3 (001) // VO_2 (100) and V_2O_3 [120] // VO_2 $[0\bar{1}\bar{1}]$

Owing to the similarity in their atomic arrangements, the crystal structures of V_2O_3 (corundum) and VO_2 (rutile) can be regarded as the derivatives of the NiAs-type structure. These crystal structures are shown in Figure 4-13a–c. In the NiAs-type structure, anions form a hexagonal close-packed structure, and their octahedral sites are occupied by cations. The structure of V_2O_3 (corundum) is similar to that of O and V atoms occupying all the anion sites and 2/3 of the cation sites of the NiAs structure, respectively. In VO_2 (rutile), O and V atoms occupy all the anion and 1/2 of the cation sites of the NiAs structure. Thus, both V_2O_3 and VO_2 can be regarded as having a framework almost same as that of the NiAs structure. From this perspective, the aforementioned orientation relationship between V_2O_3 and VO_2 indicates that the orientations of their corresponding NiAs-based frameworks were identical, i.e., V_2O_3 oxidized to VO_2 while retaining the NiAs-based framework.

In this oxidation process, the occupancy of the anion sites by O remained unchanged, while that of the cation sites by V decreased from 2/3 to 1/2. This indicates that the oxidation proceeded as V diffused out from the V_2O_3 phase, while the structural frame composed of O was retained. The V atoms that diffused out formed an additional VO_2 layer on the crystal surface by reacting with the oxygen from the gas phase.

Simultaneously, in the V_2O_3 region at the interface with VO_2, where the number of V atoms reduced, the rearrangement of the remaining V atoms among the cation sites might have occurred, completing the transformation to the VO_2 phase (Figure 4-13d).

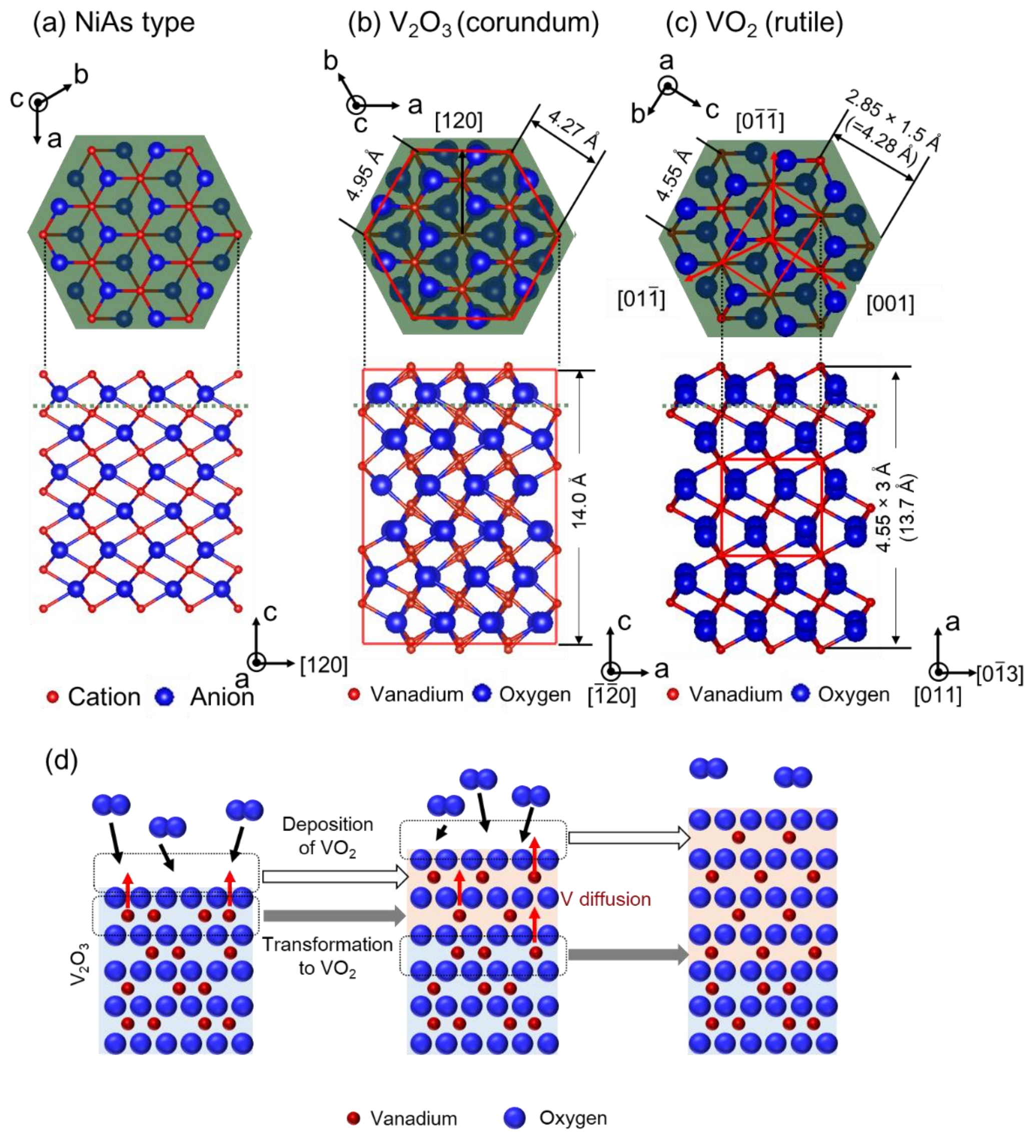

Figure 4-13 Atomic arrangements of (a) NiAs-type, and (b) V_2O_3 (corundum), and (c) VO_2 (rutile) structures. The green planes illustrated in the top views are translucent and were inserted at the positions indicated by the green dotted lines in the side views. The V_2O_3 and VO_2 unit cells are indicated by red lines. (d) Transformation process from V_2O_3 to VO_2 by oxidation.

As discussed earlier, the oxidation of V_2O_3 to VO_2 retains the NiAs-based framework. In this oxidation process, even though the NiAs-based framework is retained, VO_2 crystals with multiple orientations can be generated because the actual crystal structure of VO_2 is less symmetric than the NiAs structure. VO_2 and NiAs are two- and six-fold symmetric, respectively, along the c-axis of the corresponding NiAs structure. Therefore, a V_2O_3 crystal could be transformed into three VO_2 crystals with orientations that were three-fold symmetric with respect to each other. On the other hand, the (012)-oriented V_2O_3 and its 60° rotated crystal, i.e., the (102)-oriented V_2O_3, which was present in the as-deposited V_2O_3 films, shared the same NiAs-based framework. Accordingly, the oxidation of an epitaxial V_2O_3 film should result in a VO_2 film composed of crystals with three orientations at the maximum (Figure 4-14), regardless of the presence of rotated crystals in the initial epitaxial V_2O_3 film. Indeed, Yamaguchi et al. [13] reported that the oxidation of a (001)-oriented V_2O_3 film on a C-plane Al_2O_3 substrate results in a VO_2 film containing crystals with three orientations equivalent to the aforementioned orientation relationship (V_2O_3 (001) [120] // VO_2 (100) $[0\bar{1}\bar{1}]$).

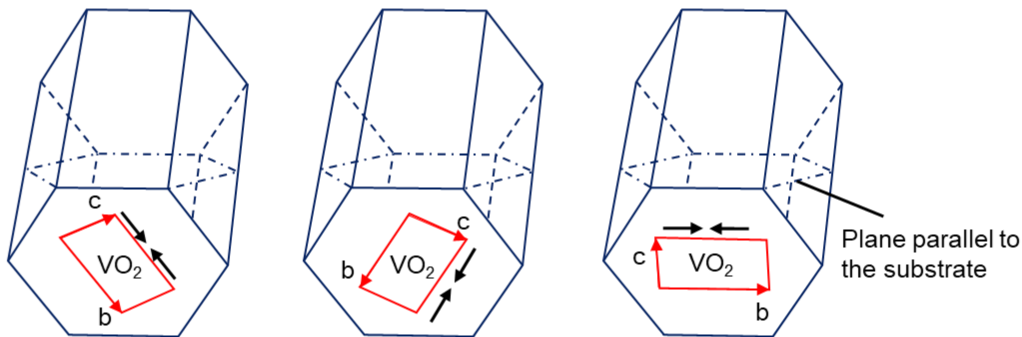

Figure 4-14 Schematic representation showing the orientations of the V_2O_3 crystal on the R-plane substrate and the three VO_2 crystals that could be generated by the oxidation of the V_2O_3 crystal retaining its NiAs-based framework. The V_2O_3-to-VO_2 transformation accompanied a large shrinkage of the crystal lattice along the b-axis of VO_2 (this direction is shown by the arrows in the figure). Among these three VO_2 crystals, the one with the b-axis parallel to the substrate surface (illustrated on the right) was not formed.

However, in this study, the V_2O_3 film on an R-plane Al_2O_3 substrate oxidized into VO_2 with only two orientations (near $(2\bar{3}\bar{1})$- and $(23\bar{1})$-oriented VO_2). Among the three expected orientations, the orientation in which the b-axis of the VO_2 crystal was parallel to the substrate surface was not realized. A possible reason for the absence of this orientation is that the transformation of V_2O_3 into VO_2 with this orientation accompanies large distortion of the crystal lattice in the direction parallel to the substrate. When V_2O_3 is oxidized into VO_2, the crystal lattice shrinks by 2.1%, 8.1%, and 0.3 % along the a-, b-, and c-axis of the VO_2 crystal, respectively (Figures 4-13b and c). Namely, the lattice shrinks the most along the b-axis of VO_2. During the oxidation of a film on a substrate, the crystal lattice of the film should shrink more easily in the direction normal to the substrate than in the direction parallel to the substrate because the film is constrained by the substrate. Therefore, the oxidation in which the b-axis of VO_2 becomes parallel to the substrate surface does not occur in the case of V_2O_3 films deposited on an R-plane Al_2O_3 substrate. On a C-plane Al_2O_3 substrate, the orientation relationship between each of the three VO_2 crystals and the substrate is identical. Hence, crystals with three different orientations are formed.

4.3.4 Resistance change across MIT

The temperature-dependent resistance of the VO_2 film fabricated by topotactic oxidation was examined to investigate its phase transition behavior. As shown in Figure 4-15, the resistance of the film oxidized at 450 °C for 120 min decreased dramatically at approximately 70 °C during heating and returned to its original value at approximately 60 °C during cooling. This temperature dependence of resistance is the typical MIT behavior of VO_2. By averaging the transition temperatures observed as the peak in the d(log R)/dT curve during heating and cooling (Figure 4-16), the phase transition temperature (T_c) of the film was determined to be 66 °C. This T_c value is typical of VO_2 [17–19]. The resistance of the film changed by four orders of magnitude with a change in temperature from 50 and 80 °C. The film oxidized at 450 °C for 120 min showed the largest change in resistance among all the films oxidized in this study (Figure 4-17). The change in the resistance of a VO_2 film across MIT becomes less significant when it is

contaminated by V^{3+}or V^{5+} [20]. The film oxidized at 450 °C for 120 min showed only VO_2 diffraction peaks (XRD pattern) and no flake-shaped grains, which suggested the presence of V_2O_5 (SEM images). Therefore, the large resistance change of the film can be attributed to the suppression of V^{3+} and V^{5+} contamination. The resistance change of the VO_2 film prepared by topotactic oxidation in this study is comparable to the maximum value for VO_2 thin films prepared by other processes, including direct epitaxial deposition [18]. No clear features attributed to the unique orientation of the film were observed in the MIT properties.

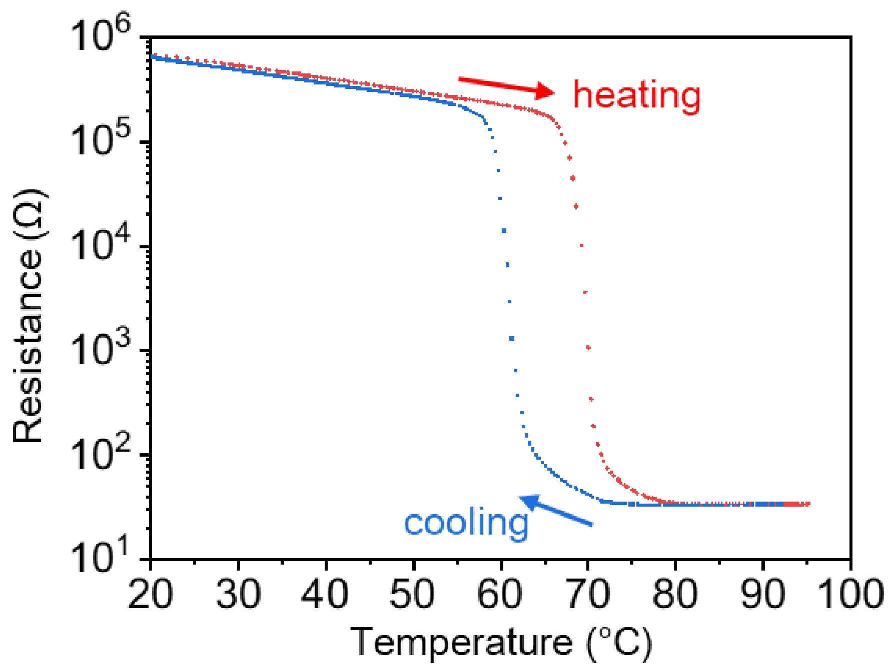

Figure 4-15 Temperature dependent resistance of the VO_2 film formed by the oxidation of V_2O_3 at 450 °C for 120 min.

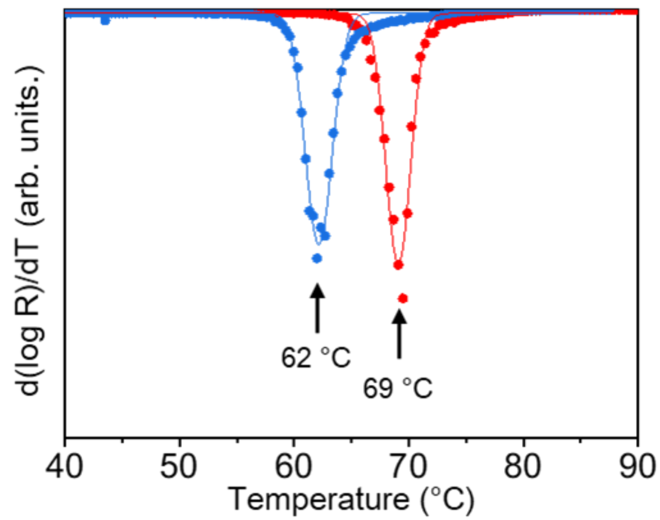

Figure 4-16 d(Log R)/dT derivative curves of the VO_2 film oxidized at 450 °C for 120 min for the heating and cooling processes.

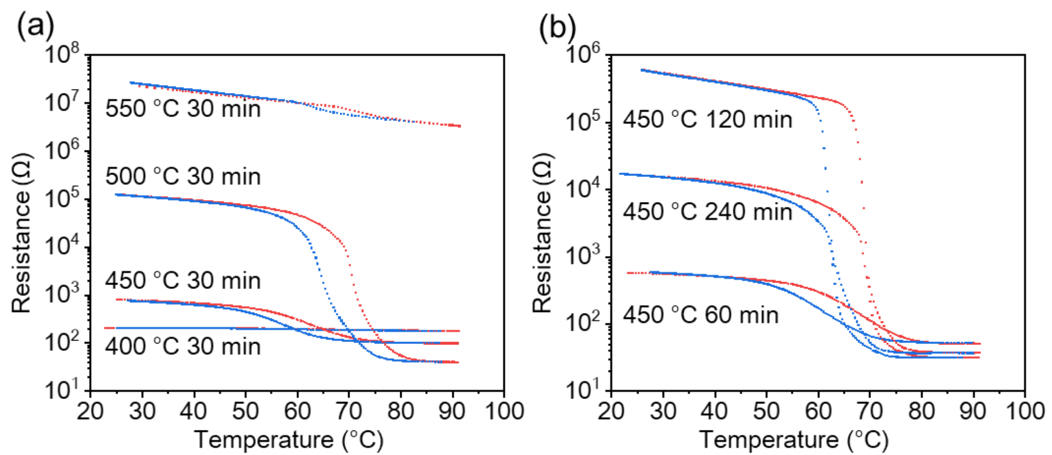

Figure 4-17 Temperature dependent resistance curves of the films obtained after the oxidation (a) at 400–550 °C for 30 min and (b) at 450 °C for 60–240 min.

4.4 Conclusion

Oriented VO_2 films were fabricated by the thermal oxidation of V_2O_3 films grown epitaxially on an R-plane Al_2O_3 substrate. The epitaxial V_2O_3 film prepared by mist CVD consisted of crystals with two orientations, which were rotated by 60° around the c-axis with respect to each other. The oxidation of the V_2O_3 film under the flow of N_2–1% O_2 gas at 450 °C for 120 min resulted in the formation of a film composed of single-phase VO_2 with a smooth surface. The VO_2 film had a unique orientation where the $(2\bar{3}\bar{1})$ or $(23\bar{1})$ planes were almost parallel to the substrate surface but tilted a few degrees. The orientation relationship between the V_2O_3 and VO_2 films and the atomic arrangements of their crystals indicated that the crystal structures of both V_2O_3 and VO_2 had almost the same NiAs-type structural framework and the oxidation proceeded topotactically while retaining the NiAs-based framework. Although the crystallographic symmetry shows that this transformation retaining the NiAs-type structure can form VO_2 crystals with three different orientations, the oxidation of the V_2O_3 epitaxial film on the R-plane Al_2O_3 substrate resulted in the formation of a VO_2 film composed of crystals with only two orientations. The limitation in the orientation can be attributed to the large shrinkage of the crystal lattice of the film, which is unlikely to occur in the direction parallel to the substrate. The resistance change across the MIT of the obtained film was over four orders of magnitude, which is comparable to that of directly deposited epitaxial VO_2 films. The topotactic oxidation approach, which was used in this study to produce oriented VO_2 films exhibiting large resistance change, can be used for the development of novel devices exploiting the potential anisotropic properties of VO_2.

References

[1] J. Lappalainen, S. Heinilehto, S. Saukko, V. Lantto, H. Jantunen, Microstructure dependent switching properties of VO_2 thin films, Sensors Actuators A Phys. 142 (2008) 250–255. https://doi.org/10.1016/j.sna.2007.05.002.

[2] L.L. Fan, S. Chen, Y.F. Wu, F.H. Chen, W.S. Chu, X. Chen, C.W. Zou, Z.Y. Wu, Growth and phase transition characteristics of pure M-phase VO_2 epitaxial film prepared by oxide molecular beam epitaxy, Appl. Phys. Lett. 103 (2013) 131914. https://doi.org/10.1063/1.4823511.

[3] P. Jin, K. Yoshimura, S. Tanemura, Dependence of microstructure and thermochromism on substrate temperature for sputter-deposited VO_2 epitaxial films, J. Vac. Sci. Technol. A Vacuum, Surfaces, Film. 15 (1997) 1113–1117. https://doi.org/10.1116/1.580439.

[4] V. Théry, A. Boulle, A. Crunteanu, J.C. Orlianges, A. Beaumont, R. Mayet, A. Mennai, F. Cosset, A. Bessaudou, M. Fabert, Structural and electrical properties of large area epitaxial VO_2 films grown by electron beam evaporation, J. Appl. Phys. 121 (2017) 055303. https://doi.org/10.1063/1.4975117.

[5] C. Zhang, C. Kang, H. Zong, S. Liang, C. Geng, M. Li, Roles of TiO_2 buffer layer for preparation of high performance VO_2 thin films with Monoclinic polymorph, Results Phys. 10 (2018) 628–632. https://doi.org/10.1016/j.rinp.2018.07.003.

[6] X. Zhou, D. Gu, S. Xu, H. Qin, Y. Jiang, Investigation on microstructures and phase transition characteristics of titanium/yttrium co-doped vanadium oxide thin films, Mater. Res. Bull. 105 (2018) 98–103. https://doi.org/10.1016/j.materresbull.2018.04.044.

[7] K.R. Speck, H.S.-W. Hu, M.E. Sherwin, R.S. Potember, Vanadium dioxide films grown from vanadium tetra-isopropoxide by the sol-gel process, Thin Solid Films. 165 (1988) 317–322. https://doi.org/10.1016/0040-6090(88)90702-X.

[8] B.I. Stefanov, G.A. Niklasson, C.G. Granqvist, L. Österlund, Gas-phase photocatalytic activity of sputter-deposited anatase TiO_2 films: Effect of <001> preferential orientation, surface temperature and humidity, J. Catal. 335 (2016) 187–196. https://doi.org/10.1016/J.JCAT.2015.12.002.

[9] D. Imazeki, C.C. van Gils, K. Nishio, R. Shimizu, T. Hitosugi, Effects of Anisotropy in Rutile TiO_2 on the Performance of Solid-State Lithium Batteries, ACS Appl. Energy Mater. (2020) acsaem.0c00910. https://doi.org/10.1021/acsaem.0c00910.

[10] N. Ueda, H. Hosono, R. Waseda, H. Kawazoe, Anisotropy of electrical and optical properties in β-Ga_2O_3 single crystals, Appl. Phys. Lett. 71 (1998) 933. https://doi.org/10.1063/1.119693.

[11] H. Yoon, J. Park, S.-Y. Choi, D. Lee, J. Son, Facet-Dependent Phase Control by Band Filling

and Anisotropic Electron-Lattice Coupling in HVO_2 Epitaxial Films, Adv. Electron. Mater. 4 (2018) 1800128. https://doi.org/10.1002/aelm.201800128.

[12] J. Park, C. Oh, J. Son, Anisotropic ionic transport-controlled synaptic weight update by protonation in a VO_2 transistor, J. Mater. Chem. C. 9 (2021) 2521–2529. https://doi.org/10.1039/D0TC05628F.

[13] I. Yamaguchi, T. Manabe, T. Tsuchiya, T. Nakajima, M. Sohma, T. Kumagai, Preparation and characterization of epitaxial VO_2 films on sapphire using postepitaxial topotaxy route via epitaxial V_2O_3 films, Jpn. J. Appl. Phys. 47 (2008) 1022–1027. https://doi.org/10.1143/JJAP.47.1022.

[14] K. Okimura, Y. Suzuki, Epitaxial growth of V_2O_3 thin films on c-plane Al_2O_3 in reactive sputtering and its transformation to VO_2 films by post annealing, Jpn. J. Appl. Phys. 50 (2011) 65803. https://doi.org/10.1143/JJAP.50.065803.

[15] K. Momma, F. Izumi, VESTA 3 for three-dimensional visualization of crystal, volumetric and morphology data, J. Appl. Crystallogr. 44 (2011) 1272–1276. https://doi.org/10.1107/S0021889811038970.

[16] J. Park, H. Yoon, H. Sim, S.Y. Choi, J. Son, Accelerated Hydrogen Diffusion and Surface Exchange by Domain Boundaries in Epitaxial VO_2 Thin Films, ACS Nano. 14 (2020) 2533–2541. https://doi.org/10.1021/acsnano.0c00441.

[17] Y. Zhao, J. Hwan Lee, Y. Zhu, M. Nazari, C. Chen, H. Wang, A. Bernussi, M. Holtz, Z. Fan, Structural, electrical, and terahertz transmission properties of VO_2 thin films grown on c-, r-, and m-plane sapphire substrates, J. Appl. Phys. 111 (2012) 053533. https://doi.org/10.1063/1.3692391.

[18] H.-T. Zhang, L. Zhang, D. Mukherjee, Y.-X. Zheng, R.C. Haislmaier, N. Alem, R. Engel-Herbert, Wafer-scale growth of VO_2 thin films using a combinatorial approach, Nat. Commun. 6 (2015) 8475. https://doi.org/10.1038/ncomms9475.

[19] D.H. Jung, H.S. So, K.H. Ko, J.W. Park, H. Lee, T.T.T. Nguyen, S. Yoon, Electrical and optical properties of VO_2 thin films grown on various sapphire substrates by using RF sputtering deposition, J. Korean Phys. Soc. 69 (2016) 1787–1797. https://doi.org/10.3938/jkps.69.1787.

[20] H. Kim, N. Charipar, M. Osofsky, S.B. Qadri, A. Piqué, Optimization of the semiconductor-metal transition in VO_2 epitaxial thin films as a function of oxygen growth pressure, Appl. Phys. Lett. 104 (2014) 081913. https://doi.org/10.1063/1.4866806.

Chapter 5 General Conclusion

In this study, the author reported the fabrication of MoO_2 and VO_2 films using the mist CVD method, which can fabricate films with lower energy consumption and lower manufacturing costs. The effects of substrate position, deposition temperature, and solvent on the properties of the resulting films were investigated to obtain MoO_2 and VO_2 films with excellent properties. In addition, the thermal oxidation of mist-CVD-grown V_2O_3 epitaxial films was explored to fabricate highly oriented VO_2 films, and the properties of the resulting films were investigated. The results obtained through this study are summarized as follows.

Chapter 2

MoO_2 thin films were fabricated by mist CVD using acetylacetonate salt as the precursor. The MoO_2 films were deposited at furnace temperatures of ≥ 440 °C; however, an additional phase was obtained for the MoO_2 films deposited at a furnace temperature of 550 °C. Examination of the films deposited at various positions in the furnace at different furnace temperatures revealed that smooth MoO_2 films composed of densely packed crystal grains with a constant thickness of 200 nm could be obtained over an area >30 cm^2 at a furnace temperature of ~480 °C. The MoO_2 films showed a low electrical resistivity of 2×10^{-3} Ω cm.

Chapter 3

VO_2 films were fabricated by mist CVD and their thermochromic properties were investigated. The author investigated the effect of the solvent of the precursor solution on the resulting film. Films consisting of a single phase of VO_2 were formed when a water-based precursor solution was used. In contrast, V_2O_3 films were formed when a methanol-based precursor solution was used. The VO_2 film deposited using the water solution exhibited high visible transmittance with a large change in the infrared transmittance with temperature change compared with those of mist-CVD-grown VO_2 films reported earlier. These values were similar to those of high-quality VO_2 deposited by solution and vacuum processes.

Chapter 4

Highly oriented VO_2 films were fabricated by the thermal oxidation of a V_2O_3 film grown epitaxially on an R-plane Al_2O_3 substrate. The epitaxial V_2O_3 film prepared using mist CVD consisted of crystals with two orientations, which were rotated by 60° around the c-axis with respect to each other. The oxidation of the V_2O_3 film under a flow of N_2–1% O_2 gas at 450 °C for 120 min resulted in the formation of a film composed of single-phase VO_2 with a smooth surface. The VO_2 film had a unique orientation in which the $(2\bar{3}\bar{1})$ or $(23\bar{1})$ planes were almost parallel to the substrate surface but tilted by a few degrees. The orientation relationship between the V_2O_3 and VO_2 films and the atomic arrangements of their crystals indicated that the crystal structures of both V_2O_3 and VO_2 had almost the same NiAs-type structural framework and the oxidation proceeded topotactically while retaining the NiAs-based framework. Although the crystallographic symmetry shows that this transformation retaining the NiAs-type structure can form VO_2 crystals with three different orientations, the oxidation of the V_2O_3 epitaxial film on the R-plane Al_2O_3 substrate resulted in the formation of a VO_2 film composed of crystals with only two orientations. The limitation in the orientation can be attributed to the large shrinkage of the crystal lattice of the film, which is unlikely to occur in the direction parallel to the substrate. The resistance change across the MIT of the obtained film was over four orders of magnitude, which is comparable to that of directly deposited epitaxial VO_2 films.

Future perspective

Chapter 2

Dense and uniform MoO_2 films were fabricated over a large area (>30 cm^2) using mist CVD. The electrical conductivity of these films was higher than that of MoO_2 films fabricated using a solution process. MoO_2 films fabricated using the solution process were studied for application in batteries having higher energy density and efficient hydrogen evolution catalysts. Therefore, MoO_2 films with higher conductivity fabricated using the mist CVD method, can be used to improve the performance of these devices.

Chapter 3

Single-phase of VO_2 films were fabricated using mist CVD. The VO_2 films exhibit excellent thermochromic properties, and thus, their use in smart windows is expected to increase. In this chapter, the effects of the precursor solution solvent on the oxidation states of vanadium oxide films deposited by mist CVD are clarified. This knowledge contributes to the use of mist CVD for other metal oxides, in which the metal has multiple oxidation numbers such as oxides of tungsten, chromium, and tin.

Chapter 4

VO_2 films with unique orientations were fabricated by the topotactic oxidation of the V_2O_3 epitaxial film. However, no clear features attributed to the unique orientation of the VO_2 film were revealed by the temperature-dependent resistance curve. Investigation of the MIT behavior via H^+ insertion could reveal the features attributed to the unique orientation of the VO_2 film and contribute to the development of novel devices using the anisotropic properties of VO_2.

The detailed mechanism that determines the orientation of VO_2 fabricated by the topotactic oxidation of the V_2O_3 epitaxial film was revealed. The proposed mechanism can contribute to the fabrication of metal oxide thin films with various orientations by topotactic reaction.

List of Publications

A. Full Length Papers

1.

Chapter2

Yuya Matamura, Takumi Ikenoue, Masao Miyake, Tetsuji Hirato

“Mist chemical vapor deposition of MoO_2 thin films”

Journal of Crystal Growth, 548, (2020) 125862

https://doi.org/10.1016/j.jcrysgro.2020.125862

2.

Chapter 3

Yuya Matamura, Takumi Ikenoue, Masao Miyake, Tetsuji Hirato

“Mist CVD of vanadium dioxide thin films with excellent thermochromic properties using a water-based precursor solution”

Solar Energy Materials and Solar Cells, 230, (2021), 111287

https://doi.org/10.1016/j.solmat.2021.111287.

3.

Chapter 4

Yuya Matamura, Makoto Kimura, Takumi Ikenoue, Masao Miyake, Tetsuji Hirato

“Formation of uniquely oriented VO_2 thin film by topotactic oxidation of V_2O_3 epitaxial film on R-plane Al_2O_3”

Crystal Growth and Design (submitted)

B. Oral Presentation

1. **Yuya matamura**, Masao Miyake, Takumi Ikenoue, and Tetsuji Hirato

“Growth of MoO_2 thin films by mist CVD”

20th forum of Kansai surface finishing, Konan University, November, 2018

2. **Yuya Matamura**, Takumi Ikenoue, Masao Miyake, and Tetsuji Hirato
"Fabrication of MoO_2 thin films and evaluation of their electrical properties."
80th autumn meeting of the Japan society of Applied Physics, Hokkaido University, September, 2019

C. Poster Presentation

1. **Yuya Matamura**, Takumi Ikenoue, Masao Miyake, and Tetsuji Hirato
"Effect of temperature on the preparation of MoO_2 thin films by a mist CVD method"
38th Electronic Materials Symposium, Nara, Japan, October, 2019

2. **Yuya Matamura**, Takumi Ikenoue, Masao Miyake, and Tetsuji Hirato
"Epitaxial growth of molybdenum dioxide by mist CVD"
130th meeting of surface finishing society of Japan, Kanagawa University, March, 2019

3. **Yuya Matamura**, Takumi Ikenoue, Masao Miyake, and Tetsuji Hirato
"Fabrication of vanadium dioxide film for smart window application via mist CVD and its optical properties."
68th spring meeting of the Japan society of Applied Physics, Online, March, 2021

D. Awards

1. Research incentive award
20th forum of Kansai surface finishing, Konan University, November, 2018

2. Poster award
68th spring meeting of the Japan society of Applied Physics, Online, March, 2021

Acknowledgements

The author would like to express his sincere gratitude to Professor Tetsuji Hirato for his attentive supervision, insightful advice, and warm encouragement. The author would like to express his appreciation to Professor Toshiya Doi for reviewing this thesis and support with experimental equipment including SEM and AFM. The author is grateful to Professor Hitoshi Fujimoto for reviewing this thesis.

The author is deeply grateful to Associate Professor Masao Miyake for his detailed instructions and careful advice throughout this study. The author would like to thank Assistant Professor Takumi Ikenoue for his insightful suggestions and help with various aspects of this study.

The author thanks Associate Professor Masakatsu Hasegawa for his valuable advice and suggestions. The author would like to express his special gratitude to Assistant Professor Shota Higashino for his constructive discussion and warm encouragement. The author is grateful to Mr. Suguru Shiomi for his valuable suggestions and the instruction on the use of various experimental equipment. The author is obliged to Mr. Yuki Haruta for his continuous discussions and encouragement. The author greatly thanks Mr. Makoto Kimura for his help with the analysis. The author would like to offer special thanks to Ms. Sachiko Yamamoto and Toshiko Morita for their help to create a comfortable environment for this study. The author thanks the entire Materials Processing group in the Energy Science Department for fruitful discussions and help throughout this study.

The author would like to express appreciation to the Japan Science and Technology Agency for their financial aid.

The author would like to express sincere thanks to all his family and friends for their continuous encouragement and support. The author is especially grateful to Dai Matamura, Chikako Matamura, Michiya Matamura, Masaya Matamura, and Rie Hayashi.